Atomistic Simulations of Octacyclopentyl Polyhedral Oligomeric Silsesquioxane Polyethylene Nanocomposites

by

Franco M. Capaldi

M.S. Mechanical Engineering
Massachusetts Institute of Technology, 2001

B.S. Mechanical Engineering
Brown University, 1999

SUBMITTED TO THE DEPARTMENT OF MECHANICAL ENGINEERING IN PARTIAL FULFILLMENT OF THE REQUIREMENTS FOR THE DEGREE OF

DOCTORATE OF PHILOSOPHY IN MECHANICAL ENGINEERING
AT THE
MASSACHUSETTS INSTITUTE OF TECHNOLOGY

JUNE 2005

Signature of Author: _____
Department of Mechanical Engineering
005

Certified by: _____
Mary C. Boyce
Professor of Mechanical Engineering

_____
Gregory C. Rutledge
Chemical Engineering

Accepted by: _____
Lallit Anand
Chairman, Department Committee on Graduate Students

Atomistic Simulations of Octacyclopentyl Polyhedral Oligomeric Silsesquioxane Polyethylene Nanocomposites

Franco M. Capaldi

Submitted to the Department of Mechanical Engineering
On March 14, 2005 in Partial Fulfillment of the
Requirements for the Degree of Doctorate of Philosophy in
Mechanical Engineering

As the scientific community develops the ability to create composites which incorporate nanoscopic filler particles, the detailed atomic arrangement and atomic interactions become significant in determining the composite properties. Nanoscopic fillers such as carbon nanotubes, polyhedral oligomeric silsesquioxane (POSS), and layered silicates have already been successfully used to improve the thermal and mechanical properties of polymers. On this length scale, details describing particle organization, interaction between particles, and interactions between particle and matrix are needed to understand the behavior of the composite.

In this thesis, we use atomistic simulations to investigate the detailed behavior of a blended octacyclopentyl polyhedral oligomeric silsesquioxane (CpPOSS) / polyethylene (PE) nanocomposite. The model potential employed to describe the atomic interactions in these systems is capable of reproducing the experimental vibrational and crystal structures for the POSS well. The mechanical properties of an infinite crystal were calculated. They are anisotropic with a Reuss average isotropic elastic modulus of 11.78 GPa.

Simulations of CpPOSS/PE composites revealed that the POSS had a stiffening effect on the polymer. Simulations revealed that both PE and POSS dynamics as measured by translational and rotational diffusivities decreased, the glass transition temperature increased, and both the density and modulus increased with increasing POSS content. Micromechanical models were fit to the composite modulus which allowed effective mechanical particle sizes to be determined.

The POSS was found to aggregate into small necklace structures which have internal ordering similar to the crystal phase. The formation of crystallites was found to be energetically favorable in this system. A coarse grained potential which accounts for both the attraction and orientation between particles was developed to aid the further study of aggregation and crystallization in these composites.

The interface between the POSS and the polymer is found to consist of polymer chains aligned tangentially to the POSS cage. This layer has increased mobility tangential to the surface of the particle and decreased mobility in the radial direction. Though it is very thin, consisting of only 1 or 2 monolayers of polymer, due to the small size of the POSS particle, the weight fraction of polymer in the interfacial region is as high as 43 % in the 25 weight percent CpPOSS/PE composite. These simulations reveal the formation of structure on both the angstrom length scale in the polymer near the interface and the mesoscopic length scale between the POSS particles.

Thesis Supervisors:
Mary C. Boyce
Professor of Mechanical Engineering

Gregory C. Rutledge
Professor of Chemical Engineering

Acknowledgements

I have been extremely fortunate to work with many amazingly talented and helpful people. All have impacted my work and life in some way or another and for this I am thankful. I would like to thank my thesis advisors, Professor Mary Boyce and Professor Gregory Rutledge for their guidance, advice and for providing a first-rate research and learning environment. Thanks to my thesis committee members, Professor Robert Cohen and Professor Nicolas Hadjiconstantinou, for thoughtful discussions. I am grateful to the National Science Foundation and the Air Force Office of Scientific Research for the financial support of my graduate work.

In the Mechanics and Materials group, I have known and worked with many great people who have made my time at MIT enjoyable. Though I cannot possibly list them all, special thanks to Mohit, Mats, Mike, Ethan, Rebecca, Dora, Sauri, Brian, Prakash, Tom, Hang, Jin, Matt, Rami, Steve, Antonio, Numan, Ahmed, Markus, Pieter, Fred, Sergei, Vikram, Amrit, Michelle, Ed, and Adam. Also, I would like to thank the staff of the Mechanical Engineering Department, and the mechanics group Una, Ray, Leslie and Joan for making my life much easier.

Most of all, I express my gratitude to my entire family. Thanks to my mother, father and sister, Laura, for their constant encouragement and support, and the faith they have shown in me and especially to my wife, Irene, for providing inspiration, motivation, love, and just about everything else I have needed throughout my time here.

Table of Contents

List of Figures

List of Tables

Chapter 1
Introduction

1.1 Polymer Nanocomposites

Interest in polymer nanocomposites has been driven by the desire to create materials with novel sets of properties. The ability to control the nanostructure of the material to achieve a tougher and stiffer composite, or a stiffer composite without sacrificing the processibility of the polymer, or achieving a functional composite would greatly impact polymer science. The behavior of these nanocomposites can be the result of phenomena on several different length scales. The polymer/filler interface, the dispersion state of the filler, the length scale of the filler in comparison to the length scale of the polymer can all influence the material properties. Understanding the interplay between these variables continues to be a difficult but worthwhile task.

It is important to understand that the specific atomic interactions between polymer and filler are critical in determining the behavior of the composite. This can be seen clearly in work by Starr et al. [1, 2]. In their simulations of a bead-spring polymer surrounding a single nanoparticle, they have found that for an attractive polymer/particle interaction there was an increase in the glass transition temperature of the polymer, while for a repulsive polymer/particle interaction there was a decrease in the glass transition temperature. The simulations considered very low loadings (below 5 volume percent) of filler. An attractive interaction at the wall traps polymer near the surface and decreases its mobility while the repulsive interaction actually increases the mobility of polymer chains near the surface of the particle. This shows that the nature of the interactions across the interface can change the effective behavior of the nanocomposite.

There is also experimental data that shows that the nanoparticle may influence the dynamics of the polymer surrounding it. Mansencal et al. [3] have used solid-state NMR to investigate the interface between polybutadiene, PB, and carbon black. In their studies, the polybutadiene surrounding the carbon black had strongly reduced mobility and cannot be detected as undergoing the glass transition. They also find that the 1,2-PB moiety is more closely bound by the filler than is the 1,4-PB fraction. Interestingly, the differences

between 1,2-PB and 1,4-PB show quite clearly that chemically specific interactions within the interface are important in determining its properties.

The interfacial surface area in the system depends strongly on the dispersion state of the system. Experimental work studying the interface between polymer and filler[3-5] reveals this. Berriot et al. [4, 5] used NMR to study the interface between grafted nanosilica particles and crosslinked ethylacrylate chains. Changes in the NMR signal during the addition of strongly interacting particles were tied to changes in the material dynamics in polymer matrix material surrounding them. However, the influence depended not only on the surface characteristics but also on the dispersion characteristics of the system. Agglomerated systems and dispersed systems were created with the same volume fraction of filler and those which were aggregated had less interface and the effect on the surrounding polymer was less significant.

There can also be significant structural changes in the polymer near the interface. Factor et al. [6] used grazing incidence X-ray scattering to study an aromatic polyimide, poly(pyromellitic dianhydride-oxydianiline) film deposited on a polished silicon surface. The air/polymer surface showed significant ordering and when thermally treated at temperatures above 300° C, crystalline-like ordering was observed. However, the polymer/silicon surface showed no signs of ordering.

The changes in molecular structure and ordering that occur near surfaces and interfaces can have significant effects on the bulk properties of the composite. Shearing molecularly thin films of cyclohexane, octamethylcyclotetrasiloxane, n-octance, n-tetradecane and branched isoparaffin 2-methyloctadecane liquids between two mica surfaces, Gee et al. [7] have shown the development of molecular ordering within these thin films. As the film thickness was decreased, the liquids became more solid like with viscosities which were as much as 105 times that of the bulk value and relaxation times were more than ten orders of magnitude slower. The decreasing thickness made surface structure much more important in determining the behavior of the material.

There have been several attempts to model generic polymer/filler interfaces in coarse grained models[1, 2, 8-10], as well as atomistically detailed simulations of POSS nanocomposites [11]. Vacatello has performed Monte Carlo simulations on simple bead spring models of polymers interacting with large spherical particles [8]. Polymer chains

near the surface of the spherical inclusion were found to adopt a modified configuration and preferentially lie parallel to the surface of the particle. The polymer was found to form densely packed and ordered shells around the particle analogous to those found near planar solid surfaces [8].

Length scales can also play an important role in determining the behavior of the nanocomposite. In the polymer filled nanocomposite, the relevant length scales are the radius of gyration of the polymer chain, size of the monomer unit, and the length scale of the particle filler. Small angle neutron scattering by Nakatani et al. [12, 13] on systems of poly(dimethyl siloxane), PDMS, containing trimethylsilyl-treated polysilicate particles have found that the particle presence influences the radius of gyration of the polymer. There is a decrease in Rg when the polymer chains are smaller than the filler particles and an increase in Rg when the polymer chains are much larger than the particles. These results are supported by Monte Carlo simulations based on rotational isomeric state (RIS) theory of PDMS and a rigid non-interacting filler particle by Yuan et al.[14].

Larger particles or even sheets can be formed through aggregation of nanoparticles. Because of this, understanding the interactions between polymers and solid surfaces can be quite relevant. A number of experiments [6, 7, 15] and simulations [14, 16-20] suggest that there are conformational changes and changes in the packing of the polymer in the interfacial region as compared to the bulk. The polymer within the interface tends to be aligned parallel to the solid surface and forms densely packed and ordered layers. This is similar to the effects seen near the surface of the nanoparticle discussed earlier.

Simulations by Jang et al. [17] using lattice Monte Carlo simulations of polyethylene near surfaces reveals changes in the structure and mobility of polymer near the surface of the solid wall, again similar to the effects seen near the surface of nanoparticles. When the nanoparticle diameter is on the size of the polymer radius of gyration, the added curvature of the nanoparticle's surface does not seem to change the fundamental phenomena observed between flat walls and polymer. The reason for this is probably due to the fact that the changes in dynamics and mobility occur on the monomer length scale. As long as the curvature of the particle does not exceed this, i.e. the particle

size is larger than the monomer size, then the effects near the particle and near the wall should be similar.

Measurements of the solvation forces between mica surfaces and alkane chains by Christenson et al. [15] have shown a preferential alignment of alkane chains parallel to the surface of the mica surface. A thin layer of alkane chains was placed between two mica surfaces and the force versus distance curve was obtained. Variation in the force versus distance curve was found to vary up to a distance of 3 Å from the mica surface indicating that the interface did not extend past this distance. Vacatello [21] has performed Monte Carlo simulations on a nanoslit filled with a bead spring model which mimics the configuration of the mica experiments. In these simulations, there is an oscillation in the curve of force versus the distance between the two surfaces. This variation in force is tied to ordering of the polymer into layers within the nanoslit. This seems to agree well with the experiments of Christenson et al. [15] described above.

We see that nanoparticles embedded in polymer can have significant effects on the structure and properties of the polymer. The changes in polymer orientation, radius of gyration, mobility, and density near the surface of the particle will be investigated in this thesis for the particular case of octa cyclopentyl polyhedral oligomeric silsesquioxane polyethylene system.

1.2 Polyhedral Oligomeric Silsesquioxane

The polyhedral oligomeric silsesquioxane (POSS) macromonomer[22, 23] consists of an inorganic of silicon and oxygen core surrounded by organic groups on the corners. The structure of a POSS macromonomer with cage structure of Si_8O_{12} is shown in Figure 1-1. The crystal structures of octa-methylsilsesquioxane [24], octasilsesquioxane [25], octacyclopentyl POSS [26], and several other POSS cages have been determined [27, 28].

When creating polymer/POSS nanocomposites, the outer organic groups can be chosen to promote compatibility between POSS and polymer. POSS may be incorporated into a polymer either by chemically tethering it to the polymer backbone or by blending the particles with the polymer matrix. POSS has been successfully copolymerized with polysiloxane[29-31], poly(methyl methacrylate)[32], polynorbornene[33],

polystyrene[34], polyethylene[35], and polyurethane [36-38]. POSS has also been blended with amphiphilic poly(dimethylsiloxane) [39], epoxy [40], and poly(methyl methacrylate) [41].

There are many possible applications for POSS. Tegou et al. [42] demonstrated the ability to create POSS resists suitable for 157 nm lithography and had the potential for sub 100 nm resolution patterns. POSS based resists offer the advantage higher glass transition temperatures (increases of 10-40 degrees), inherent etch resistance to oxygen plasma, and a well defined structure. Bleha et al. [43] are investigating the incorportation of POSS into chitosan films as a means to control the mechanical properties and permeability of the chitosan film. While success was limited in this goal, the study show quite clearly that composite properties depend strongly on processing. With one set of processing steps, the permeability increased, reversing the drying and crosslinking steps led to a decrease in the permeability. Maitra et al. [44] are studying polyethylene oxide functionalized polyhedral oligosilsesquioxanes and lithium salts. These materials may provide solid polymer electrolytes for use as electrode separators and as binder materials for composite cathodes in rechargeable lithium batteries.

The influence of POSS on the glass transition temperature of various polymers depends heavily on the particular interactions between the filler and the homopolymer. The glass transition temperature may either increase or decrease. For example, creating the hybrid polymer with 2.4 mol % or less of the copolymer poly(hydroxystyrene-co-vinylpyrrolidone-co-isobutylstyryl polyhedral oligosilsesquioxanes) and poly(vinylpyrrolidone) or poly(acetoxystyrene) decreased the glass transition temperature below that of the homopolymer by approximately 10 degrees [45]. In copolymer poly (hydroxystyrene-co-vinylpyrrolidon-co-isobutylstyryl polyhedral oligosilsesquioxane), the addition of an initial 0.8 mol percent POSS leads to a decrease in the glass transition temperature but addition beyond that leads to a steadily increasing T_g. The explanation for the specificity is due to the interactions between the POSS and polymer. If the POSS acts to decrease the self-association between the homopolymers, then a decrease in Tg is observed. If the POSS introduces any strong specific interactions, the Tg increases. With increasing POSS content however, the formation of aggregates, crystallites, and occluded polymer causes an increase in T_g by confining the polymer.

Blends of poly(methyl methacrylate) and acrylic polyhedral oligomeric silsesquioxanes showed clear plasticizing effects on the PMMA [46]. The glass transition temperature and melt-state linear viscoelastic moduli decreased with the addition of POSS to this system. While increases in the storage modulus at temperatures below 0° C at loadings of 20 volume percent were attributed to phase separated domains of POSS which behave like rigid fillers below their glass transition temperature.

The increase in the glass transition temperature seen in tethered POSS systems is attributed to the fact that large masses have been attached to the polymer chain slowing its dynamics and entangling the chains [41]. The addition of blended POSS to a system that already has POSS tethered to the polymer chain decreases dynamics further because associations between the blended POSS and tethered POSS cause a further slowdown in polymer dynamics.

POSS polystyrene copolymers have shown lower viscosities [47] than the homopolymer. Blends of copolymerized POSS poly(methyl methacrylate) with PMMA and PS homopolymers showed increased fracture toughness [48]. This thesis focuses on blended composites of cyclopentyl substituted POSS (CpPOSS, $H_{45}C_{40}Si_8O_{12}$) within a polyethylene matrix.

In the same study [45], creating hybrid polymers with 2.4 mol % POSS and poly(hydroxystyrene) increased the glass transition temperature by approximately 40 degrees. Haddad et al. [49] found that creating copolymers with less than 10 mol % POSS and polystyrene decreased the glass transition temperature by approximately 10-20 degrees, but at higher loading the T_g increased. Xu et al. [50] found that creating poly(vinylphenol-co-vinylpyrrolidone-co-isobutylstyryl polyhedral oligosilsesquioxane) copolymers with differing POSS content showed a monotonic increase in Tg. In all cases, increasing the loading of POSS leads to an increase in the glass transition temperature.

The tendency for POSS to aggregate into small crystalline domains has been observed in numerous experiments [35, 37, 41, 51-53]. It is thought that these aggregates play an important role in the increase of T_g with large POSS loading. Previous attempts [54] to model chemically-tethered cyclohexyl and cyclopentyl POSS nanoparticles to polynorbornene have indicated that well dispersed POSS particles could increase the

polymer's glass transition temperature and increase the material stiffness without the presence of aggregates.

Waddon et al. [52] have created composites of polyethylene and tethered norbornene-cyclopentyl POSS which exhibit a two-phase crystalline structure consisting of PE crystalline domains and POSS crystalline domains. Interestingly, upon melt crystallization during cooling from 180 °C, the POSS particles aggregate first to form a scaffold for subsequent PE crystallization. However, during solvent crystallization in xylene, the PE crystallizes first to form a scaffold for subsequent POSS crystallization. The size of POSS crystals was estimated using the Scherrer equation to have dimensions of approximately 3 – 11 nm.

Studies on the mechanical behavior of the POSS also reveal the importance of the choice of organic pendant groups. The tris(norbornenylethyl)-POSS copolymer with isobutyl pendant groups shows a decrease in elastic moduli, toughness and yield strength with increasing POSS content[55] irrespective of crosslinking density. This is attributed to a decrease in the cohesive energy with increasing POSS content. Huang et al. have found that by adding octa(aminophenyl)silsesquioxane to polyimide, they were able to increase the glass transition of the composite as well as increase stiffness and toughness of the composite[56]. Once again, this suggests that the choice of pendant groups has a significant effect on the mechanical properties also.

Fu et al. [57] have studied the addition of grafted cyclopentyl POSS to polystyrene-polybutadiene-polystyrene (SBS). Interestingly, they grafted the POSS to the polymer chain after polymerization of the chain had already taken place instead of the more common one-pot copolymerization techniques. In this way, they were able to create well dispersed POSS composites with differing POSS content, but identical polymer chain structure. Their dynamic mechanical analysis (DMA) results clearly indicate an increase in the Tg of the polybutadiene block as the POSS filler content is increased from 0 to 20 wt %. The yield stress for the polymer decreases with increasing POSS content, but the composite is significantly tougher. X-ray scattering indicated the presence of some crystalline POSS domains within the composite.

Lamm et al. [58] have simulated the assembly of POSS-like nanostructures. Using lattice Monte Carlo simulations on a coarse grained model of POSS, they were able to

capture the increase in POSS particle spacing with increasing tether length. However, these coarse-grained models cannot capture the interesting features seen in the POSS systems because they lack the detailed interactions between filler and polymer which are the very interactions that give POSS such interesting behavior.

All of these studies suggest that as the length scale of the filler decreases, the interfacial interactions between filler and matrix become increasingly important in determining the global properties of the composite. This thesis will explore in more detail the interface, energetic interactions, and modifications in mechanical and thermal properties that occur with the addition of cyclopentyl POSS in a polyethylene matrix.

Figure 1-1: a) Schematic of the silicate cage. ($R_8Si_8O_{12}$). b) Schematic of the Cyclopentyl (C_5H_9) R-groups used in this study.

a)

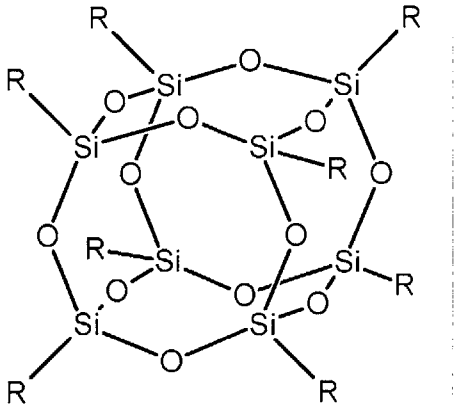

b)

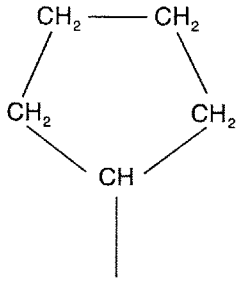

1. Starr, F.W., T.B. Schroder, and S.C. Glotzer, *Molecular dynamics simulation of a polymer melt with a nanoscopic particle.* Macromolecules, 2002. **35**(11): p. 4481-4492.
2. Starr, F.W., T.B. Schroder, and S.C. Glotzer, *Effects of a nanoscopic filler on the structure and dynamics of a simulated polymer melt and the relationship to ultrathin films.* Physical Review E, 2001. **6402**(2).
3. Mansencal, R., B. Haidar, A. Vidal, L. Delmotte, and J.M. Chezeau, *High-resolution solid-state NMR investigation of the filler-rubber interaction: 2. High-speed H-1 magic-angle spinning NMR spectroscopy in carbon-black-filled polybutadiene.* Polymer International, 2001. **50**(4): p. 387-394.
4. Berriot, J., F. Martin, H. Montes, L. Monnerie, and P. Sotta, *Reinforcement of model filled elastomers: characterization of the crosslinking density at the filler-elastomer interface by H-1 NMR measurements.* Polymer, 2003. **44**(5): p. 1437-1447.
5. Berriot, J., H. Montes, F. Martin, M. Mauger, W. Pyckhout-Hintzen, G. Meier, and H. Frielinghaus, *Reinforcement of model filled elastomers: synthesis and characterization of the dispersion state by SANS measurements.* Polymer, 2003. **44**(17): p. 4909-4919.
6. Factor, B.J., T.P. Russell, and M.F. Toney, *Grazing-Incidence X-Ray-Scattering Studies of Thin-Films of an Aromatic Polyimide.* Macromolecules, 1993. **26**(11): p. 2847-2859.
7. Gee, M.L., P.M. McGuiggan, J.N. Israelachvili, and A.M. Homola, *Liquid to Solid-Like Transitions of Molecularly Thin-Films under Shear.* Journal of Chemical Physics, 1990. **93**(3): p. 1895-1906.
8. Vacatello, M., *Monte Carlo simulations of polymer melts filled with solid nanoparticles.* Macromolecules, 2001. **34**(6): p. 1946-1952.
9. Vacatello, M., *Chain dimensions in filled polymers: An intriguing problem.* Macromolecules, 2002. **35**(21): p. 8191-8193.
10. Vacatello, M., *Phantom chain simulations of polymer-nanofiller systems.* Macromolecules, 2003. **36**(9): p. 3411-3416.
11. Bharadwaj, R.K., R.J. Berry, and B.L. Farmer, *Molecular dynamics simulation study of norbornene-POSS polymers.* Polymer, 2000. **41**(19): p. 7209-7221.
12. Nakatani, A.I., W. Chen, R.G. Schmidt, G.V. Gordon, and C.C. Han, *Chain dimensions in polysilicate-filled poly(dimethyl siloxane).* International Journal of Thermophysics, 2002. **23**(1): p. 199-209.
13. Nakatani, A.I., W. Chen, R.G. Schmidt, G.V. Gordon, and C.C. Han, *Chain dimensions in polysilicate-filled poly(dimethyl siloxane).* Polymer, 2001. **42**(8): p. 3713-3722.
14. Yuan, Q.W., A. Kloczkowski, J.E. Mark, and M.A. Sharaf, *Simulations on the reinforcement of poly(dimethylsiloxane) elastomers by randomly distributed filler particles.* Journal of Polymer Science Part B-Polymer Physics, 1996. **34**(9): p. 1647-1657.
15. Christenson, H.K., D.W.R. Gruen, R.G. Horn, and J.N. Israelachvili, *Structuring in Liquid Alkanes between Solid-Surfaces - Force*

Measurements and Mean-Field Theory. Journal of Chemical Physics, 1987. **87**(3): p. 1834-1841.
16. Doruker, P. and W.L. Mattice, *Simulation of polyethylene thin films on a high coordination lattice.* Macromolecules, 1998. **31**(4): p. 1418-1426.
17. Jang, J.H. and W.L. Mattice, *The effect of solid wall interaction on an amorphous polyethylene thin film, using a Monte Carlo simulation on a high coordination lattice.* Polymer, 1999. **40**(16): p. 4685-4694.
18. Jang, J.H. and W.L. Mattice, *A Monte Carlo simulation for the effect of compression on an amorphous polyethylene melt in very thin confined geometry.* Macromolecules, 2000. **33**(4): p. 1467-1472.
19. Theodorou, D.N., *Microscopic Structure and Thermodynamic Properties of Bulk Copolymers and Surface-Active Polymers at Interfaces .2. Results for Some Representative Chain Architectures.* Macromolecules, 1988. **21**(5): p. 1422-1436.
20. Theodorou, D.N., *Microscopic Structure and Thermodynamic Properties of Bulk Copolymers and Surface-Active Polymers at Interfaces .1. Theory.* Macromolecules, 1988. **21**(5): p. 1411-1421.
21. Vacatello, M., *Monte Carlo simulations of polymers in nanoslits.* Macromolecular Theory and Simulations, 2004. **13**(1): p. 30-35.
22. Lichtenhan, J.D., J.J. Schwab, and W.A. Reinerth, *Nanostructured chemicals: A new era in chemical technology.* Chemical Innovation, 2001. **31**(1): p. 3-5.
23. Lichtenhan, J.D., *Polyhedral Oligomeric Silsesquioxanes - Building-Blocks for Silsesquioxane-Based Polymers and Hybrid Materials.* Comments on Inorganic Chemistry, 1995. **17**(2): p. 115-130.
24. Larsson, K., *The crystal structure of Octa-(methylsilsesquioxane).* Arkiv For Kemi, 1960. **16**: p. 203.
25. Larsson, K., *The crystal structure of Octa-(silsesquioxane)(HSiO_1.5)8.* Arkiv For Kemi, 1960. **16**: p. 215.
26. Bassindale, A.R., Z.H. Liu, I.A. MacKinnon, P.G. Taylor, Y.X. Yang, M.E. Light, P.N. Horton, and M.B. Hursthouse, *A higher yielding route for T-8 silsesquioxane cages and X-ray crystal structures of some novel spherosilicates.* Dalton Transactions, 2003(14): p. 2945-2949.
27. Barry, A.J., W.H. Daudt, J.J. Domicone, and J.W. Gilkey, *Crystalline Organosilsesquioxanes.* Journal of the American Chemical Society, 1954. **77**: p. 4248.
28. Larsson, K., *A crystal structure investigation of substituted Octa-(silsesquioxanes) and (ArSiO_1.5)8.* Arkiv For Kemi, 1960. **16**: p. 209.
29. Lichtenhan, J.D., N.Q. Vu, J.A. Carter, J.W. Gilman, and F.J. Feher, *Silsesquioxane Siloxane Copolymers from Polyhedral Silsesquioxanes.* Macromolecules, 1993. **26**(8): p. 2141-2142.
30. Shockey, E.G., A.G. Bolf, P.F. Jones, J.J. Schwab, K.P. Chaffee, T.S. Haddad, and J.D. Lichtenhan, *Functionalized polyhedral oligosilsesquioxane (POSS) macromers: New graftable POSS hydride, POSS alpha-olefin, POSS epoxy, and POSS chlorosilane macromers and*

POSS-siloxane triblocks. Applied Organometallic Chemistry, 1999. **13**(4): p. 311-327.
31. Gilman, J.W., D.S. Schlitzer, and J.D. Lichtenhan, *Low earth orbit resistant siloxane copolymers.* Journal of Applied Polymer Science, 1996. **60**(4): p. 591-596.
32. Lichtenhan, J.D., Y.A. Otonari, and M.J. Carr, *Linear Hybrid Polymer Building-Blocks - Methacrylate-Functionalized Polyhedral Oligomeric Silsesquioxane Monomers and Polymers.* Macromolecules, 1995. **28**(24): p. 8435-8437.
33. Mather, P.T., H.G. Jeon, A. Romo-Uribe, T.S. Haddad, and J.D. Lichtenhan, *Mechanical relaxation and microstructure of poly(norbornyl-POSS) copolymers.* Macromolecules, 1999. **32**(4): p. 1194-1203.
34. Zheng, L., R.M. Kasi, R.J. Farris, and E.B. Coughlin, *Synthesis and thermal properties of hybrid copolymers of syndiotactic polystyrene and polyhedral oligomeric silsesquioxane.* Journal of Polymer Science Part a-Polymer Chemistry, 2002. **40**(7): p. 885-891.
35. Zheng, L., A.J. Waddon, R.J. Farris, and E.B. Coughlin, *X-ray characterizations of polyethylene polyhedral oligomeric silsesquioxane copolymers.* Macromolecules, 2002. **35**(6): p. 2375-2379.
36. Hsiao, B.S., H. White, M. Rafailovich, P.T. Mather, H.G. Jeon, S. Phillips, J. Lichtenhan, and J. Schwab, *Nanoscale reinforcement of polyhedral oligomeric silsesquioxane (POSS) in polyurethane elastomer.* Polymer International, 2000. **49**(5): p. 437-440.
37. Fu, B.X., B.S. Hsiao, S. Pagola, P. Stephens, H. White, M. Rafailovich, J. Sokolov, P.T. Mather, H.G. Jeon, S. Phillips, J. Lichtenhan, and J. Schwab, *Structural development during deformation of polyurethane containing polyhedral oligomeric silsesquioxanes (POSS) molecules.* Polymer, 2001. **42**(2): p. 599-611.
38. Fu, B.X., W.H. Zhang, B.S. Hsiao, M. Rafailovich, J. Sokolov, G. Johansson, B.B. Sauer, S. Phillips, and R. Balnski, *Synthesis and characterization of segmented polyurethanes containing polyhedral oligomeric silsesquioxanes nanostructured molecules.* High Performance Polymers, 2000. **12**(4): p. 565-571.
39. Hottle, J.R., H.J. Kim, J.J. Deng, C.E. Farmer-Creely, B.A. Viers, and A.R. Esker, *Blends of amphiphilic PDMS and trisilanolisobutyl-POSS at the air/water interface.* Macromolecules, 2004. **37**(13): p. 4900-4908.
40. Li, G.Z., L.C. Wang, H. Toghiani, T.L. Daulton, K. Koyama, and C.U. Pittman, *Viscoelastic and mechanical properties of epoxy/multifunctional polyhedral oligomeric silsesquioxane nanocomposites and epoxy/ladderlike polyphenylsilsesquioxane blends.* Macromolecules, 2001. **34**(25): p. 8686-8693.
41. Kopesky, E.T., T.S. Haddad, R.E. Cohen, and G.H. McKinley, *Thermomechanical properties of poly(methyl methacrylate)s containing tethered and untethered polyhedral oligomeric silsesquioxanes.* Macromolecules, 2004. **37**(24): p. 8992-9004.

42. Tegou, E., V. Bellas, E. Gogolides, and P. Argitis, *Polyhedral oligomeric silsesquioxane (POSS) acrylate copolymers for microfabrication: properties and formulation of resist materials.* Microelectronic Engineering, 2004. **73-74**: p. 238-243.
43. Bleha, M., G. Tishchenko, Z. Pientka, and J. Brus, *Effect of POSS (TM) functionality on morphology of thin hybrid chitosan films.* Designed Monomers and Polymers, 2004. **7**(1-2): p. 25-43.
44. Maitra, P. and S.L. Wunder, *POSS based electrolytes for rechargeable lithium batteries.* Electrochemical and Solid State Letters, 2004. **7**(4): p. A88-A92.
45. Xu, H.Y., S.W. Kuo, J.S. Lee, and F.C. Chang, *Glass transition temperatures of poly(hydroxystyrene-co- vinylpyrrolidone-co-isobutylstyry1 polyhedral oligosilsesquioxanes).* Polymer, 2002. **43**(19): p. 5117-5124.
46. Kopesky, E.T., T.S. Haddad, G.H. McKinley, and R.E. Cohen, *Miscibility and Properties of Acrylic Polyhedral Oligomeric Silsesquioxane-Poly(methyl methacrylate) Blends.* 2005.
47. Romo-Uribe, A., P.T. Mather, T.S. Haddad, and J.D. Lichtenhan, *Viscoelastic and morphological behavior of hybrid styryl-based polyhedral oligomeric silsesquioxane (POSS) copolymers.* Journal of Polymer Science Part B-Polymer Physics, 1998. **36**(11): p. 1857-1872.
48. Zhang, W., B.X. Fu, Y. Seo, E. Schrag, B.S. Hsiao, P.T. Mather, N.L. Yang, D. Xu, H. Ade, M. Rafailovich, and J. Sokolov, *Effect of Methyl Methacrylate/Polyhedral Oligomeric Silsesquioxane Random Copolymers in Compatibilization of Polystyrene and Poly(methyl methacrylate) Blends.* Macromolecules, 2002. **35**: p. 8029-8038.
49. Haddad, T.S. and J.D. Lichtenhan, *Hybrid organic-inorganic thermoplastics: Styryl-based polyhedral oligomeric silsesquioxane polymers.* Macromolecules, 1996. **29**(22): p. 7302-7304.
50. Xu, H.Y., S.W. Kuo, and F.C. Chang, *Significant glass transition temperature increase based on polyhedral oligomeric silsequioxane (POSS) copolymer through hydrogen bonding.* Polymer Bulletin, 2002. **48**(6): p. 469-474.
51. Lee, Y.J., S.W. Kuo, W.J. Huang, H.Y. Lee, and F.C. Chang, *Miscibility, specific interactions, and self-assembly behavior of phenolic/polyhedral oligomeric silsesquioxane hybrids.* Journal of Polymer Science Part B-Polymer Physics, 2004. **42**(6): p. 1127-1136.
52. Waddon, A.J., L. Zheng, R.J. Farris, and E.B. Coughlin, *Nanostructured polyethylene-POSS copolymers: Control of crystallization and aggregation.* Nano Letters, 2002. **2**(10): p. 1149-1155.
53. Waddon, A.J. and E.B. Coughlin, *Crystal structure of polyhedral oligomeric silsequioxane (POSS) nano-materials: A study by x-ray diffraction and electron microscopy.* Chemistry of Materials, 2003. **15**(24): p. 4555-4561.
54. Farmer, B.L., R.J. Berry, and R.K. Bharadwaj, *Molecular dynamics simulations of POSS-containing polymers.* Abstracts of Papers of the American Chemical Society, 2001. **222**: p. U186-U186.

55. Constable, G.S., A.J. Lesser, and E.B. Coughlin, *Morphological and mechanical evaluation of hybrid organic-inorganic thermoset copolymers of dicyclopentadiene and mono- or tris(norbornenyl)-substituted polyhedral oligomeric silsesquioxanes.* Macromolecules, 2004. **37**(4): p. 1276-1282.
56. Huang, J.C., C.B. He, Y. Xiao, K.Y. Mya, J. Dai, and Y.P. Siow, *Polyimide/POSS nanocomposites: interfacial interaction, thermal properties and mechanical properties.* Polymer, 2003. **44**(16): p. 4491-4499.
57. Fu, B.X., A. Lee, and T.S. Haddad, *Styrene-butadiene-styrene triblock copolymers modified with polyhedral oligomeric silsesquioxanes.* Macromolecules, 2004. **37**(14): p. 5211-5218.
58. Lamm, M.H., T. Chen, and S.C. Glotzer, *Simulated assembly of nanostructured organic/inorganic networks.* Nano Letters, 2003. **3**(8): p. 989-994.

Chapter 2
Methodology

2.1 Monte Carlo

The Monte Carlo method is a stochastic method which generates configurations of a given system within a particular ensemble. Producing a path through configuration space, it provides no information on the trajectories or velocities of particles. The original formulation is attributed to Metropolis et al. [1].

In atomistic simulations, one is interested in calculating the properties of a given potential function within a certain ensemble. It can be shown that for a NVT ensemble, the probability, p_i, of finding the system in a particular configuration, i, is given by:

$$p_i = \exp\left(-\frac{U\left(\vec{r}^{\,N}\right)}{k_B T}\right) \tag{2.1}$$

where $\vec{r}^{\,N}$ is the set of positions of the particles in the system, U is the potential energy function, and k is Boltzmann's constant.

The average of a property can then be expressed as an integral over degrees of freedom weighted by the probability of finding that state. .

$$\langle A \rangle = \frac{\int d\vec{r}^{\,N} \exp\left(-\frac{U\left(\vec{r}^{\,N}\right)}{k_B T}\right) A\left(\vec{r}^{\,N}\right)}{\int d\vec{r}^{\,N} \exp\left(-\frac{U\left(\vec{r}^{\,N}\right)}{k_B T}\right)} \tag{2.2}$$

where A is the property. For static properties, this average is equivalent to the time average over a single trajectory.

Determining a given property of a system becomes a matter of integrating this function. Only in very rare cases can this integral be evaluated analytically. Resorting to numerical methods, one could randomly sample configurations, calculate the weight and average over the weighted samples. This is inefficient since most of the configurations sampled would be high energy states with low weights. A more efficient way to calculate this ensemble average would be to generate configurations according to the weight $\exp\{-\beta U(\vec{r})\}$. Using this scheme, one samples more frequently those states that contribute most to the average. The property can then be expressed as a simple average of the computed property over the generated states,

$$\langle A \rangle = \frac{1}{N_c} \sum_{j=1}^{N_c} A(r^N) \tag{2.3}$$

where A is the property of interest, and N_c is the number of generated configurations. To sample configurations according to this given weight, Metropolis developed the following algorithm:

1. given an initial configuration $\vec{r}^N$
2. calculate the energy of this state $U_i = U(r^N)$
3. choose an atom at random and perturb it
4. calculate the energy of the perturbed configuration $U_j = U(\vec{r}^N_{new})$
5. if $(U_j - U_i) < 0$ accept the perturbation, otherwise accept configuration with a

probability $\exp\left(-\beta\left(U_j - U_i\right)\right)$

6. calculate property A

7. go to 2.

In addition to the simple single atom displacement move, concerted rotation moves, reptation moves, and molecule displacement/rotation moves were all employed to equilibrate systems. The reptation move [2] is used to disconnect one monomer from the chain end and reattach it to the other end of the chain. This produces a slithering motion of the polymer through the melt. However, the reptation move can be inefficient at changing the internal degrees of freedom for the polymer if long chains are used. The concerted rotation move [3] is used to equilibrate internal segments of polymer chains. The algorithm works by selecting a 10 segment portion of the backbone and displacing 4 of the segments. Molecular translation and rotation were used to take entire molecules and simultaneously translate or rotate all atoms associated with this molecule.

2.2 Molecular Dynamics

Molecular Dynamics is a technique for following the progression of a system of atoms or molecules through phase space. From a given set of initial conditions and interatomic potentials, one can generate the trajectories for particles. Properties can be calculated by averaging over the trajectory:

$$A_\tau = \frac{1}{\tau}\int_0^\tau dtA(t) \qquad (2.4)$$

where A is the property of interest and τ is the time. The key assumption in molecular dynamics is that the movement of atoms can be treated using classical mechanics. If this equation of

motion holds, then the same equations of motion that govern macroscopic objects may be used to model the trajectories of atoms or molecules.

In fact, the motion of all but the lightest of atoms can be treated accurately by classical mechanics even though the interactions between atoms, which is a product of the motion of electrons, must be calculated using quantum mechanics. Luckily, the mass of a nuclei is on the order of ten thousand times that of an electron. The position of the electron is highly non-localized due to its high velocities and low mass and has a short relaxation time. In contrast, the heavier nucleus has a highly localized position and requires much more time to reach its equilibrium state than the electrons encircling it. The two motions can therefore be decoupled and treated independently. This is known as the Born-Oppenheimer Principle. Quantum mechanical calculations can be used to determine the energy of a given configuration of atoms with equilibrated electrons [4]. By varying distances between atoms, a map of the potential energy as a function of configuration can be developed and the motion of large systems of atoms can be calculated without explicitly taking into account the electrons.

By treating the atoms as localized point masses and assuming their interactions are captured in a potential function, one can use Newton's equations of motion to solve for the trajectories of these particles. Recalling that the force on a particle can be written as the negative gradient of the potential, one can then write the equations of motion in the following form:

$$m_i \frac{d^2 \vec{r}_i}{dt^2} = \frac{\partial U\left(\vec{r}^{\,N}\right)}{\partial \vec{r}} \tag{2.5}$$

where m_i and $\vec{r}_i$ are the mass and position of atom I respectively, N is the number of atoms in the simulation, $\vec{r}^N = \{\vec{r}_1, \vec{r}_2, ...\vec{r}_N\}$, and $U(\vec{r}^N)$ is the potential which can be expressed as a function of all other atomic positions. This gives a set of N 2nd order non-linear ordinary differential equations which can only be solved numerically. The corresponding Hamiltonian for this system is given by:

$$H = \sum_{i=1}^{N} \frac{\vec{p}_i^2}{2m_i} + U(\vec{r}^N) \tag{2.6}$$

where $\vec{p}_i$ is the particle momentum.

The Hamiltonian in this case is equivalent to the total energy of the system. Therefore, solving these equations produces a trajectory within an ensemble with a constant number of particles, volume, and energy. This ensemble is termed the microcanonical ensemble (NVE).
If one would like to simulate other ensembles, changes must be made to the equations of motion. To conduct simulations in an ensemble with a constant number of particles, volume, and temperature (NVT) [5-7]. In this formulation, a heat bath is coupled to the equations of motion allowing the transfer of energy to and from the system.

The Verlet algorithm is used to integrate equations of motion for a NVT system. The equations of motion can be similarly modified to sample an ensemble with a constant number of particles, pressure, and temperature (NPT) [8]. The Berendsen algorithm is used [7]. In this formulation, the coupling between motion of the simulation cell is assumed to be weakly coupled to the motion of the particles. This allows the two motions to be integrated separately. The volume and positions of each particle are scaled at each time step in response to stress changes.

$$\begin{aligned}
\bar{\lambda}(t) &= \bar{I} - \frac{\Delta t}{3\tau}\beta\left(\bar{\sigma}(t) - \bar{\sigma}^{o}\right) \\
\bar{s}\left(t+\Delta t\right) &= \bar{\lambda}\bar{s}\left(t\right) \\
\vec{r}_i\left(t+\Delta t\right) &= \bar{\lambda}\vec{r}_i\left(t\right) \\
V\left(t+\Delta t\right) &= \left(\det\bar{\lambda}\right)V\left(t\right)
\end{aligned} \tag{2.7}$$

where $\bar{\lambda}(t)$ is the scaling matrix, τ_P is the time constant, $\bar{\sigma}^{o}$ is the desired stress tensor, $\bar{\sigma}(t)$ is the current stress tensor, Δt is the time step, $\bar{s}$ is the set of vectors defining the shape of the simulation cell, $\vec{r}_i$ is the vector position of particle i, and V is the volume of the simulation cell. This algorithm provides an over-damped response to pressure changes, thereby removing many of the oscillations that would be found using the more rigorous ensemble techniques.

The stress tensor is calculated using the atomic virial [9]. Since periodic boundary conditions are employed, the expression for the virial stress tensor is:

$$\tau^{\alpha\beta} = \left\langle -\frac{1}{V}\sum_i \frac{p_i^{\alpha}\cdot p_i^{\beta}}{m_i} - \frac{1}{2V}\sum_i\sum_j \left(r_i^{\alpha} - r_{j_{\min}(i)}^{\alpha}\right)F_{ij}^{\min,\beta} \right\rangle + \tau_{tail}^{\alpha\beta} \tag{2.8}$$

where V is the volume of the cell, p_i^{α} is the α component of the momentum of the i^{th} particle, m_i is the mass of particle i, r_i^{α} is the α component of the position of the i^{th} particle, $r_{j_{\min}(i)}^{\alpha}$ is the α component of the position of the image of the j^{th} particle which is closest to the i^{th} particle, F_{ij} is the force on i due to j_{min}, and τ_{tail} is the correction to the pressure due to the cutoff radius. The force is defined as $\vec{F}_{ij} = -\nabla_{\vec{r}_i - \vec{r}_j} U\left(\vec{r}^{N}\right)$. The gradient is calculated keeping the separation between all particles other then i and j constant. This does not presuppose pairwise additivity and is applicable to many-body forces. The calculation of long range contributions to the virial stress

tensor and the acceleration can be time consuming. Often interactions beyond a given distance are discarded. When a truncation is used in calculating the contribution of a set of interactions to the pressure, the following correction must be added to the calculated stress:

$$\tau_{tail}^{\alpha\beta} = \delta_{\alpha\beta} \frac{2\pi}{3} \rho^2 \int_{r_c}^{\infty} g(r) \frac{dU_{NB}}{dr} r^3 dr \tag{2.9}$$

where $\delta_{\alpha\beta}$ is the Kroniker delta which is zero if $\alpha \neq \beta$ and is equal to one if $\alpha = \beta$, ρ is the number density, g(r) is the radial distribution function, U_{NB} is the long range potential, and r_c is the cutoff radius.

Assuming that the van der Waals interactions are truncated at r_c and are described by a 12-6 Lennard-Jones potential and that the radial distribution function can be sufficiently approximated as 1 in the region beyond r_c, the equation for the tail correction becomes

$$\tau_{tail}^{\alpha\beta} = \delta_{\alpha\beta} \frac{16\pi}{3} \rho^2 \varepsilon \sigma^3 \left(\frac{2}{3} \left(\frac{\sigma}{r_c} \right)^9 - \left(\frac{\sigma}{r_c} \right)^{12} \right). \tag{2.10}$$

This correction was employed throughout this study. In order to facilitate the computation of the van der Waals interactions, a list of the potential interacting pairs was maintained. Termed a neighbor list, this technique was first used by Verlet [10]. For each atom a list of particles within a distance $d = r_{cutoff} + \delta r$ was maintained. When any particle has moved a distance greater than $\frac{\delta r}{2}$, the list is updated. Due to the constrained motion of particles in the solid phase, this list is valid for a number of time steps.

The link-cell method [11] was used to aid in the creation of neighbor lists. The simulation cell is divided into rectangular compartments whose dimensions are slightly larger then the cutoff distance. Then for a given mer only 27 adjacent compartments must be searched to find neighbors. Since searching for these neighbors requires N^2 work, the link-cell method greatly reduces the computational time required to form the neighbor list.

Due to computational constraints, the particle number in atomistic simulations is severely limited. Surface effects may negatively affect even the largest of simulations. In order to reduce the surface effects, periodic boundary conditions were employed. Atoms or bonds which leave one face of the simulation cell enter the opposite side.

1. Metropolis, N., A. Rosenbluth, M. Rosenbluth, A. Tellar, and M. Tellar, *Equation of state calculations by fast computing machines.* Journal of Chemical Physics, 1953. **21**: p. 1087.
2. Wall, F.T. and F. Mandell, *Macromolecular dimensions obtained by an efficient Monte Carlo method without sample attrition.* Journal of Chemical Physics, 1975. **63**: p. 4592.
3. Dodd, L.R., T.D. Boone, and D.N. Theodorou, *A Concerted Rotation Algorithm for Atomistic Monte-Carlo Simulation of Polymer Melts and Glasses.* Molecular Physics, 1993. **78**(4): p. 961-996.
4. Born, M. and R. Oppenheimer, *Zur Quantentheorie der Molekeln.* Ann. Phys., 1927. **84**(457-484).
5. Nose, S., *A unified formulation of constant temperature molecular dynamics methods.* Journal of Chemical Physics, 1984. **81**(1): p. 511.
6. Hoover, W., *Canonical dynamics: Equilibrium phase-space distributions.* Physical Review A, 1984. **31**: p. 1695.
7. Berendsen, H.J., J.P.M. Postma, W.F.v. Gunsteren, A.D. Nola, and J.R. Haak, *Molecular Dynamics with Coupling to an External Bath.* Journal of Chemical Physics, 1984. **81**: p. 3684-3690.
8. Parrinello, M. and A. Rahman, *Polymorphic transitions in single-crystals - a new molecular-dynamics method.* Journal of Applied Physics, 1981. **52**(12): p. 7182.
9. Theodorou, D.N., T.D. Boone, L.R. Dodd, and K.F. Mansfield, *Stress Tensor in Model Polymer Systems with Periodic Boundaries.* Makromolekulare Chemie-Theory and Simulations, 1993. **2**(2): p. 191-238.
10. Verlet, L., *Computer "Experiments" on Classical Fluids. I. Thermodynamical Properties of Lennard-Jones Molecules.* Physical Review, 1967. **159**(1): p. 98-103.
11. Hocknet, R.W., S.P. Goel, and J.W. Eastwood, *Quite high-resolution computer models of a plasma.* Journal of Computational Physics, 1974. **14**: p. 48.

Chapter 3
Modeling Cyclopentyl POSS

The success or failure of a molecular simulation rests heavily on the description of molecular interactions which are adopted for the particular system being studied. Entire fields for the development of proper interatomic interactions have been developed [1-12]. In most cases, potentials are derived that adequately describe the behavior of a certain set of molecules or monomers, but may do a poor job at describing others even when these molecules consist of the same elements. This occurs because the empirical potential is an approximation to the complex energy surface of the molecule. Changes in bonding, and or changes in the detailed electronic structure of the material may lead to errors when using the potential on different molecules. Although there has been no development of a potential to specifically describe polyhedral oligomeric silsesquioxane, there have been potentials developed for polysilanes [13], polysiloxanes [14], and alkanes [15]. However, their efficacy in describing the molecular properties of polyhedral oligomeric silsesquioxane has not been shown. In the first part of this chapter, we describe the validation of an atomic potential for the simulation of POSS structures by demonstrating that the potential reproduces the vibrational spectra for hydrogenated POSS, and reproduces the crystal structures of cyclopentyl and hydrogenated POSS.

This potential is then used to describe the energetic and mechanical properties of the crystal. As will be described in Chapter 4, the anisotropic properties of the crystal are particularly important in understanding the properties of POSS/polymer nanocomposites due to the presence of small crystalline POSS domains within a variety of polymer matrices. The cohesive energy and the energy required to disperse POSS within the polymer are calculated. This provides clear evidence that there is an energetic driving force towards crystallization in the POSS/polyethylene system.

We also calculate the activation energies for pendant ring rotation for POSS which is perfectly dispersed within the polymer matrix and compare this to ring rotation characteristics of POSS embedded within the crystal. The extra mobility for ring rotation observed in the POSS/polymer system indicates that the rings in contact with polymer are

more mobile than those in the crystal. However, the mobility in the polymer is no faster than the dihedral angle relaxation in the polyethylene. This means that in this system, the ring groups will not act to increase the mobility of the surrounding polymer.

This chapter serves to demonstrate that we can describe observed properties of the POSS particle such as vibrational frequencies and crystal structures using the potential force field presented in this thesis. We then take this molecular description and calculate properties such as cohesive energies, stiffness, and ring dynamics for the cyclopentyl POSS molecule. In Chapter 4, we will use several of these properties to help us understand the behavior of the nanocomposite.

3.1 Model Potential

The POSS particles and polymer were modeled using an explicit atom force field developed by Sun et al. [13-15]. The parameters for this forcefield were originally developed for polysilanes [13], polysiloxanes [14], and alkanes [15]. These three sets of parameters were developed with maximum transferability in mind. In Section 3.2 and 3.3, we will show that they also describe the molecular interactions for the POSS structures well. The functional form of this force field is given by

$$\begin{aligned} E_{total} = & \sum_{b}\sum_{n=2}^{4}\left[k_n(b-b_o)^n\right]+\sum_{\theta}\sum_{n=2}^{4}\left[H_n(\theta-\theta_o)^n\right] \\ & +\sum_{\phi}\sum_{n=1}^{3}\left[V_n\left(1-\cos\left(n\phi-\phi_n^0\right)\right)\right]+\sum_{b,b^*}\left[k^{bb}(b-b_o)(b^*-b_o^*)\right] \\ & +\sum_{b,\theta}\left[k^{b\theta}(b-b_o)(\theta-\theta_o)\right]+\sum_{b,\phi}\left[(b-b_o)\sum_{n=1}^{3}k_n^{b\phi}\cos(n\phi)\right] \\ & +\sum_{\theta,\phi}\left[(\theta-\theta_o)\sum_{n=1}^{3}k_n^{\theta\phi}\cos\left(n\phi\right)\right]+\sum_{\theta,\theta^*}k^{\theta\theta}\left(\theta-\theta_o\right)\left(\theta^*-\theta_o^*\right) \\ & +\sum_{\theta,\theta^*,\phi}k^{\theta\theta\phi}\left(\theta-\theta_o\right)\left(\theta^*-\theta_o^*\right)\cos\phi \\ & +\sum_{i,j}\varepsilon_{ij}\left[2\left(\frac{\sigma}{r}\right)^9-3\left(\frac{\sigma}{r}\right)^6\right]+\sum_{i,j}\frac{q_iq_j}{r_{ij}} \end{aligned} \tag{3.1}$$

where b is a bond length, θ is a bond angle, ϕ is a torsion angle, r_{ij} is the distance between atoms i and j, q_i is the charge on atom i which is calculated using bond increments δ_{ij}.

This potential accounts for both intermolecular and intramolecular interactions. The force field parameters used within this work are defined in Table 3-1 . Any terms which are not found in Table 3-1 can be assumed to be zero.

A 6th order combination law as dictated by Sun's potential [13] was used to calculate the interactions between unlike pairs of atoms:

$$\sigma_{i,j} = \left(\frac{(\sigma_i)^6 + (\sigma_j)^6}{2} \right)^{1/6} \tag{3.2}$$

$$\varepsilon_{i,j} = 2\sqrt{\varepsilon_i \cdot \varepsilon_j} \left(\frac{(\sigma_i)^3 \cdot (\sigma_j)^3}{(\sigma_i)^6 \cdot (\sigma_j)^6} \right). \tag{3.3}$$

The charge on each atom, q_i, was determined using the bond increments, δ_{ij}, given within the forcefield as follows:

$$q_i = \sum_{j=all\ bonded\ atoms} \delta_{ij} \,. \tag{3.4}$$

Using the functional forms in Equation 3.1, the parameters in Table 3-1 were fit to geometric and energetic properties calculated using ab initio calculations. The added complexity of this forcefield, in the form of cross coupling terms, adds additional flexibility to the forcefield that allows it to simultaneously match the energetics, equilibrium geometries, vibrational spectra, and electrostatics for a wide range of molecules. For example, the polysilane [13] potential terms can be used to describe silane, methylsilane, ethylsilane, dimethylsilane, phenyldisilane, and numerous other silane derivatives. In fact, it is precisely the ability of these potential terms to reproduce the equilibrium geometries and vibrational spectra for the POSS molecule that we will test in Section 3.2. The ability of the electrostatic and van der Waals interactions to describe intermolecular interactions is tested in Section 3.3.

Table 3-1. Force field parameters used to model the atoms in the system [13-15].

Atom Type Definitions	
Si	Generic silicon atom with four bonds to non hydrogen atoms attached
O	Generic oxygen atom with two bonds attached
C	Generic sp^3 carbon atom with four bonds attached
H	Generic hydrogen

Quartic Bond

i	j	Ref	b_o(Å)	k_2 (kcal/mol/ Å^2)	k_3 (kcal/mol/ Å^3)	k_4 (kcal/mol/ Å^4)	δ_{ij} (electrons)
Si	C	[13]	1.899	189.65	-279.42	307.51	0.135
Si	H	[13]	1.478	202.78	-305.36	280.27	0.126
O	Si	[14]	1.640	350.1232	-517.3424	673.7067	-0.2225
C	C	[15]	1.530	299.6700	-501.7700	679.8100	0.0000
C	H	[15]	1.101	345.0000	-691.8900	844.6000	-0.0530

Quartic Angle

i	j	k	Ref	θ_o(deg)	H_2 (kcal/mol/rad^2)	H_3 (kcal/mol/rad^3)	H_4 (kcal/mol/rad^4)
H	O	Si	[14]	122.8	23.7764	-19.8152	9.6331
Si	O	Si	[14]	159.0	8.5000	-13.4188	-4.1785
C	Si	O	[14]	114.9	23.0218	-31.3993	24.9814
H	Si	O	[14]	107.4	57.6643	-10.6506	4.6274
O	Si	O	[14]	110.7	70.3069	-6.9375	0.0000
Si	C	H	[13]	112.04	28.7700	-13.950	0.0000
Si	C	C	[13]	112.67	39.5200	-7.4400	0.0000
C	C	C	[15]	112.67	39.5160	-7.4430	-9.5583
C	C	H	[15]	110.77	41.4530	-10.6040	5.1290
H	C	H	[15]	107.66	39.6410	-12.9210	-2.4318

Torsion

i	j	k	l	Ref	V_1 (kcal/mol)	V_2 (kcal/mol)	V_3 (kcal/mol)
Si	O	Si	C	[14]	0.000	0.000	-0.010
Si	O	Si	H	[14]	0.000	0.000	-0.010
Si	O	Si	O	[14]	-0.225	0.000	-0.010
*	O	Si	*	[14]	0.000	0.000	-0.010
*	Si	C	*	[13]	0.000	0.000	-0.070
C	C	C	C	[15]	0.000	0.0514	-0.1430
C	C	C	H	[15]	0.0000	0.0316	-0.1681
H	C	C	H	[15]	-0.1432	0.0617	-0.1530
*	C	C	*	[15]	0.000	0.000	-0.1530

Nonbond (LJ-9-6)

i	Ref	σ (Å)	ε (kcal/mol)
Si	[14]	4.290	0.131
O	[14]	3.300	0.080
C	[15]	3.854	0.0620
H	[15]	2.878	0.0230

Cross Terms Bond-Bond and Bond-Angle

i	j	k	Ref	k^{bb} (i-j/j-k)	$k^{b\theta}$ i-j/i-j-k	$k^{b\theta}$ j-k/i-j-k
C	C	H	[15]	3.3872	20.7540	11.4210
H	C	H	[15]	5.3316	18.1030	18.1030
C	C	C	[15]	0.000	8.0160	8.0160
Si	C	H	[13]	0.000	18.28	16.69
Si	O	Si	[14]	41.1143	28.6686	28.6686
O	Si	O	[14]	41.1143	23.4380	23.4380
H	Si	O	[14]	11.6183	6.4278	20.5669
C	Si	O	[14]	5.4896	6.4278	20.5669

Cross Terms Angle-Angle and Bond-Torsion

i	j	k	l	Ref	i-j-k/j-k-l	$k^{b\phi}$ (i-j/i-j-k-l)			$K^{b\phi}$ (k-l/i-j-k-l)		
						k_1	k_2	k_3	k_1	k_2	k_3
C	C	C	C	[15]	-0.1729	-0.0732	0.0000	0.0000	0.0000	0.0000	0.0000
C	C	C	H	[15]	-1.3199	0.2486	0.2422	-0.0925	0.0814	0.0591	0.2219
H	C	C	H	[15]	-0.4825	0.2130	0.3120	0.0777	0.2130	0.3120	0.0777

Middle Bond-Torsion

i	j	k	l	Ref	$k^{b\phi}$ (j-k/i-j-k-l)		
					k_1	k_2	k_3
C	C	C	C	[15]	-17.7870	-7.1877	0.0000
C	C	C	H	[15]	-14.8790	-3.6581	-0.3138
H	C	C	H	[15]	-14.2610	-0.5322	-0.4864

Cross Terms Angle-Torsion

i	j	k	l	Ref	$k^{\theta\phi}$ (i-j-k/i-j-k-l)			$k^{\theta\phi}$ (j-k-l/i-j-k-l)			$k^{\theta\theta\phi}$
					k_1	k_2	k_3	k_1	k_2	k_3	i-j-k/ i-j-k-l/ j-k-l
C	C	C	C	[15]	0.3886	-0.3139	0.1389	0.3113	0.4516	-0.1988	-16.1640
H	C	C	H	[15]	-0.8085	0.5569	-0.2466	-0.8085	0.5569	-0.2466	-12.5640
C	C	C	H	[15]	-0.2454	0.0000	-0.1136	0.3113	0.4516	-0.1988	0.0000

3.2 Vibrational Frequencies

Since this force field was not originally developed to study POSS molecules, it was necessary to test the ability of the force field to reproduce experimentally observable properties for these molecules. Specifically the equilibrium geometry and the vibrational spectra of octasilsesquioxane were determined. The equilibrium geometry, which is simply the average length of bonds and measure of bond angle for the equilibrated molecule, are reported in Section 3.3. Good agreement between these calculated and experimental properties for a molecule indicates that the force field being used to describe the molecule is capturing the intramolecular interactions between the various elements in the system.

The vibrational spectra and symmetries for each mode for octasilsesquioxane were determined experimentally by Marcolli et al. [16] using both infrared and Raman spectroscopy. For comparison, we calculated the vibrational spectra of a single octasilsesquioxane molecule in a vacuum. Using a lattice dynamics code developed by Lacks and Rutledge [17], the energy of the octasilsesquioxane was minimized with respect to its geometry and then a normal mode analysis was conducted on the molecule. These calculations were conducted at the gamma point using vibrational frequencies calculated using quantum mechanics for the oscillators. Using the computed eigenvectors, the symmetry of each vibrational type was identified and matched with experimentally determined data.

A comparison between the computed vibrational frequencies and those determined experimentally can be found in Table 3-2 and Table 3-3. Experimental frequencies determined via Raman spectroscopy differ from the calculated values by a root mean squared error of 39 cm^{-1}. Frequencies determined via infrared spectroscopy differ from the calculated values by 42 cm^{-1}. This indicates a reasonable agreement between experimental and calculated data for calculations based on the fit potentials employed in this study. Although one can resolve narrow differences in wave number experimentally, computational methods that are not based on quantum mechanics rarely can capture the vibrational spectra with more accuracy.

Looking more closely at the calculated values, one finds that most of the error can be attributed to the representation of the O-Si-H bond angle. If one neglects frequencies

related to bending of this bond angle, shown in Table 3-2 and Table 3-3 in italics, then differences between calculated and experimental frequencies from Raman spectroscopy give a root mean squared error of 8 cm^{-1} and differences between calculated and experimental frequencies from infrared spectroscopy give a root mean squared error of 1.2 cm^{-1}. This excellent agreement indicates that the rigidity of the silicon oxygen bonding within the cubic cage is captured with great accuracy via the adopted force field. This is of particular importance when in Chapter 4 we study the mechanical properties of composites consisting of CpPOSS filled polyethylene since it will affect the elasticity of the filler molecule.

Table 3-2. Computed and experimentally determined Raman spectra[16] for octasilsesquioxane. Modes involving bending of O-Si-H bond angles are shown in italics.

Raman Experiment cm^{-1}	Calculated Modes cm^{-1}	Vibrational Type
2302	2242.8	Si-H
2296	2242.8	Si-H
2286	2242.8	Si-H
1117	1111.3	Si-O-Si
932	*973.44*	*O-Si-H*
897	*973.44*	*O-Si-H*
883	*973.44*	*O-Si-H*
697	687.84	Si-O-Si
610	613.62	Si-O-Si
580	566.3	O-Si-O
456	446.28	O-Si-O
414	410.03	O-Si-O
423	410.03	O-Si-O
352	349.68	O-Si-O
171	174.65	O-Si-O
84	85.895	O-Si-O

Table 3-3. Computed and experimentally determined Infrared Spectra[16] for octasilsesquioxane. Modes involving bending of O-Si-H bond angles are shown in italics.

IR Experiment cm^{-1}	Calculated Modes cm^{-1}	Vibrational Type
2277	2242.8	Si-H
1141	1111.3	Si-O-Si
881	*973.44*	*O-Si-H*
566	566.3	O-Si-O
465	466.4	O-Si-O
399	397.39	O-Si-O

3.3 Crystal Structures

It is not only necessary to show that the intermolecular interactions within a given molecule are correctly represented by the model potential, but one must also demonstrate that the model potential captures the intramolecular interactions. This can be demonstrated by comparing the minimum free energy crystal structure for the molecule using the given potential and that determined experimentally for the same molecule. Good agreement between these indicates a good representation of the intermolecular interactions for the molecule.

Interest in the crystal structure of polyhedral oligomeric silsesquioxane crystal structures dates back to 1960 with early studies by Larsson[18-20]. Larsson [19] determined the crystal structure for octasilsesquioxane, $(HSiO_{1.5})_8$ via x-ray diffraction using Cu-K radiation. The density for the crystal structure was found to be 1.91 g cm^{-3}. The unit cell contains three molecules and has either an R3 or $R\bar{3}$ space group. The crystal parameters can be found in Table 3-4.

The crystal structure for octacyclopentylsilsesquioxane, Table 3-4, was recently determined via x-ray diffraction at 120K by Bassindale et al.[21]. Crystals were formed from a mixture of octacyclopentylsilsesquioxane, dichloromethane, and acetone. The resulting octacyclopentylsilsesquioxane crystal had a density of 1.33 g cm^{-3} and decomposed at less than 400° C without melting. The data for octacyclopentylsilsesquioxane at 120K show that the R groups are all ordered and that they do not rotate at this temperature.

One difficulty in studying the crystal structure of POSS molecules is that the presence of an R group rotational degree of freedom sometimes leads to a phase transition as the temperature is cooled and the available thermal energy falls below the transition energy[18-20]. A rapid and reversible phase transition in $(n\text{-}C_3H_7SiO_{1.5})_8$ was observed at a temperature of -1° C and may be attributable to R group rotational freedom [20]. $(n\text{-}C_3H_7SiO_{1.5})_8$ transitions from a triclinic unit cell at temperatures below -1°C to a hexagonal form at higher temperatures. However, no transitions were noted for octasilsesquioxane or octacyclopentylsilsesquioxane. The x-ray data could not be used to distinguish between rotating R groups and stationary groups which were disordered.

Octasilsesquioxane is a distinct member of the POSS structures because it lacks a rotational degree of freedom for the R groups.

Simulations of the crystal structure of octasilsesquioxane and octacyclopentylsilsesquioxane were studied using a lattice dynamics code developed by Rutledge and Lacks[17]. The initial crystal structure for octasilsesquioxane was built using atomic coordinates taken from Larsson[19], Figure 3-1 , and from Bassindale et al.[21] for Octacyclopentylsilsesquioxane, Figure 3-2. Calculations were conducted over a uniformly distributed k-mesh with 64 total points using frequencies for the oscillators calculated using quantum mechanics.

The lattice dynamics code was used to minimize the free energy of the octasilsesquioxane and octacyclopentylsilsesquioxane structures at 300K and 120K respectively with respect to atomic coordinates and crystal cell parameters. The cell parameters for the minimized structure can be found in Table 3.4. There is less than 5% difference between the calculated and experimental cell parameters for octasilsesquioxane, Table 3-5, and less than 6.4% for those of octacyclopentylsilsesquioxane, Table 3-6. This indicates a relatively good representation of the intermolecular forces in the system.

The equilibrium geometry for octacyclopentylsilsesquioxane is reported in Table 3-7 and compared to experimental data from Bassindale et al. [21]. This again tests the intramolecular interaction terms within the potential and demonstrates that the potential reproduces the shape and size of this molecule.

Table 3-4 – Experimental crystal structures for various POSS molecules.

Compound	Octasilsesquioxane[19]	Octacyclopentylsilsesquioxane[21]
Empirical formula	$H_8O_{12}Si_8$	$C_{40}H_{72}O_{12}Si_8$
M_r [g/mol]	424.74	969.70
T [K]	Room Temperature	120
Crystal System	Hexagonal	Triclinic
Space Group	R3 or R $\bar{3}$	P $\bar{1}$
a [Å]	9.13(1)	9.9936(6)
b [Å]		10.1401(8)
c [Å]	15.35(1)	12.1205(8)
α [°]	90	98.333(6)
β [°]	90	92.328(5)
γ [°]	120	95.545(2)

Table 3-5. Computed minimum free energy cell parameters for octasilsesquioxane.

	Computed	Experimental[19]	Error
a [Å]	9.04	9.13(1)	1.0 %
b [Å]	9.13	9.13(1)	0.03 %
c [Å]	15.77	15.35(1)	2.7 %
α [°]	90	90	0 %
β [°]	90	90	0 %
γ [°]	125.8	120	4.8 %
Volume [$Å^3$]	1054	1108	4.9%

Table 3-6. Computed minimum free energy cell parameters for octacyclopentylsilsesquioxane.

	Computed	Experimental [21]	Error
a [Å]	10.39	9.9936(6)	3.9 %
b [Å]	10.37	10.1401(8)	2.3 %
c [Å]	11.80	12.1205(8)	2.6 %
α [°]	92.0	98.333(6)	6.4 %
β [°]	89.0	92.328(5)	3.9 %
γ [°]	92.9	95.545(2)	2.8 %
Volume [$Å^3$]	1268	1206	5.0%

Table 3-7. Computed and experimental equilibrium Si-O bond length and O-Si-O and O-Si-C bond angles for octacyclopentylsilsesquioxane.

	Computed	Experimental [21]	Error
Si-O [Å]	1.66	1.62	2.4 %
O-Si-O [°]	108.5	108.9	0.4%
O-Si-C [°]	110.4	110.0	0.4%

Figure 3-1. Crystal Structure of Octasilsesquioxane.

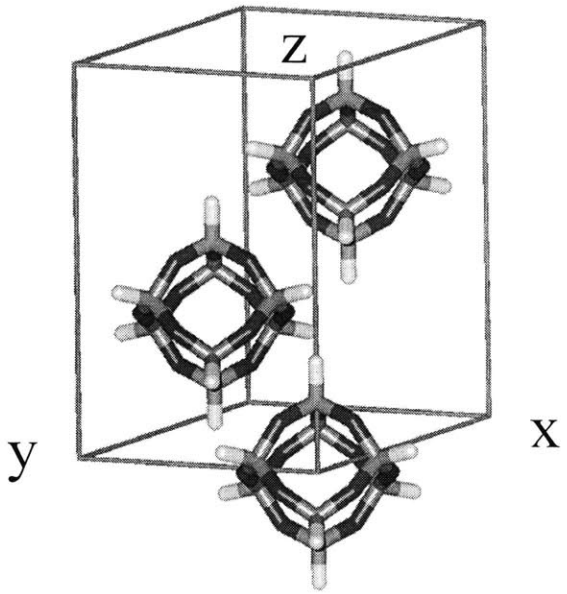

Figure 3-2. Crystal Structure of Octacyclopentylsilsesquioxane.

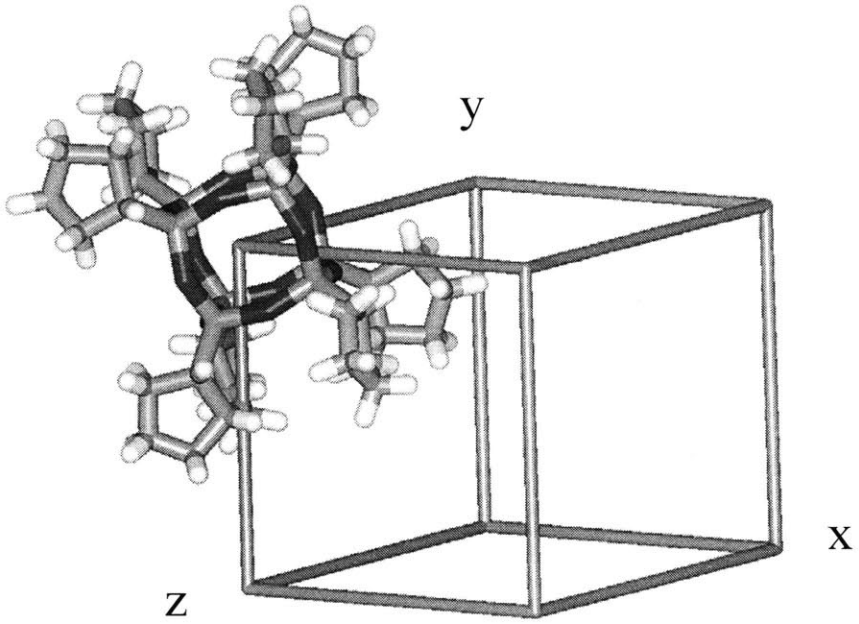

3.4 Mechanical Properties

When determining the behavior of composites, it is essential to characterize fully both the filler and the matrix. The lack of both experimental and computational data on the mechanical properties of POSS structures prevents one from analyzing the properties of polymer/POSS composites using micromechanical models because the elastic properties of the filler (the POSS in this case) are required by these models. The anisotropy of the crystal makes experimental determination of the stiffness tensor particularly difficult. Given that the octacyclopentylsilsesquioxane triclinic unit cell has a P1 symmetry group, there is only a center of inversion as a symmetry operation. For the triclinic unit cell, the stiffness tensor may have 21 independent elastic constants.

The mechanical properties of octacyclopentylsilsesquioxane were determined using molecular dynamics. The crystal structures shown in Table 4-1 were used as initial configurations. Systems were then equilibrated for 500 ps in the NσT ensemble giving the equilibrated cell shape tensor, h_o. Six simulations were run applying a single non-zero component of the stress tensor to the equilibrated crystal cell. In each of the simulations, one of the components σ_{xx}, σ_{xy}, σ_{xz}, σ_{yy}, σ_{yz}, and σ_{zz} was set to 50 MPa while the other 5 were set to zero. Using the perturbed cell shape tensor, h, the strain in the crystal was obtained using the Parinello-Rahman formula[22] as follows:

$$\varepsilon = \frac{1}{2}\left(h_o'^{-1} G h_o^{-1} - I\right) \qquad (3.5)$$
$$G = h'h$$

where ε is the strain tensor. By using the applied stress tensor and the resultant strain tensor, each of these six simulations gives a single row of the compliance tensor, S_{ij}:

$$\varepsilon_i = S_{ij}\sigma_j . \qquad (3.6)$$

Here we are using a Voigt notation to write the stress and strain tensors as 6 component vectors such that

$$\{\sigma\} = \begin{bmatrix} \sigma_{xx} & \sigma_{yy} & \sigma_{zz} & \sigma_{yz} & \sigma_{xz} & \sigma_{xy} \end{bmatrix} \qquad (3.7)$$

$$\{\varepsilon\} = \begin{bmatrix} \varepsilon_{xx} & \varepsilon_{yy} & \varepsilon_{zz} & \gamma_{yz} & \gamma_{xz} & \gamma_{xy} \end{bmatrix} \qquad (3.8)$$

By inverting the compliance tensor, one can obtain the stiffness tensor, C. The resultant stiffness tensor is as follows:

$$C_{ij} = \begin{bmatrix} 16.6 & 5.3 & 6.2 & 3.1 & -0.7 & -5.2 \\ & 20.3 & 5.9 & 0.9 & -4.1 & -0.7 \\ & & 18.1 & 1.2 & 0.5 & 0.2 \\ & & & 7.5 & 0.3 & -1.2 \\ & & & & 9.4 & 3.3 \\ & & & & & 7.7 \end{bmatrix}$$

where all of the terms have units of GPa and the tensor is symmetric such that $C_{ij} = C_{ji}$. Notice that the full fourth order stiffness tensor C_{ijkl} has 81 components but the symmetry conditions, $C_{ijkl} = C_{jikl} = C_{ijlk}$, reduces this to 36 independent components and the symmetry $C_{ijkl} = C_{klij}$ reduces it to 21 independent components. Depending on the symmetry of the unit cell, the stiffness tensor can possess additional symmetry. For example, a triclinic unit cell all 21 components are independent.

$$C_{ij}^{triclinic} = \begin{bmatrix} c_{11} & c_{12} & c_{13} & c_{14} & c_{15} & c_{16} \\ & c_{22} & c_{23} & c_{24} & c_{25} & c_{26} \\ & & c_{33} & c_{34} & c_{35} & c_{36} \\ & & & c_{44} & c_{45} & c_{46} \\ & & & & c_{55} & c_{56} \\ & & & & & c_{66} \end{bmatrix}$$

For an orthorhombic system there are 9 independent components.

$$C_{ij}^{orthorhomic} = \begin{bmatrix} c_{11} & c_{12} & c_{13} & 0 & 0 & 0 \\ & c_{22} & c_{23} & 0 & 0 & 0 \\ & & c_{33} & 0 & 0 & 0 \\ & & & c_{44} & 0 & 0 \\ & & & & c_{55} & 0 \\ & & & & & c_{66} \end{bmatrix}$$

For an isotropic system there are only two independent components.

$$C_{ij}^{\text{isotropic}} = \begin{bmatrix} c_{11} & c_{12} & c_{12} & 0 & 0 & 0 \\ & c_{11} & c_{12} & 0 & 0 & 0 \\ & & c_{11} & 0 & 0 & 0 \\ & & & \frac{1}{2}(c_{11}-c_{12}) & 0 & 0 \\ & & & & \frac{1}{2}(c_{11}-c_{12}) & 0 \\ & & & & & \frac{1}{2}(c_{11}-c_{12}) \end{bmatrix}$$

As stated earlier, the cyclopentyl POSS crystal possesses P1 symmetry and has a triclinic unit cell. This allows for a full 21 independent elastic constants. The results show that there are several non-zero shear coupling terms such as c_{16}, c_{25}, and several others. This indicates that upon the application of shear stress, the unit cell expands along one of the principal axes. The Reuss average isotropic bulk and shear moduli were calculated from the anisotropic compliance tensor using the following formula:

$$\begin{aligned} K_R^{-1} &= \left[S_{11}+S_{22}+S_{33}+2\left(S_{12}+S_{13}+S_{23}\right)\right] \\ G_R^{-1} &= \frac{4}{15}\left[S_{11}+S_{22}+S_{33}-\left(S_{12}+S_{13}+S_{23}\right)+\frac{3}{4}\left(S_{44}+S_{55}+S_{66}\right)\right] \end{aligned} \tag{3.9}$$

Isotropic approximations for familiar values like the Young's Modulus and the shear modulus can be found in Table 3-8. Given that polymer moduli vary on the order of 5 MPa to 2 GPa, the modulus of the CpPOSS crystal is on the order of 10 times, when the matrix is glassy or semicrystalline, to 1000 times, when matrix is rubbery, stiffer than the polymer. This suggests that the POSS when in the form of crystalline aggregates is not necessarily "rigid" in comparison to the polymer and its stiffness must be taken into account in micromechanical models describing the influence of POSS additives on the mechanical properties of composites depending on the polymer in which it is incorporated. For the stiffer glassy polymers, the POSS stiffness must be accounted for. Also the order of magnitude of c_{11} falls in the range of that determined experimentally for many other organic crystals reported in Table 3-9. Although the CpPOSS cage is quite rigid as seen by the computed and experimental vibrational spectra, the interactions between stiff cages is mediated by the compliant pendant organic groups. The strong interactions between ions which result in high moduli in ionic crystals are much stiffer

than the van der Waals interactions and the octapole interactions between the silicon-oxygen cages. Because of this, the molecular crystal is always more compliant than the ionic atomic crystal, Table 3-9.

Table 3-8: Isotropic approximations for cyclopentyl POSS crystal elastic properties.

Term	Value
Bulk Modulus, K_R	7.5 [GPa]
Elastic Modulus, E_R	11.78 [GPa]
Poisson's Ratio, ν_R	0.24
Shear Modulus, G_R	4.75 [GPa]

Table 3-9: Experimental elastic constants for other organic crystals.

Organic Crystal	C_{11} [GPa]	C_{22} [GPa]	C_{33} [GPa]	C_{44} [GPa]	C_{55} [GPa]	C_{66} [GPa]	C_{12} [GPa]	C_{13} [GPa]	C_{23} [GPa]	C_{35} [GPa]
Urea [23]	21.7	21.7	53.2	6.26	6.26	0.45	8.9	24.0	24.0	
Hexamethylenetetramine [24]	15			7			3			
pentacrythritol[25]	40.5		13.9	2.74		2.52	26.6	10.5		
Rescorcinol[26]	8.6	28.8	19.5	3.26	4.35	4.00	9.5	7.5	19.1	
m-dinitrobenzene [27]	10.7	11.3	20.3	4.37	2.04	5.31	6.30	1.95	3.19	
durene[28]	9.08	10	10	1.84	2.17	7.27	7.75	2.57	3.19	-0.13

3.5 CpPOSS Cohesive Energy

The cohesive energy of the crystal was found at 200K, 250K, and 300K. The larger the cohesive energy, the stronger the interactions between molecules within the crystal and the more stable the crystal. Additionally, since the mesostructure of the nanocomposite can play a significant role in determining its properties, it is important to understand the energetics of CpPOSS crystallization within the composite. Aggregation and the formation of crystallites within the nanocomposite is driven by energetic interactions between the CpPOSS molecules, between the CpPOSS molecules and the polymer, and entropic penalties for aggregation. The energetic driving force for crystallization within the POSS/Polyethylene composite may be assessed by directly comparing the energy of a CpPOSS particle within a crystal and that of a CpPOSS particle embedded in the polyethylene matrix.

The cohesive energy, $U_{cohesive}$, is determined by the following equation:

$$U_{cohesive} = U_{System} - \sum_{n=1}^{N_{molecules}} U_n^{vacuum} \tag{3.10}$$

where U_{system} is the total energy of the simulated system, and U_n^{vacuum} is the energy of each molecule in vacuum. Simulations were carried out on a) an infinite CpPOSS crystal, b) a single CpPOSS molecule in a vacuum, and c) a single CpPOSS molecule embedded within a polymer. Each simulation was run for 3 nanoseconds in the NσT ensemble and the energy of the CpPOSS molecule was averaged over the last 2 nanoseconds of the run. The system energy, U_{system}, in equation 3.10 is the energy of the infinite crystal. The energy of individual isolated POSS molecules is taken from system b) a single CpPOSS molecule in a vacuum. The resulting cohesive energy is reported in Table 3-10. This term is also converted into a cohesive energy density, δ, by taking the square root of the cohesive energy density divided by the volume of the unit cell as follows:

$$\delta = \sqrt{\frac{U_{cohesive}}{V}} \tag{3.11}$$

where V is the volume of the simulation cell. This volume is given by the determinant of the system shape matrix, h. The experimentally determined cohesive energy density for several other material systems is given in Table 3-11.

In addition, the energetic penalty for dispersing the CpPOSS into the polymer was determined by subtracting the energy of the CpPOSS molecule in system c, the CpPOSS/PE system, and the energy of a CpPOSS in system a, the CpPOSS crystal. The energy required for dispersion, $U_{dispersion}$, is given by:

$$U_{dispersion} = U_{crystal}^{POSS} - U_{dispersed}^{POSS} \tag{3.12}$$

where $U_{crystal}^{POSS}$ is the energy of a CpPOSS molecule in a perfect crystal, and $U_{dispersion}^{POSS}$ is the energy of a CpPOSS molecule perfectly dispersed in a polyethylene matrix. This quantity is reported in Table 3-12. It is much more difficult to define an energy density for the dispersed molecule simply because the volume for a single molecule is ill defined. The boundary defining the volume enclosed by a given atom can be arbitrarily chosen as the van der Waals radii, the repulsive part of the van der Waals interaction, or any other arbitrary value. This problem is discussed in more detail in Chapter 4.

In order to determine whether the POSS will aggregate within the polymer matrix it is necessary to know both the energetic driving force for aggregation and crystallization and the entropic penalty for dispersing the POSS. Table 3-12 shows that it is clearly energetically favorable for crystallization to occur. However, this data is not sufficient to predict aggregation. Since it is entropically favorable for the CpPOSS to be in the dispersed state, the energetic driving force is necessary for crystallization. Simulations of CpPOSS/PE composites will later show that the aggregated state is preferred in this system.

As a very rough estimate, we can approximate the entropy of dispersion by treating the nanoparticles as an ideal gas. In this case the change in entropy between two states at constant temperature is given by:

$$\Delta S = Nk \ln \frac{V_f}{V_i} \tag{3.13}$$

where N is the number of atoms, k is the Boltzmann's constant, V_f is the final volume, and V_i is the initial volume. The final state is the crystalline state, and the initial state is the dispersed state. The volume of the crystal is approximately 36 times the volume of a

5 wt % dispersed nanocomposite. In this case, the entropy of the crystal is lower than the entropy of the dispersed state by 0.029 kJ/mol. This is significantly smaller than the order 100 kJ/mol differences in internal energy between these two states.

Figure 3-3: CpPOSS in a vacuum.

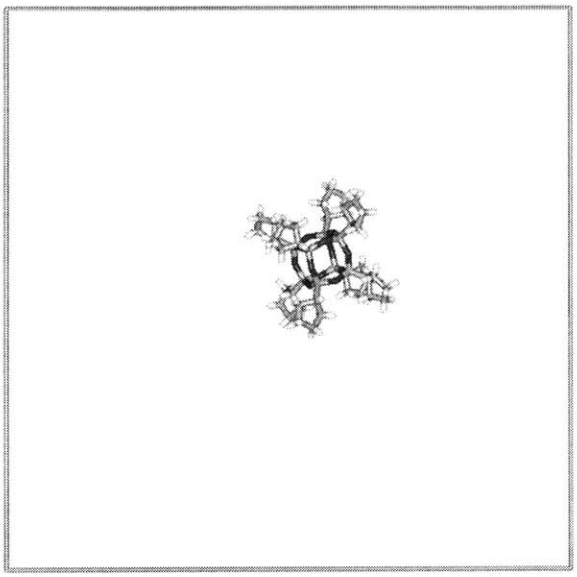

Figure 3-4: Single CpPOSS embedded within a Polyethylene matrix.

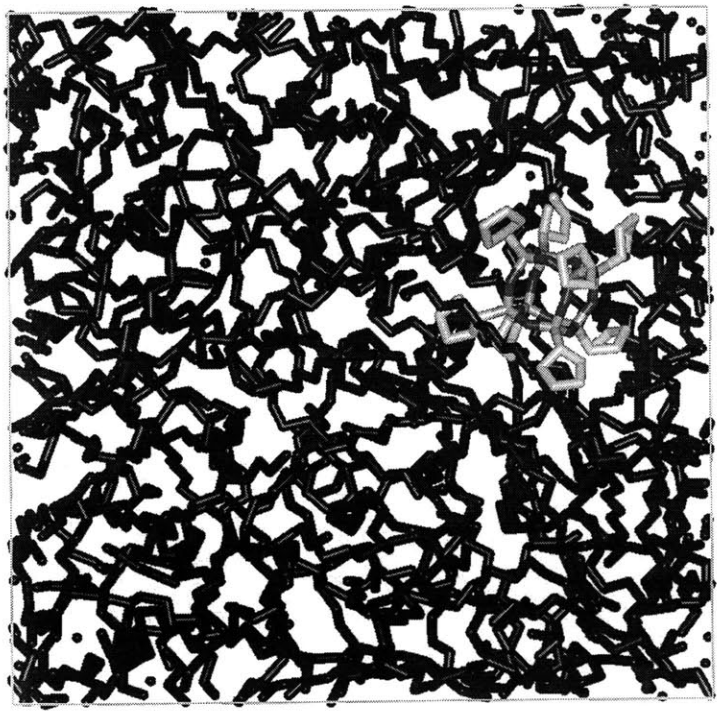

Table 3-10: CpPOSS cohesive energy at various temperatures.

Simulation Set	300 K	250K	200 K
$U_{cohesive}$ [kJ/mol]	$-1.0(6) \times 10^3$	$-1.4(4) \times 10^3$	$-1.8(4) \times 10^3$
δ [cal/cc]$^{1/2}$	38.1	42.9	51.5

Table 3-11: Experimentally determined Hildebrand solubility parameters [29].

Material	δ [cal/cc]$^{1/2}$
Polystyrene	34-42
Nylon 6.6	56
Polybutadiene	29-35
Polyethylene	30-39

Table 3-12: Energy difference between crystallized CpPOSS and CpPOSS dispersed in polyethylene.

Simulation Set	300K	250K	200K
$U_{dispersion}$ [kJ/mol]	$-6.0(6) \times 10^2$	$-1.0(4) \times 10^3$	$-1.4(4) \times 10^3$

3.6 Ring Dynamics

We are also interested in the dynamics of the cyclopentyl R groups because these interact directly with the polymer surrounding the POSS cage. The fast dynamics and flexibility of the ring group have even been associated with a decrease in the glass transition temperature of the blended POSS polymer composites[30]. Understanding the difference in dynamics between the ring group and segmental mobility of the polymer backbone will help us to understand the effects of incorporating POSS into the polymer. In polymers where the ring group rotation is faster than segmental motion within the polymer, it is expected that the polymer in contact with the ring group will have increased dynamics. If the ring group rotation and POSS mobility is much slower than the segmental motion within the polymer, then the surface of the POSS may act much like a flat static wall in the presence of the more mobile polymer.

The rotational dynamics of the cyclopentyl ring groups were determined by monitoring the dihedral angle formed between the silicon-oxygen-carbon-carbon atoms. The following dihedral angle autocorrelation function, $\phi_{DACF}(t)$, was calculated:

$$\phi_{DACF}(t) = \frac{\langle \cos(\phi(t)) \cdot \cos(\phi(0)) \rangle - \langle \cos(\phi(0)) \rangle^2}{\langle \cos^2(\phi(0)) \rangle - \langle \cos(\phi(0)) \rangle^2} \tag{3.14}$$

where ϕ is the dihedral angle, and t is the time. The following three systems were studied a) a single CpPOSS particle in a vacuum, b) an infinite CpPOSS crystal, and c) CpPOSS dispersed in a polyethylene matrix. The resulting curves can be seen in Figure 3-5, 3-6, and 3-7.

The relaxation time for each of these dihedral angle autocorrelation functions was determined by fitting a William-Watts stretched exponential[31] to each curve using a least squares method.

$$\phi_{DACF}(t) = \exp\left(-\left(\frac{t}{\tau_{DACF}} \right)^{\beta} \right) \tag{3.15}$$

Assuming an Arrhenius relation between the DACF relaxation time and the temperature, an activation energy for ring rotation was determined as follows:

$$\frac{\tau_{DACF}}{\tau_o} = \exp\left(\frac{-E_a}{RT}\right) \tag{3.16}$$

where E_a is the activation energy, τ_o is a constant, R is the gas constant, and T is the temperature. The results can be found in Table 3-8.

In a vacuum, the rotational relaxation of the ring groups is quite fast. It is significantly faster than the relaxation of the segments along the polymer backbone. When placed into the polymer matrix, the relaxation times decrease and the activation energy of 13 kJ/mol approaches the activation energy for dihedral angle rotation along the backbone of the polymer chain. In the crystal, the ring rotation is very slow.

The change in ring dynamics depends significantly on the material surrounding the particle. In a polyethylene matrix, we find that the ring group rotation is no faster than the segmental motion along the polymer backbone. In a polymer with slower segmental mobility, due perhaps to ring groups, or bulky side groups, it is presumed that the ring group mobility would be faster than the polymer segmental mobility. In Chapter 4, it will be shown that blending the CpPOSS to short chains of polyethylene actually increases the glass transition temperature. The common plasticizing effect of blended POSS is not seen in the computational studies. This may be due in part to the fact that the ring group rotation does not contribute additional mobility to the system in which it is added.

Figure 3-5: Figure illustrating the dihedral angle that is being monitored. The dihedral angle being monitored is indicated by the arrow.

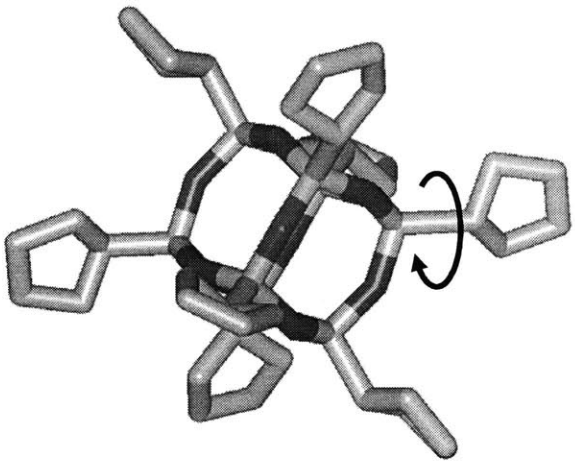

Figure 3-6: Dihedral angle autocorrelation functions for a single CpPOSS particle in a vacuum.

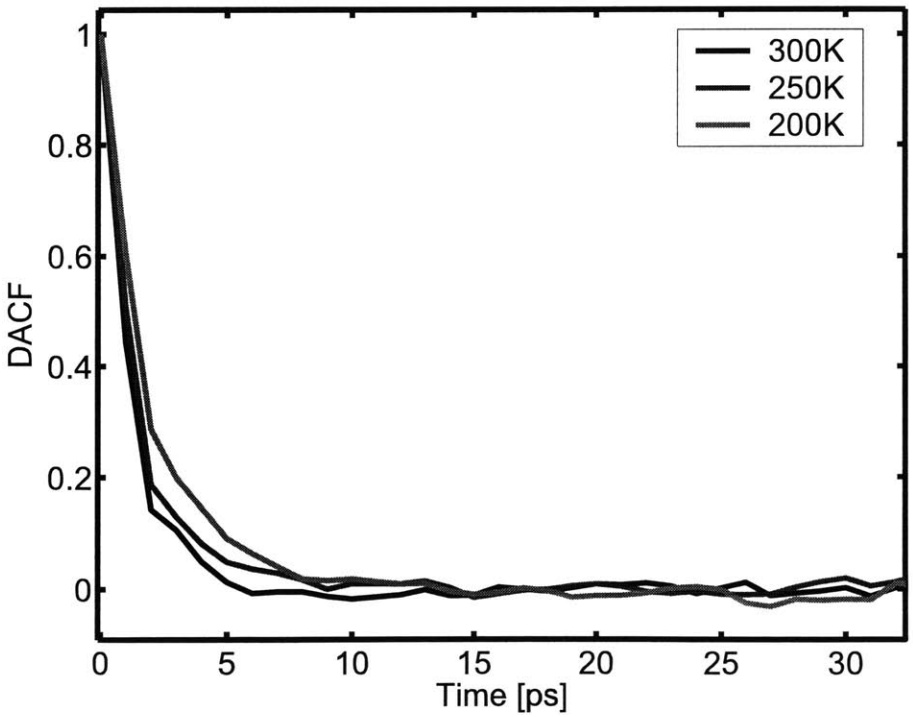

Figure 3-7: Dihedral angle relaxation times for CpPOSS in a vacuum.

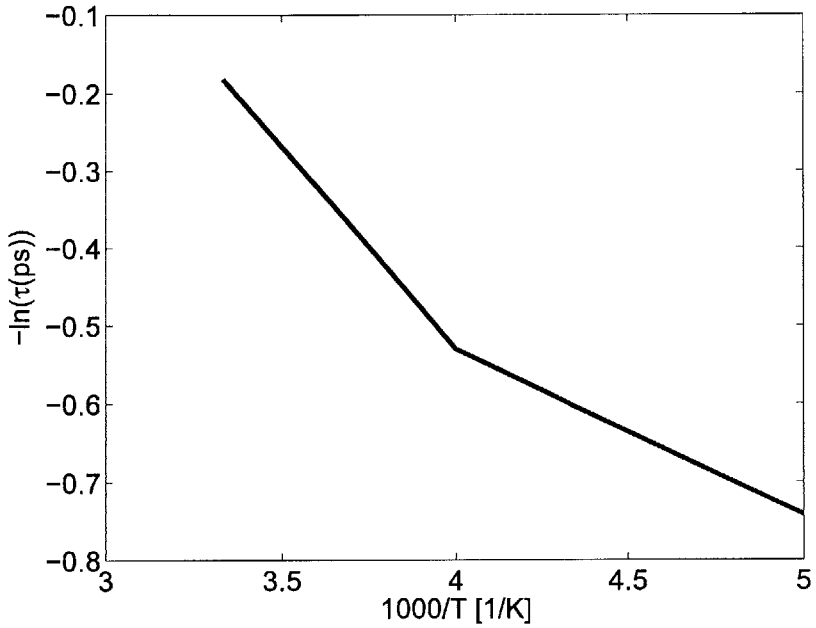

Figure 3-8: Dihedral angle autocorrelation functions for an infinite CpPOSS crystal.

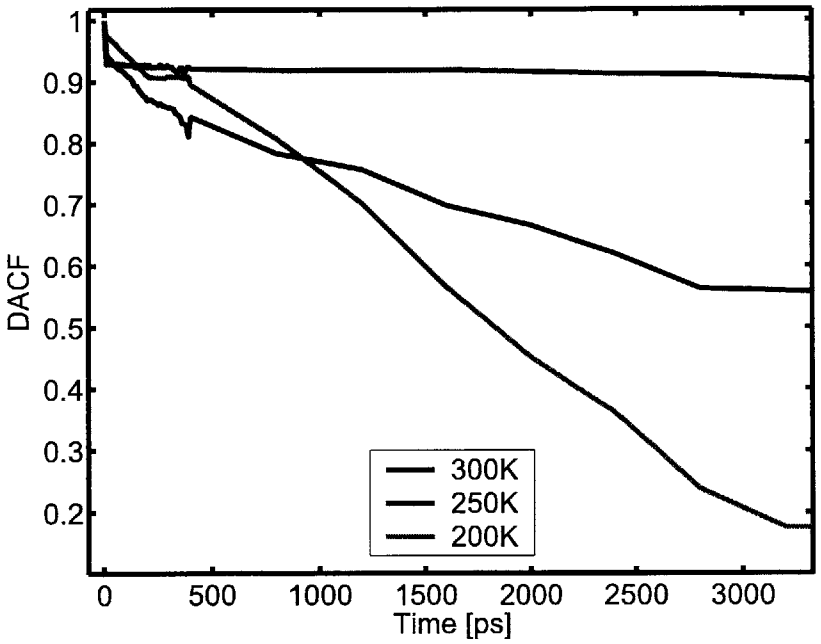

Figure 3-9: Dihedral angle autocorrelation functions for a PE/CpPOSS composite.

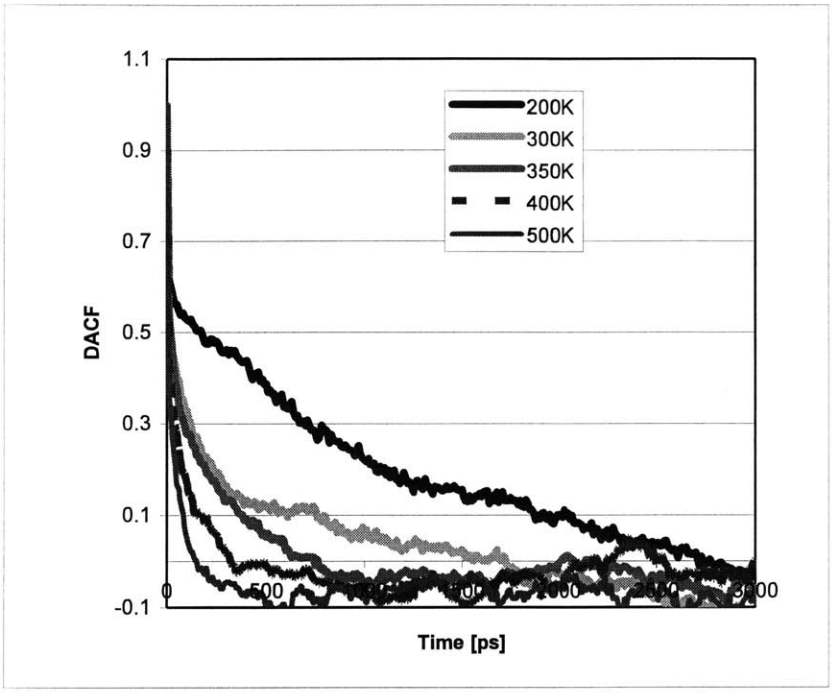

Figure 3-10: Dihedral angle relaxation times for PE/CpPOSS composite.

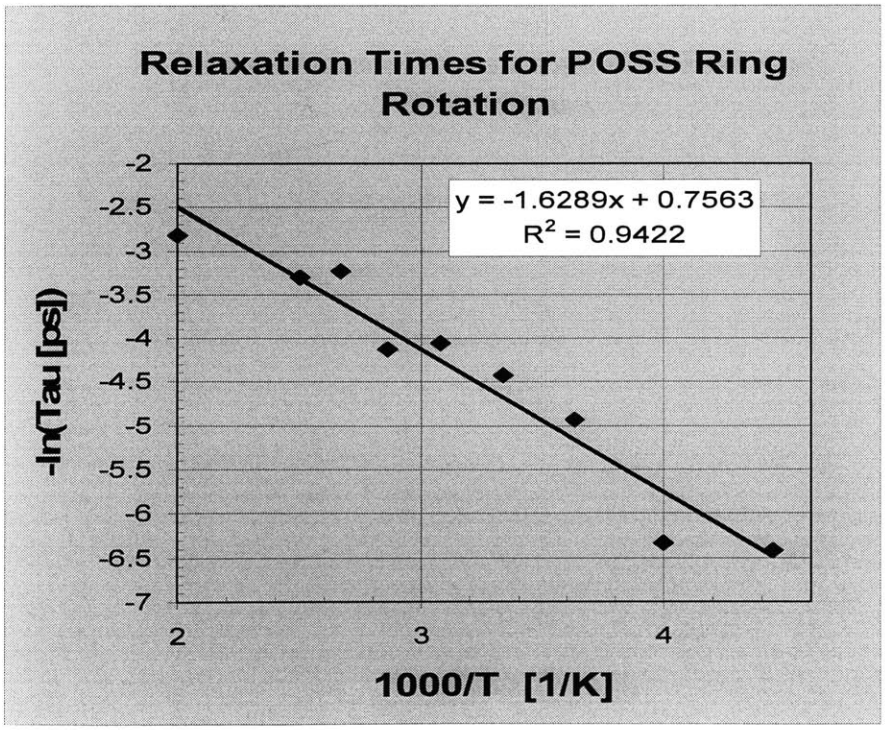

Table 3-13: Activation energies for ring group rotation in CpPOSS.

System	Activation Energy for Ring Rotation [kJ/mol]
Isolated CpPOSS	2.7
CpPOSS dispersed in PE	13.5

3.7 Discussion

In this chapter, we have demonstrated that the force field developed by Sun et al. [13-15] adequately describes the intermolecular and intramolecular interactions in the POSS molecule. The ability of this forcefield to reproduce the crystal structures and vibrational spectra for the POSS molecule indicate that we have captured the rigidity of the molecule and intramolecular interactions well. However, calculations of the elastic moduli of the CpPOSS crystal reveal that the rigidity of the central silicon-oxygen cage within the CpPOSS molecule does not translate into high stiffness for the CpPOSS crystal. The interactions between the flexible organic cyclopentyl R-groups add compliance to the crystal and the measured stiffness is on the order of 15 GPa. This is not terribly stiff compared to the polymers they are blended with which have elastic moduli on the order of 1 – 2 GPa. Note that the calculated elastic modulus was for a crystal of CpPOSS and not for a single molecule embedded within a polymer. In Chapter 4, we will examine the enhancement of moduli that occurs with the addition of CpPOSS to the polyethylene matrix. These properties will be used in Chapter 4 to use micromechanical models to describe the change in mechanical properties of the CpPOSS/PE blends.

Comparing the energy of the crystalline POSS to that of a POSS molecule perfectly dispersed in the polymer, one finds that there is an energetic driving force towards crystallization of the CpPOSS in the CpPOSS/PE composite system. In Chapter 4, we will show how this energetic driving force leads to aggregation within the simulated CpPOSS/PE composites. In fact, the presence of crystallites of POSS within POSS/polymer has been observed[32-34]. In the case of tethered POSS, the chemical constraint forces the POSS to crystallize into raft like structures[32, 35-41]. Due to the presence of these highly organized and crystallized POSS domains, the mechanical properties and energetics of the POSS crystal are critical to understanding the behavior of the nanocomposites themselves.

A decrease in the glass transition temperature has been observed with the addition of small amounts of POSS in a polymer[34, 42]. This decrease may be attributed to a plasticization of the polymer by the POSS particle. In this chapter, we have shown that

the mobility of the ring groups in the polymer is on the same order of magnitude as segmental motion within the polymer chain. In Chapter 4, we will also show that the mobility of the CpPOSS particles is actually slower than the mobility of the PE chains studied in our simulations. This means that the blended POSS will not act to enhance the mobility of our system, and the CpPOSS/PE system we study is perhaps analogous to the tethered POSS systems. In the tethered systems, the addition of large immobile POSS structures into the system leads to increases in the glass transition temperature and decreases in polymer mobility due to confinement effects.

1. Borodin, O., G.D. Smith, and R. Douglas, *Force field development and MD simulations of poly(ethylene oxide)/LiBF4 polymer electrolytes.* Journal of Physical Chemistry B, 2003. **107**(28): p. 6824-6837.
2. Kirschner, K.N., A.H. Lewin, and J.P. Bowen, *Molecular mechanics force-field development for amino acid zwitterions.* Journal of Computational Chemistry, 2003. **24**(1): p. 111-128.
3. Todebush, P.M., G. Liang, and J.P. Bowen, *Molecular mechanics (MM4) force field development for phosphine and its alkyl derivatives.* Chirality, 2002. **14**(2-3): p. 220-231.
4. Yang, J., Y. Ren, A.M. Tian, and H.A. Sun, *COMPASS force field for 14 inorganic molecules, He, Ne, Ar, Kr, Xe, H-2, O-2, N-2, NO, CO, CO2, NO2, CS2, and SO2, in liquid phases.* Journal of Physical Chemistry B, 2000. **104**(20): p. 4951-4957.
5. Faller, R., H. Schmitz, O. Biermann, and F. Muller-Plathe, *Automatic parameterization of force fields for liquids by simplex optimization.* Journal of Computational Chemistry, 1999. **20**(10): p. 1009-1017.
6. Fisher, L.S. and T.A. Holme, *Molecular mechanics (MM3) force field development for tetravalent boron containing compounds.* Abstracts of Papers of the American Chemical Society, 1999. **217**: p. U684-U684.
7. Kirschner, K.N., A.H. Lewin, and J.P. Bowen, *Molecular mechanics force field development for amino acid zwitterions and zwitterionic drugs.* Abstracts of Papers of the American Chemical Society, 1998. **216**: p. U717-U717.
8. Sun, H., *Integrated force field development for applications in materials science.* Abstracts of Papers of the American Chemical Society, 1998. **216**: p. U743-U743.
9. Tenette, C., J.C. Smith, and C.M. Topham, *Force field development and conformational search strategy in the simulation of biomolecular recognition processes.* Biochemical Society Transactions, 1996. **24**(1): p. 268-274.
10. Mackerell, A.D., *Empirical Force-Field Development and Validation for Computational Studies of Biological-Membranes.* Abstracts of Papers of the American Chemical Society, 1994. **208**: p. 18-COMP.
11. Brady, J.W., *Force-Field Development for Carbohydrates and Polysaccharides.* Abstracts of Papers of the American Chemical Society, 1992. **203**: p. 4-CELL.
12. Kollman, P.A. and K.A. Dill, *Decisions in Force-Field Development - an Alternative to Those Described by Roterman Et-Al.* Journal of Biomolecular Structure & Dynamics, 1991. **8**(6): p. 1103-1107.
13. Sun, H., *Ab-Initio Calculations and Force-Field Development for Computer-Simulation of Polysilanes.* Macromolecules, 1995. **28**(3): p. 701-712.
14. Sun, H. and D. Rigby, *Polysiloxanes: Ab initio force field and structural, conformational and thermophysical properties.* Spectrochimica Acta Part a-Molecular and Biomolecular Spectroscopy, 1997. **53**(8): p. 1301-1323.
15. Sun, H., *COMPASS: An ab initio force-field optimized for condensed-phase applications - Overview with details on alkane and benzene compounds.* Journal of Physical Chemistry B, 1998. **102**(38): p. 7338-7364.

16. Marcolli, C., P. Laine, R. Buhler, G. Calzaferri, and J. Tomkinson, *Vibrations of H8Si8O12, D8Si8O12, and H10Si10O15 as determined by PNS, IR, and Raman experiments.* Journal of Physical Chemistry B, 1997. **101**(7): p. 1171-1179.
17. Lacks, D.J. and G.C. Rutledge, *Simulation of the Temperature-Dependence of Mechanical- Properties of Polyethylene.* Journal of Physical Chemistry, 1994. **98**(4): p. 1222-1231.
18. Larsson, K., *The crystal structure of Octa-(methylsilsesquioxane).* Arkiv For Kemi, 1960. **16**: p. 203.
19. Larsson, K., *The crystal structure of Octa-(silsesquioxane)(HSiO_1.5)8.* Arkiv For Kemi, 1960. **16**: p. 215.
20. Larsson, K., *A crystal structure investigation of substituted Octa-(silsesquioxanes) and (ArSiO_1.5)8.* Arkiv For Kemi, 1960. **16**: p. 209.
21. Bassindale, A.R., Z.H. Liu, I.A. MacKinnon, P.G. Taylor, Y.X. Yang, M.E. Light, P.N. Horton, and M.B. Hursthouse, *A higher yielding route for T-8 silsesquioxane cages and X-ray crystal structures of some novel spherosilicates.* Dalton Transactions, 2003(14): p. 2945-2949.
22. Parrinello, M. and A. Rahman, *Strain Fluctuations and Elastic-Constants.* Journal of Chemical Physics, 1982. **76**(5): p. 2662-2666.
23. Fischer, G. and A. Zarembowitch, Seances Academy of Sciences, Ser. B, 1970. **270**: p. 852.
24. Ramachandran, G.N. and W.A. Wooster, Acta Crystallographica, 1951. **4**: p. 431.
25. Nomura, H., K. Higuchi, S. Kato, and Y. Miyahara, Japan Journal of Applied Physics, 1972. **11**: p. 304.
26. Koptsik, V.A., Kristallografiia, 1959. **4**: p. 219.
27. Mitsui, T. and K. Ilo, Japan Journal of Applied Physics, 1980. **19**: p. 2511.
28. Sanquer, M. and C. Ecolivet, *Elastic Constants in Molecular Crystals*, in *Dynamics of Molecular Crystals*. 1987, Elsevier: Amsterdam.
29. Brandrup, J. and E.H. Immergut, eds. *Polymer Handbook*. 3rd ed. 1989, Wiley-Iterscience: New York.
30. Pellice, S.A., D.P. Fasce, and R.J.J. Williams, *Properties of Epoxy Networks Derived from the Reaction of Diglycidyl Ether of GBisphenol A with Polyhedral oligomeric Silsesquioxanes Bearing OH-Functionalized Organic Substituents.* Journal of Polymer Science Part B-Polymer Physics, 2003. **41**: p. 1451-1461.
31. Williams, G., D.C. Watts, S.B. Dev, and A. North, Transactions of the Faraday Society, 1971. **67**: p. 1323.
32. Zheng, L., A.J. Waddon, R.J. Farris, and E.B. Coughlin, *X-ray characterizations of polyethylene polyhedral oligomeric silsesquioxane copolymers.* Macromolecules, 2002. **35**(6): p. 2375-2379.
33. Phillips, S.H., T.S. Haddad, and S.J. Tomczak, *Developments in nanoscience: polyhedral silsesquioxane (POSS)-polymers oligomeric.* Current Opinion in Solid State & Materials Science, 2004. **8**(1): p. 21-29.
34. Kopesky, E.T., T.S. Haddad, R.E. Cohen, and G.H. McKinley, *Thermomechanical properties of poly(methyl methacrylate)s containing tethered and untethered polyhedral oligomeric silsesquioxanes.* Macromolecules, 2004. **37**(24): p. 8992-9004.

35. Cardoen, G. and E.B. Coughlin, *Hemi-telechelic polystyrene-POSS copolymers as model systems for the study of well-defined inorganic/organic hybrid materials.* Macromolecules, 2004. **37**(13): p. 5123-5126.
36. Constable, G.S., A.J. Lesser, and E.B. Coughlin, *Morphological and mechanical evaluation of hybrid organic-inorganic thermoset copolymers of dicyclopentadiene and mono- or tris(norbornenyl)-substituted polyhedral oligomeric silsesquioxanes.* Macromolecules, 2004. **37**(4): p. 1276-1282.
37. Waddon, A.J., L. Zheng, R.J. Farris, and E.B. Coughlin, *Nanostructured polyethylene-POSS copolymers: Control of crystallization and aggregation.* Nano Letters, 2002. **2**(10): p. 1149-1155.
38. Waddon, A.J. and E.B. Coughlin, *Crystal structure of polyhedral oligomeric silsequioxane (POSS) nano-materials: A study by x-ray diffraction and electron microscopy.* Chemistry of Materials, 2003. **15**(24): p. 4555-4561.
39. Zheng, L., R.J. Farris, and E.B. Coughlin, *Novel polyolefin nanocomposites: Synthesis and characterizations of metallocene-catalyzed polyolefin polyhedral oligomeric silsesquioxane copolymers.* Macromolecules, 2001. **34**(23): p. 8034-8039.
40. Zheng, L., R.M. Kasi, R.J. Farris, and E.B. Coughlin, *Synthesis and thermal properties of hybrid copolymers of syndiotactic polystyrene and polyhedral oligomeric silsesquioxane.* Journal of Polymer Science Part a-Polymer Chemistry, 2002. **40**(7): p. 885-891.
41. Zheng, L., S. Hong, G. Cardoen, E. Burgaz, S.P. Gido, and E.B. Coughlin, *Polymer nanocomposites through controlled self-assembly of cubic silsesquioxane scaffolds.* Macromolecules, 2004. **37**(23): p. 8606-8611.
42. Kopesky, E.T., T.S. Haddad, G.H. McKinley, and R.E. Cohen, *Miscibility and Properties of Acrylic Polyhedral Oligomeric Silsesquioxane-Poly(methyl methacrylate) Blends.* 2005.

Chapter 4
CpPOSS/Polyethylene Nano-composites

In recent years, there has been significant interest in polyhedral oligomeric silsesquioxane polymer composites since the cost of production has decreased significantly and these molecules have been found to modify a number of important properties. The addition of tethered POSS has been linked to increases in the glass transition temperature as the added POSS slows the dynamics of the polymer chain to which it is attached [1-4]. Blends of acrylic polyhedral oligomeric silsesquioxane and polymethyl methacrylate show a clear decrease in the glass transition temperature [4]. POSS polystyrene copolymers have shown lower viscosities [5] than the homopolymer. Blends of copolymerized POSS poly(methyl methacrylate) with PMMA and PS homopolymers showed increased fracture toughness [6]. POSS may be incorporated into a polymer either by chemically tethering it to the polymer backbone or by blending the particles with the polymer matrix. POSS has been successfully copolymerized with polysiloxane[7-9], poly(methyl methacrylate)[10], polynorbornene[11], polystyrene[12], polyethylene[13], and polyurethane [14-16]. POSS has also been blended with amphiphilic poly(dimethylsiloxane) [17], epoxy [18], and poly(methyl methacrylate) [4, 19]. In this chapter, molecules of CpPOSS are blended at different concentrations into a matrix consisting of pentacontane ($C_{50}H_{102}$) chains. In this system, the polymer mobility is found to decrease, there is a slight increase in the glass transition temperature, and there is an enhancement of the elastic moduli.

4.1 Description of Simulations

Three system compositions were studied: a 5 weight percent CpPOSS/PE composite comprising 6 CpPOSS particles and 158 pentacontane ($C_{50}H_{102}$, denoted hereafter as C50) chains, a 15 weight percent CpPOSS/PE composite comprising 20 CpPOSS particles and 158 C50 chains, and a 25 weight percent CpPOSS/PE system comprising 60 CpPOSS particles and 167 C50 chains. As described in Chapter 3, the POSS particles and polymer were modeled using an explicit atom force field developed by Sun et al. [20-22].

CpPOSS/PE composites are created by first randomly placing CpPOSS particles within a representative volume element. The CpPOSS particles are given a random rotation and displacement within the cell. The new position of the particle is accepted or rejected based on a Monte Carlo acceptance criteria based on the energy of inserting the particle into the system. This prevents particles from overlapping in non-physical ways. If the particle insertion is rejected, then the particle is given a new displacement and rotation and insertion is attempted once again.

After all of the CpPOSS particles have been placed within the simulation cell, the polymer is added to the system. Specifically, pentacontane chains were introduced into the system by first randomly selecting a starting point for the chain and inserting additional monomers with fixed bond lengths, fixed bond angles, and random dihedral angles, with an acceptance criteria based on the energy of the inserted molecule. The systems were then equilibrated using a Metropolis Monte Carlo algorithm with single atom displacement moves applied to all atoms, and reptation moves and concerted rotation moves applied to polymer chains.

Each structure, Table 4-1, was then subjected to the following simulation schedule: i) 100 ps simulation at 500K, holding the number of atoms, volume, and temperature constant (NVT ensemble); ii) 5 ns simulation at 500K, holding the number of atoms, pressure, and temperature constant (NPT ensemble); iii) 2ns simulation during which the temperature was ramped from 500K to 300K in steps of 1×10^{-4} K every 1 fs; iv) 10 ns at 300K, holding the number of atoms, stress tensor and temperature constant (NσT ensemble). In each case, the set point pressure was atmospheric. The intent of this protocol was to observe the behavior of the composites at 500K and 300K, with the cooling segment allowing for an equilibrated structure to be constructed at 300K. The simulation segment (i) allows the atomic velocities to equilibrate before the simulation cell size is allowed to fluctuate. The system densities were 0.80(1) g/cm^3, 0.82(1) g/cm^3, 0.84(1) g/cm^3, and 0.87(1) g/cm^3 at 500K, 0.88(1) g/cm^3, 0.90(1) g/cm^3, 0.93(1) g/cm^3, and 0.96(1) g/cm^3 at 300K, 0.93(1) g/cm^3, 0.94(1) g/cm^3, 0.97(1) g/cm^3, 0.99(1) g/cm^3 at 200K for composites of 0 wt%, 5 wt%, 15 wt%, and 25 wt% respectively.

Molecular dynamics simulations were performed using the velocity Verlet algorithm [23] with an integration time step of 1 fs. The pressure within the simulation

cell was maintained at the target value by rescaling the volume of the cell using the approach of Berendsen et al. [24] with a barostat constant of 100 ps. The temperature was controlled using the Berendsen thermostat with a thermostat constant of 10 ps. The details of the algorithms used can be found in Chapter 2.

Table 4-1: Initial Structure Description.

Weight Percent POSS	Number of Chains	Number of Monomers Per Chain	Number of POSS particles	Generation Density [g/cm^3]	Generation Temperature [K]
5	158	50	6	0.55	500
15	158	50	20	0.55	500
25	143	50	60	0.55	500

4.2 Length Scales

The connections between physical properties and length scale can be significant in polymer systems. Namely the connections between filler particle size and radius of gyration have been shown to play a key role in the properties of polymer nanocomposites[25-32]. In the following sections, we will characterize several important length scales in the system: the average separation between particles, the radius of gyration of the polymer chain, and the filler particle size.

4.2.1 Average Particle Separation

The average particle separation is important for several reasons. If particles are separated by less than the radius of gyration of the polymer chain, then the conformational space of the polymer in the surrounding cavities will be affected throughout the composite by the presence of the particles. Second, comparing the average separation between particles to the distances traveled by particles during the simulations will indicate how much of the composite's phase space has been explored during the course of the simulations.

We quantify the average separation of particles in the system first by using the concentration of particles. Given the number of particles, N, within a certain volume, V, one can obtain the average separation between particles, $\bar{d}_{disp}$, by taking the cube root of the total volume divided by the number of particles in that volume:

$$\overline{d}_{disp} = \sqrt[3]{\frac{\langle V \rangle}{N}} . \tag{4.1}$$

Note that this equation assumes that the particles are well dispersed in the matrix.

In Section 4-7, we will show that this is not true for the 15 and 25 weight percent systems. The resulting average separation distances at 500K, 300K, and 200K for the POSS composites are given in Tables 4-2, 4-3, and 4-4 respectively. The next section will show that the polymer radius of gyration is approximately 1 nm. The diameter of the particle, from base of R-group to R-group is approximately 1.4 nm. At 25 weight percent, the average separation between particles is approaching the radius of gyration of the polymer and the diameter of the POSS particles themselves assuming that the particles are perfectly dispersed.

Table 4-2: Theoretical average separation between particles at 500K for various systems assuming perfect dispersion.

Weight Percent POSS	$\langle V \rangle$ [nm^3]	N_{POSS}	$\bar{d}_{disp}$ [Å]
5	235	6	34.0
15	255	20	23.3
25	296	60	17.0

Table 4-3: Theoretical average separation between particles at 300K for various systems assuming perfect dispersion.

Weight Percent POSS	$\langle V \rangle$ [nm^3]	N_{POSS}	$\bar{d}_{disp}$ [Å]
5	212	6	32.8
15	232	20	22.6
25	269	60	16.5

Table 4-4: Theoretical average separation between particles at 200K for various systems assuming perfect dispersion.

Weight Percent POSS	$\langle V \rangle$ [nm^3]	N_{POSS}	$\bar{d}_{disp}$ [Å]
5	204	6	32.4
15	221	20	22.3
25	254	60	16.2

However, this measure is not the only relevant length scale in the problem. The calculation of mean separation based on concentration, $\bar{d}_{disp}$, does not account for the mesoscopic structure that may develop. The distance between a given CpPOSS particle and its nearest neighbor is also relevant when studying aggregation phenomena and interpreting the aggregation data presented in later sections within this chapter. In a case with a heterogeneous distribution of particles, these two measures may give very different answers. What is termed here as the average distance to the nearest neighbor, $\bar{d}_{PNN}$, approaches 10 Angstroms for particles which are in crystal registry. The difference between $\bar{d}_{PNN}$ and 10 Angstroms is the distance over which a particle must travel in order to enter into crystal registry with its nearest neighbor.

The actual average nearest neighbor distance was evaluated by averaging the computed minimum distance between each particle and all of its neighbors as follows:

$$\overline{d_{PNN}} = \left\langle \frac{1}{N_{POSS}} \sum_{i=1}^{N_{POSS}} \min\left\{ \left(\vec{r}_i^{\,cm} - \vec{r}_j^{\,cm} \right)_{j=1..N_{POSS}, j\neq i} \right\} \right\rangle \tag{4.2}$$

where $\overline{d}_{PNN}$ is the average particle separation, N_{POSS} is the number of POSS particles, $\vec{r}_i^{\,cm}$ is the center of mass of POSS particle i, and the average is taken over the trajectory. Results for this calculation at 500K, 300K, and 200K are given in Table 4-5.

As the concentration increases, $\overline{d}_{PNN}$ decreases as one would expect. So we can see that for the concentrations of 15 and 25 weight percent, the particles need to travel only 2 to 3 Angstroms before they are in a position where crystal registry with their neighbor is possible. However at 5 weight percent the CpPOSS particle must travel approximately 10 Angstroms to reach its nearest neighboring particle. The values of $\overline{d}_{PNN}$ can be compared to the dispersed values, $\overline{d}_{disp}$. The lower values of $\overline{d}_{PNN}$ indicate that the particles are not perfectly dispersed on a simple cubic lattice. We will show later that the particles have aggregated to some degree and it is this aggregation that reduces the nearest neighbor distances between particles.

Table 4-5: Average minimum particle spacing at 300K and 500K computed from simulated systems.

Weight Percent POSS	$\overline{d}_{mps}$ [Angstroms] T = 300K	$\overline{d}_{mps}$ [Angstroms] T = 500K
5	20.0	20.5
15	12.9	13.5
25	10.3	12.0

4.3 Radius of Gyration

The radius of gyration is a measure of the size of the polymer chain. The radius of gyration, R_g, was calculated using the following formula:

$$R_g^2 = \frac{\sum_{i=1}^{N_{ca}} m_i \left\langle \left(\vec{r}_i - \vec{r}_{COM}^{chain} \right)^2 \right\rangle}{\sum_{i=1}^{N_{ca}} m_i} \tag{4.3}$$

where N_{ca} is the number of atoms in the chain, m_i is the mass of atom i, $\mathbf{r}_i$ is the position of atom i, and $\vec{r}_{COM}^{chain}$ is the position of the center of mass of the chain. The results can be found in Table 4-6. As shown in Section 4.2.1, the distance between particles is approaching the radius of gyration of the polymer chains. However, there is no change in the radius of gyration of the polymer with increasing CpPOSS content.

Table 4-6. Radius of gyration for polymer chains within the CpPOSS/PE composite.

Composition [weight % POSS]	R_g [Å] T = 200K	R_g [Å] T = 300K	R_g [Å] T = 500K
0	10.7(1)	10.9(2)	10.2(2)
5	11.4(1)	11.2(3)	10.2(3)
15	10.6(2)	10.8(2)	10.1(2)
25	10.7(2)	10.6(3)	10.2(2)

4.4 Diffusion

Understanding the effects of increasing CpPOSS concentration on mobility of both the polymer and of the particles is critical to understanding how CpPOSS acts to reinforce the matrix and alter the properties of the composite. These effects are determined by calculating the translational dynamics of the polymer and the translational and rotational dynamics of the CpPOSS particles. The translational dynamics were determined by measuring the mean squared displacement,

$$\left\langle \Delta r(t)^2 \right\rangle = \left\langle \frac{1}{N} \sum_{i=1}^{N} \left(\left| \vec{r}_i(t) - \vec{r}_i(0) \right| \right)^2 \right\rangle, \tag{4.4}$$

of atoms within the system and using this data to calculate a diffusion coefficient, D, for that set of atoms. The diffusion coefficient is obtained from the limiting behavior of the mean squared displacement using the familiar Einstein relation:

$$\lim_{t \to \infty} \frac{d\left\langle \Delta r(t)^2 \right\rangle}{dt} = 6D\,. \tag{4.5}$$

The mean squared displacement of the carbon atoms along the backbone of the polymer chain is given in Figure 4-1. The calculated diffusion coefficients in Table 4-7 reveal that the mobility of the polymer decreases with increasing CpPOSS concentration. The calculated diffusion coefficients of 5.0×10-6 cm^2 s^{-1} to 6.5×10-6 cm^2 s^{-1} at 500K compare well with the experimental value of 6.1×10-6 cm^2 s^{-1} reported by Pearson et al. [33] for C50 at 500K.

To measure the translational mobility of POSS particles, the mean squared displacement of the silicon atoms within the system was monitored, the results of which are given in Figure 4-2. The calculated diffusion coefficients in Table 4-8 reveal that the diffusion of the silicon atoms is approximately 1.5 times slower than that of the polymer. Table 4-8 also displays a drop in mobility at 25 weight percent CpPOSS. The diffusion coefficients could not be calculated accurately at 300K due to the slow motion of the CpPOSS particles at that temperature.

In these simulations the CpPOSS mobility is shown to be lower than that of the polymer. In many experimental systems, blending POSS into the polymer has a plasticizing effect. The plasticizing effect is probably due to the fact that in the experimental systems, the POSS molecule is more mobile than the polymer adding free volume and inducing increases in dynamics of the polymer. In the simulations, the CpPOSS acts to retard the motion of the polyethylene. As shown in Chapter 3, the rotational mobility of the ring groups for the POSS blended into the polymer is no greater than the dihedral angle rotation along the polymer backbone. The slower dynamics of the POSS leads to decreases in mobility for the matrix polymer.

Figure 4-1. Mean squared displacement (MSD) of carbon atoms in the polymer at 500K and 300K.

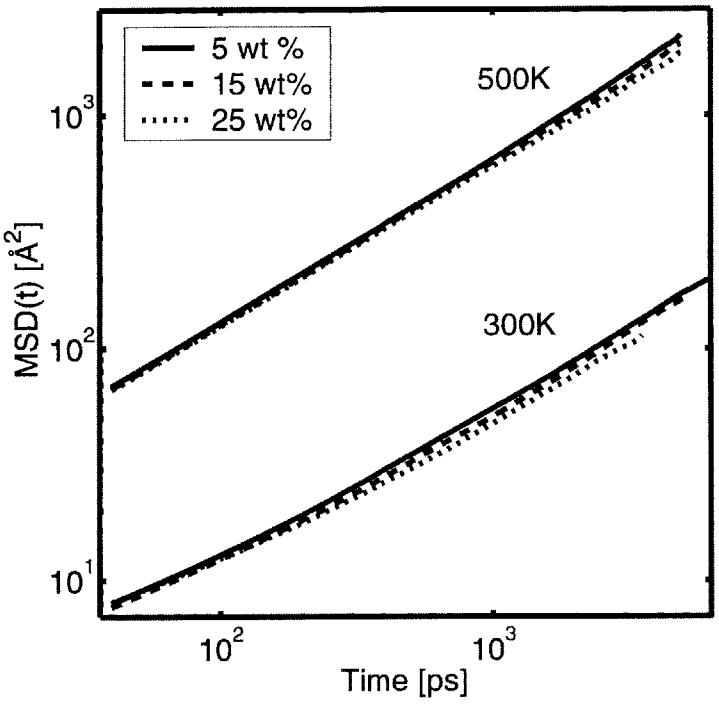

Figure 4-2. Mean squared displacement of Silicon atoms at 500K and 300K.

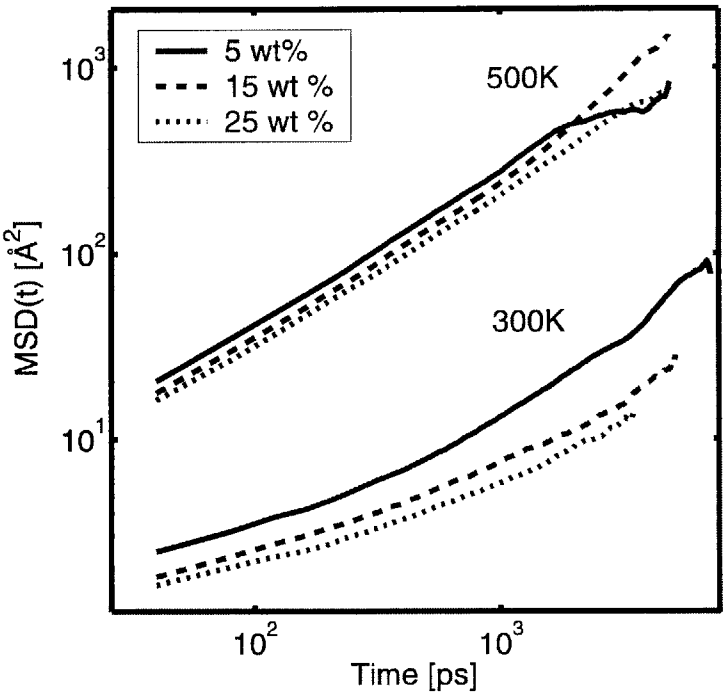

Table 4-7. Diffusion coefficients ($\times 10^6$ D [$cm^2\ s^{-1}$]) for polymer backbone atoms.

Composition [weight % POSS]	300K	500K
5	0.39	6.5
15	0.47	6.0
25	0.44	5.3

4.5 Rotational Diffusion

The rotational diffusion constants can be calculated from the long time behavior of the following function [34]:

$$D_{rot} = \lim_{t\to\infty} \frac{1}{4t} \left\langle \theta(t) - \theta(0) \right\rangle \tag{4.6}$$

where D_{rot} is the rotational diffusion constant, $\Delta\theta(t)$ is the angle of rotation of molecular reference frame, t is the time, and the average is taken over initial positions. The rotational diffusion constant, D_{rot}, can then be calculated from the slope of this function at long times. If we take $\theta(0) = 0$, i.e. we take the initial orientation as the reference frame, then we can relate D_{rot} to $\theta(t)$. By attaching a unit vector to the Si-O bond vector, $\hat{b}$, we can calculate a rotational diffusion constant by calculating the following equivalent function:

$$D_{rot} = \lim_{t\to\infty} \frac{1}{4t} \left\langle \hat{\mathbf{b}}(t) \bullet \hat{\mathbf{b}}(0) \right\rangle. \tag{4.7}$$

Therefore some information concerning the rotation of the CpPOSS particle can be obtained by using information from the bond autocorrelation function for the Si-O bond vector. One should keep in mind that this assumes that the Si-O bond rotates with the molecular reference frame. In this case, the relatively rigid silicon oxygen cage does rotate with the molecular reference frame as can be seen from molecular trajectories. The bond autocorrelation data for the composites can be found in Figure 4-3. A decaying exponential was fit to the data and used to obtain estimates of the rotational diffusion coefficients found in Table 4-8.

The decrease in the mobility of the POSS particles with increasing concentration, in particular as the concentration is increased from 15 wt% to 25 wt%, may be due to the

same attractive interactions between particles that leads to the aggregation mentioned earlier. At 5 wt%, these attractions appear to be sufficiently minor that the POSS particles may be deemed dilute and non-interacting. It is evident from this data that the CpPOSS acts to decrease the mobility of the polymer, which is consistent with the increases in T_g seen in the tethered POSS nanocomposites.

Figure 4-3. Bond autocorrelation function (BACF) for Si-O bonds at 500K for 5, 15, and 25 wt % CpPOSS/PE composite.

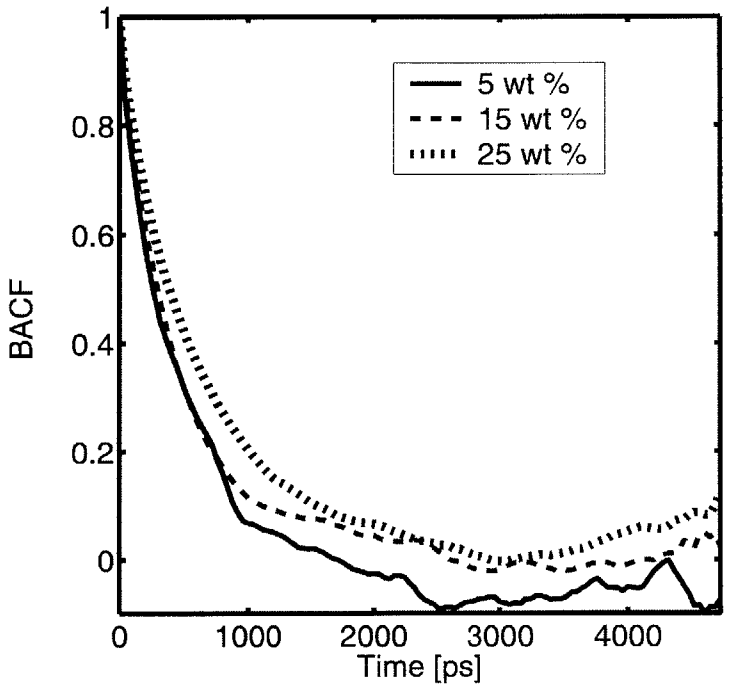

Table 4-8. Diffusion coefficients for silicon atoms at 500K.

Composition [weight % POSS]	D ($\times 10^6$ [cm^2 s^{-1}])	τ_{rot} [ps]
5	1.5	403
15	2.1	453
25	2.0	617

4.6 Aggregation

Crystallization of POSS particles has been seen experimentally and can play an important role in determining the properties of the final composite. Significant aggregation increases the size of each filler inclusion, and thereby decreases the surface area between particle and matrix in the composite. In order to study aggregation within these composites, the evolution of structure within the composite was monitored over the time scales accessible within these simulations. Even in simulations as short as 10 ns, changes in structure could be observed that indicate increased ordering of particles. Figure 4-4 and Figure 4-5 show snapshots of the 25 wt % system after completing stage (ii) (500K) and at the end of stage (iv) (300K), respectively. POSS particles are initially distributed randomly within the matrix at 500K, but during the 5ns NPT simulation at 500K, particle aggregation occurs, but without any internal structure developing. Upon cooling to 300K, the particles further aggregate within the polymer matrix, with the aggregates now developing an identifiable internal structure.

The aggregate structure was quantified by calculating the radial distribution function between the centers of mass of POSS particles and all silicon atoms within the system belonging to other POSS particles:

$$g_{P,A}(R) = \frac{V}{N_{Si} N_P} \left\langle \sum_{i=1}^{N_P} \sum_{j=1}^{N_{Si}} \delta(R - |\vec{r}_i^{\,P} - \vec{r}_j^{\,Si}|) \right\rangle \tag{4.8}$$

where $\vec{r}_i^{\,P}$ is the center of mass of POSS particle i, and $\vec{r}_j^{\,Si}$ is the position of silicon atom j, V is the volume of the simulation cell, N_{Si} is the number of silicon atoms in the system, and N_P is the number of POSS particles in the system. The only silicon atoms present within the system are located on the cage of the POSS particles. Therefore, this function shows on average how neighboring POSS particles are arranged around any given POSS particle.

Figure 4-7 displays the radial distribution function at 500K for the 15 and 25 wt% systems. The structure exhibits only a weak, fluid like, short range ordering of silicon atoms at this temperature. This indicates that at 500K, there is no discernable orientational organization of the CpPOSS particles within the systems. When the system is cooled to 300K, Figure 4-8 and 200K, Figure 4-9, the appearance of sharp peaks in the

radial distribution function indicates a specific organization of neighboring POSS particles. The peaks are present for distances less than 15 Å (which is the maximum distance between silicon atoms within nearest neighbor POSS particles). These peaks correspond to the peaks present in the radial distribution function for a CpPOSS crystal, as also shown in Figure 4-8. This suggests a clear ordering of neighboring POSS particles into the structural arrangement of the type found in the crystal phase. However, the simulation time scale (10 ns) precludes the formation of well-organized crystals. Instead, multiple POSS particles align with one another in an irregular network. The presence of crystalline domains within POSS/polymer composites has been observed extensively in experiments [15]. The ordered aggregates observed in these simulations are most likely the precursors to the crystallites observed experimentally. Unfortunately, the simulation time scales are too short to observe the assembly of well-formed crystallites. Data from the 5 wt% composite is not shown in Figure 4-8 because the CpPOSS particles, being more dilute in that system, did not exhibit aggregation on the time scale of the simulation.

Figure 4-4. Snapshot of initial configuration for a 25 weight percent CpPOSS/PE system.

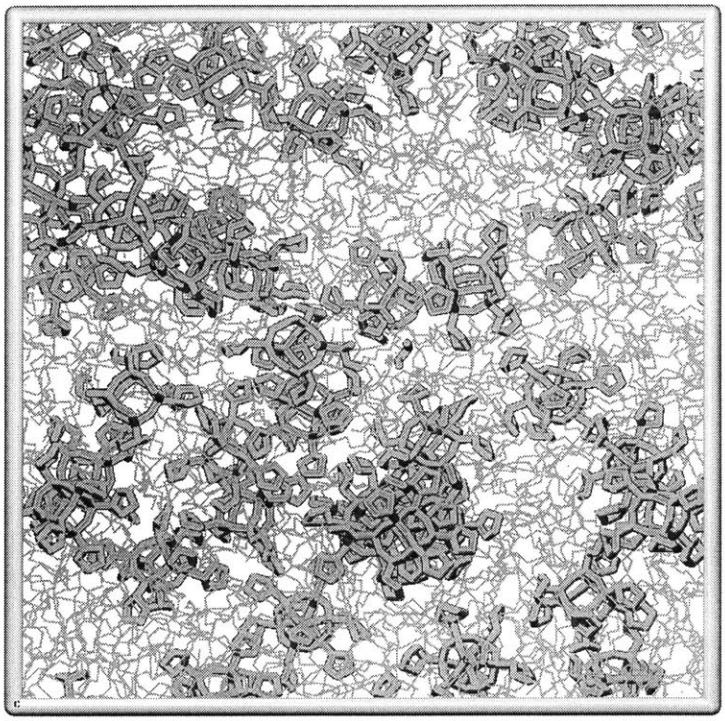

Figure 4-5. Snapshot of system after equilibration at 500K and cooling to 300K.

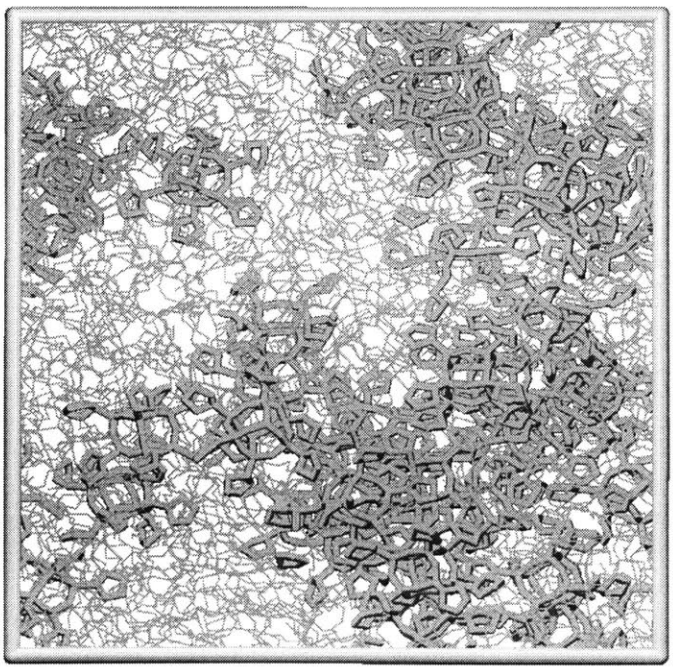

Figure 4-6: Snapshot of cluster within the 25 weight percent sample at 300K.

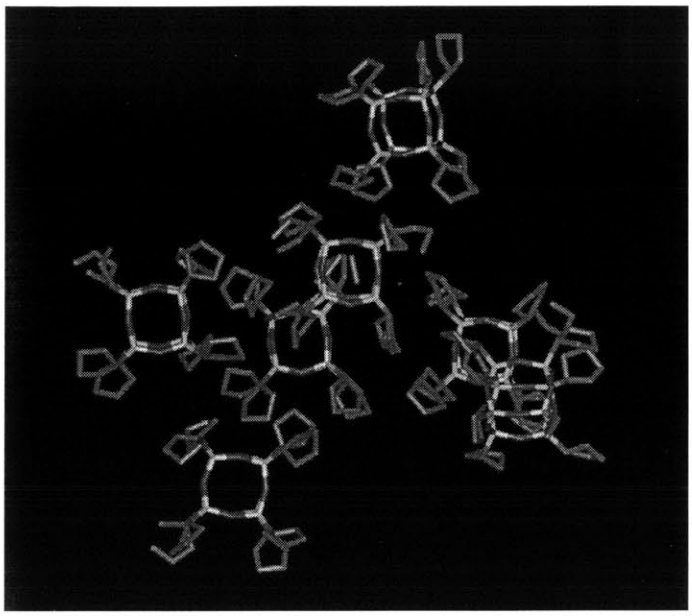

Figure 4-7. Radial distribution function, $g_{P\text{-}A}(R)$, of 15 and 25 wt % CpPOSS/PE composite at 500K. The inset illustrates the measurement of R from the center of the POSS particle.

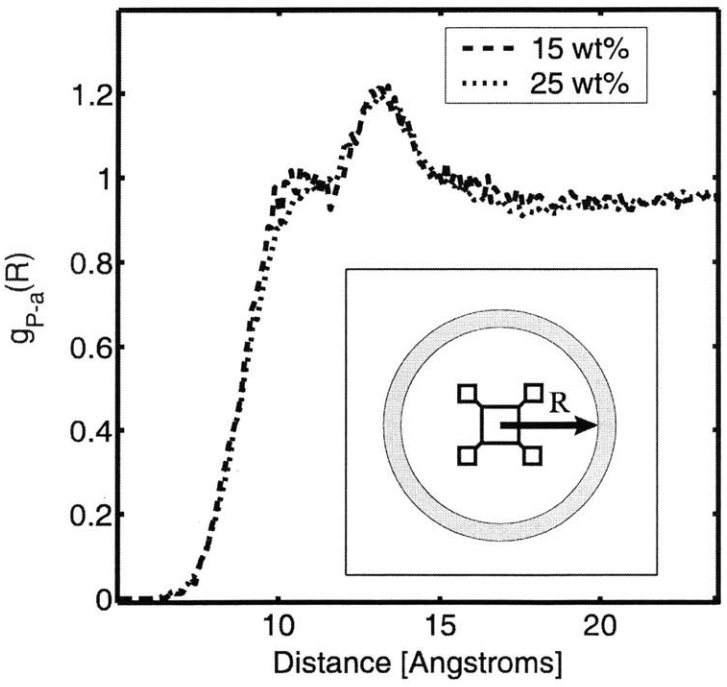

Figure 4-8. Radial distribution function, $g_{P-A}(R)$, of CpPOSS crystal, 15 wt% CpPOSS/PE composite, and 25 wt % CpPOSS/PE composite at 300K.

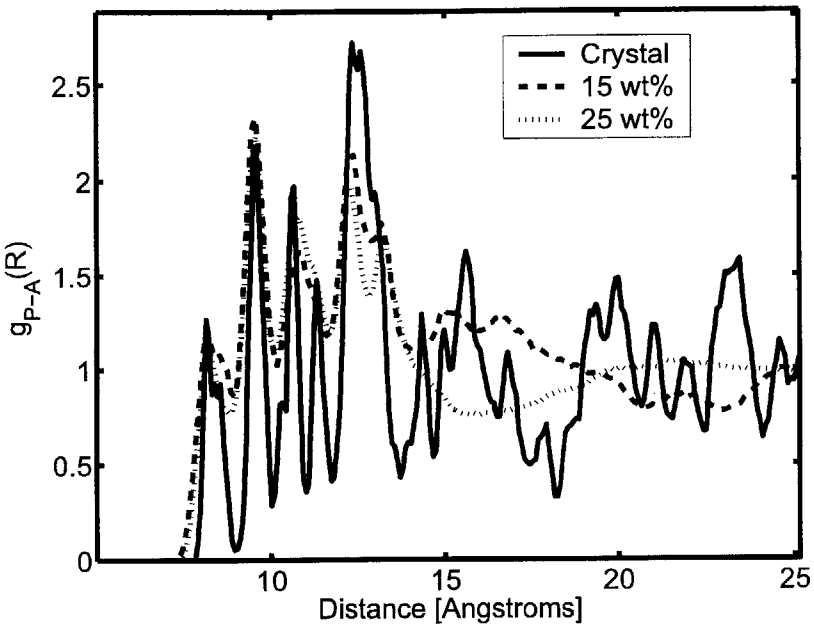

Figure 4-9. Radial distribution function, $g_{P-A}(R)$, of 15 wt% CpPOSS/PE composite, and 25 wt % CpPOSS/PE composite at 200K.

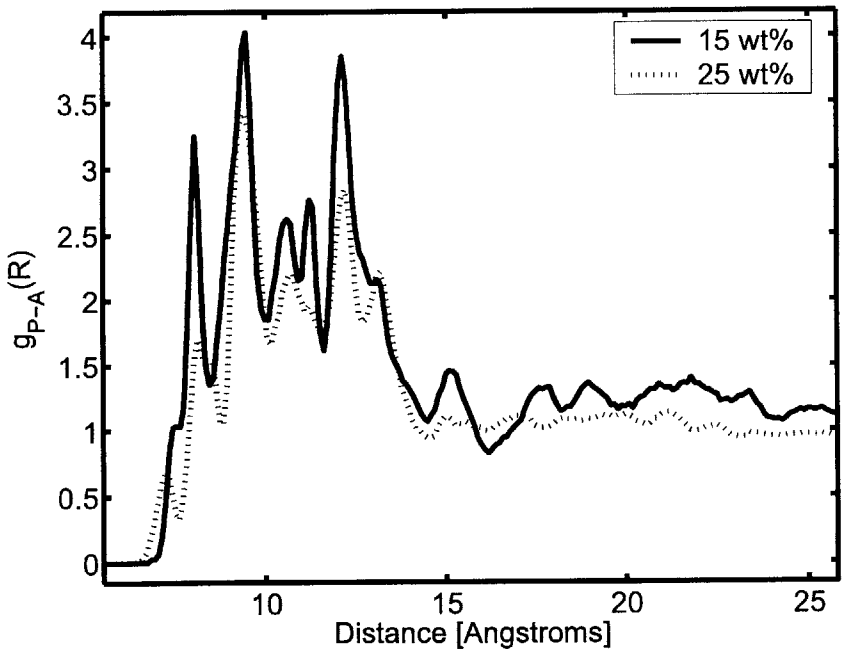

4.7 Cluster Analysis

Two methods were used to perform cluster analysis. The first was based solely on a proximity condition. Two particles were considered part of the same cluster if the separation distance between the centers of mass, $R_{P,P}$, was less than some critical value, $R_{P,P}^{Cluster}$.

The second method selects based on both a proximity condition and an alignment condition. The proximity condition is identical to that found in the first method. The alignment condition measures the angle of separation between the principal axis of each POSS particle. For each pair of molecules the principal axes, $\left\{\hat{\mathbf{e}}_1, \hat{\mathbf{e}}_2, \hat{\mathbf{e}}_3\right\}$, were calculated. For each possible pair of principal axes for these two molecules, an alignment parameter, $\phi_{ij,km}^{Cluster}$, is calculated as follows:

$$\phi_{ij,km}^{Cluster} = \min\left\{\left[\cos^{-1}\left(\mathbf{e}_i^m \cdot \mathbf{e}_j^k\right)\right]^2, \left[\pi - \cos^{-1}\left(\mathbf{e}_i^m \cdot \mathbf{e}_j^k\right)\right]^2\right\} \tag{4.9}$$

where i and j denote the principal axes being compared, m and k are the POSS particle numbers each ranging from 1 to N_{POSS}. The three minimum values of $\phi_{ij,km}^{Cluster}$, for k = 1,3 and m = 1,3, are taken for each pair of particles and the maximum of these three values, $\phi_{ij,\max}^{Cluster}$, is used to determine clustering. If the value of $\phi_{ij,\max}^{Cluster}$ is less than a critical value, $\phi_{critical}^{Cluster}$ then the two particles are considered to be part of the same aggregate. The value of $\phi_{critical}^{Cluster}$ varies between 0 and $\frac{1}{4}\pi^2$.

When analyzing the results of this analysis, it is important to determine the probability that two randomly placed molecules will pass the alignment condition. If we imagine having a single vector in 3d space, v_1, and we introduce a new randomly oriented vector, v_2, the probability that the angle between them will be θ, assuming we consider only the line vector and do not assign a direction along this line, is given by

$$\begin{aligned} p(\theta) &= \sin\theta, \qquad 0 \le \theta \le \frac{\pi}{2} \\ P(\theta) &= 1 - \cos\theta \end{aligned} \quad . \tag{4.10}$$

Therefore the probability that these two angles will have a score that is less than ϕ is given by

$$P(\phi) = 1 - \cos\sqrt{\phi}, \quad 0 \le \phi \le \left(\frac{\pi}{2}\right)^2. \tag{4.11}$$

There are three principal axes for each particle, therefore the probability that one axis on particle 1 will have a score less than ϕ when compared to an axis on particle 2 is three times equation (4.11). In order for the alignment condition to be satisfied, all three axes on particle 1 must have an axis on particle 2 which produces a score below ϕ. The joint probability that axes 1, 2, and 3 on particle 1 will each have a corresponding axis on particle 2 which gives a score below ϕ is then given by

$$P(\phi) = 9\left(1 - \cos\sqrt{\phi}\right)^2 \tag{4.12}$$

The number of particles within a given distance, r, from another particle can be approximated as

$$N(r) = \frac{4}{3}\pi r^3 \frac{N_{POSS}}{V} \tag{4.13}$$

Given the number of particles in the system within a distance r from any particle, N(r) the number of clusters of at least size 2 that will randomly form is given by

$$N_{C_2} = N_{POSS} N(r) P(\phi). \tag{4.14}$$

The number of clusters of at least size C_3 is given by

$$N_{C_3} = N_{C_2}\left[2N(r)P(\phi)\right]. \tag{4.15}$$

We can see from the expectation numbers calculated in Table 4-9, that there is a miniscule probability that any of the systems will register the presence of a cluster at any given time step. However this probability will grow linearly with simulated time.

The proximity and orientation method was used to calculate the number of clusters in each of the samples in Table 4-10 using a cutoff distance r = 12 Å and a θ = 10°. The clusters are identified by the number of molecules within a given cluster. For example, a C_2 cluster has 2 CpPOSS molecules within it and a C_{10} cluster has 10 CpPOSS molecules within it. This analysis reveals that 65 percent of the CpPOSS in the 15 weight percent CpPOSS/PE composite is part of a cluster. Similarly, 38 percent of the 25 weight percent CpPOSS/PE composite is clustered. The presence of these large

clusters occurring within a randomly distributed system are miniscule and their presences confirms the aggregation tendency seen within the radial distribution data in Section 4.7.

Table 4-9: Number of clusters formed, N_{Cn}, of size greater than or equal to n that in a system with a given the number of POSS particles and assuming all particles are randomly oriented.

Number of POSS Particles	Cluster type	Expectation Number
6	C_2 C_3	1.3×10^{-3} 7×10^{-7}
20	C_2 C_3	2.1×10^{-2} 4.6×10^{-5}
60	C_2 C_3	0.16 8×10^{-3}

Table 4-10. Number of clusters and cluster characterization in CpPOSS/PE composites.

Composition [wt% CpPOSS]	Number of Clusters of Given Type
5	0
15	3 C_2 clusters 1 C_3 cluster 1 C_4 cluster
25	5 C_2 clusters 1 C_3 cluster 1 C_{10} cluster

4.8 Potential of Mean Force

The importance of aggregation (and possibly crystallization) of these CpPOSS particles within the matrix on determining the properties of the composite is significant. Increases in aggregation lead to decreases in interfacial area. In order to understand fully the aggregation and crystallization of CpPOSS particles, it is necessary to conduct simulations on large numbers of CpPOSS particles over long simulated time periods in order to observe the assembly of well-formed crystals. Such simulations are not practical using atomistic level simulations. This practical limitation could be overcome using coarse grained approximations. In anticipation of this, we derive here an effective inter-particle potential of mean force, based on data taken from these atomistic simulations, which can be used for subsequent mesoscopic modeling.

We assume a mesoscopic model which treats CpPOSS particles as interacting spheres. Given a particular functional form, the interaction parameters for the potential f mean force between particles embedded in a polymer matrix at a specific temperature can be found by inverting the observed radial distribution function. The radial distribution function was calculated between the centers of mass of CpPOSS particles, $g_{P,P}$, as follows:

$$g_{P,P}(R) = \frac{V}{N_P^2}\left\langle \sum_{i=1}^{N_P}\sum_{j=1}^{N_P} \delta(R + |\vec{r}_i^{\,P} - \vec{r}_j^{\,P}|) \right\rangle . \tag{4.16}$$

Figure 4-10 shows $g_{P,P}$ for 15 and 25 weight percent CpPOSS composites. The potential of mean force, W(r), was then calculated by inversion of the Boltzman distribution:

$$W(R) = -kT \ln\left(g_{P,P}(R)\right) \tag{4.17}$$

where k is the Boltzmann constant, and T is the temperature in Kelvin. A single potential of mean force was calculated based on the average $g_{P,P}(r)$ for the 15 and 25 weight percent CpPOSS composites as shown in Figure 4-11. Strictly speaking, this potential is only valid at 500 K and does not capture 3-body correlations, which become progressively more important at higher concentrations. Note also that equation 4.17 follows directly from U(R) = -kTln(P(R)) since ρg(R)dR gives the probability of finding

a particle at a distance R given there is a particle at the origin where ρ is the number density. The number density and dR leads to a constant difference between W(R) and U(R).

Functions of the Lennard Jones 9-6 type and a 5th order polynomial were each fit to the data in Figure 4-11 using a non-linear least squares fit. The 12-6 potential was also tried, but with less satisfactory results. Of these, the 9-6 potential was found to yield the best fit. The functions and parameters are given in Table 4-11.

Table 4-11: Potential of mean force model equations and parameters.

Equation	Parameters
$W(x)=\begin{cases} ax^5+bx^4+cx^3+dx^2+ex^1+f & x\le 13.49 \\ 0 & x>13.49 \end{cases}$	a = -0.0168 kJ/mol/Å^5 b = 1.1818 kJ/mol/Å^4 c = -33.1535 kJ/mol/Å^3 d = 462.328 kJ/mol/Å^2 e = -320.27 kJ/mol/Å^1 f = 8810.1 kJ/mol
$W(x)=\varepsilon\left[2\left(\frac{\sigma}{x}\right)^9-3\left(\frac{\sigma}{x}\right)^6\right]$	σ = 1.605 Å ε = 11.78 kJ/mol

Figure 4-10. Radial distribution function, $g_{P\text{-}P(r)}$, for CpPOSS/PE systems at 500K.

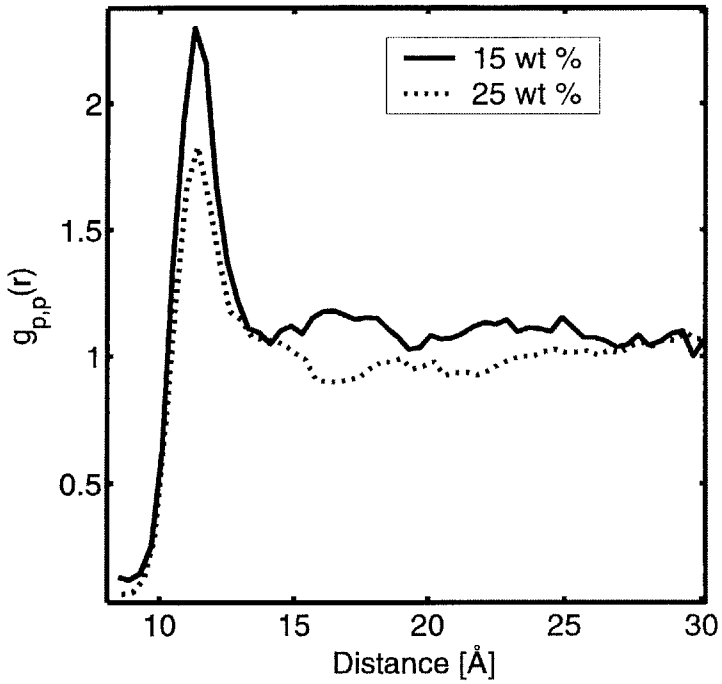

Figure 4-11. Potential of mean force for CpPOSS/PE systems at 500K.

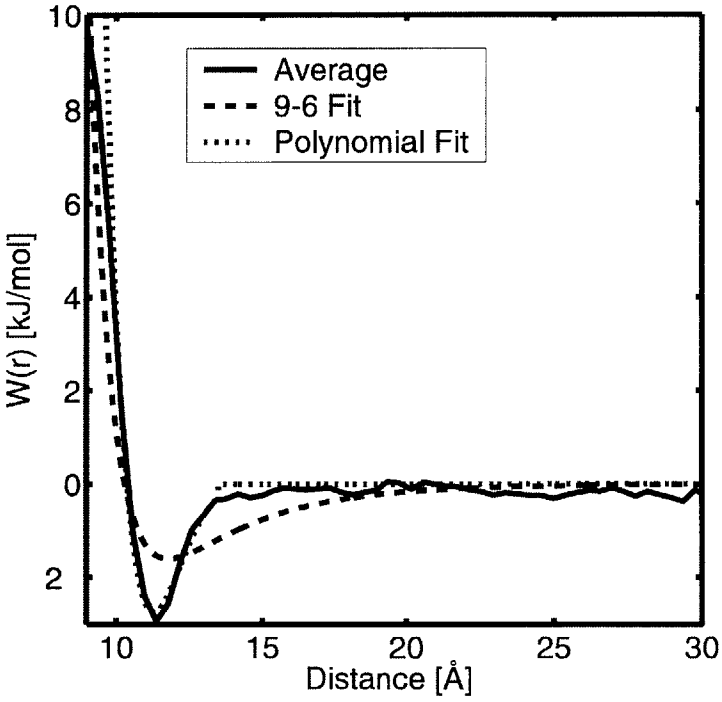

4.9 Potential of Mean Force with Angular Dependence

Although the potential of mean force as a function of the distance between CpPOSS molecule centers of mass, $R_{p,p}$, captures the attraction between CpPOSS particles, it lacks the details necessary to capture the orientation that develops within aggregates of CpPOSS. In order to capture the aggregation effects, one must introduce a variable that accounts for orientation between neighboring particles. We introduce a variable θ which is defined as follows:

$$\theta_{mis} = \sqrt{\phi_{ij,\max}^{Cluster}} \tag{4.18}$$

Theta is basically the largest angle between any two of the principal axes of the moment of inertia tensor for two CpPOSS molecules. The normalized probability distribution, $p(R_{P,P},\theta)$ is calculated as follows:

$$p\left(R_{P,P},\theta\right) = C\frac{\hat{p}\left(R_{P,P},\theta\right)}{\left[\left(R_{P,P}-\delta r\right)^3 - R_{P,P}^3\right]\sin\theta} \tag{4.19}$$

where $\hat{p}\left(R_{P,P},\theta\right)$ is a histogram of $R_{P,P}$ and θ values, δr is the histogram bin width. The terms in the denominator are used to normalize for the volume and angle dependence of the histograms. The constant C is chosen so that the integration of the probability distribution over the entire phase space is equal to one. The results at 300K for the 25 weight percent and 15 weight percent composites are shown in Figure 4-12 and Figure 4-13 respectively. The increased probability at distances, $R_{P,P}$, less than 12 Å indicates the attraction between CpPOSS centers. The increase probability for angles, θ, less than 10 degrees indicates that there is a preferred orientation when neighboring particles are close together.

Figure 4-12. CpPOSS center and orientation probability distribution function for the 25 weight percent sample at 300K.

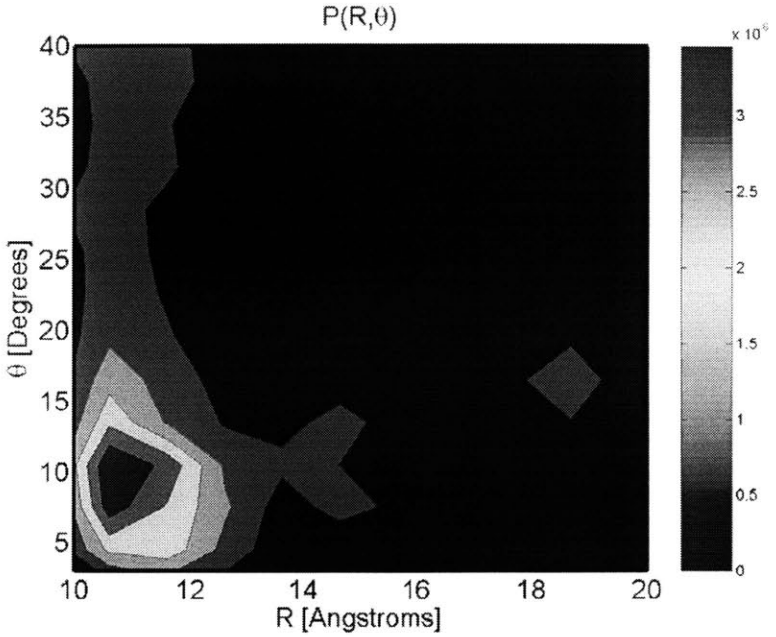

Figure 4-13: CpPOSS center and orientation probability distribution function for the 15 weight percent sample at 300K.

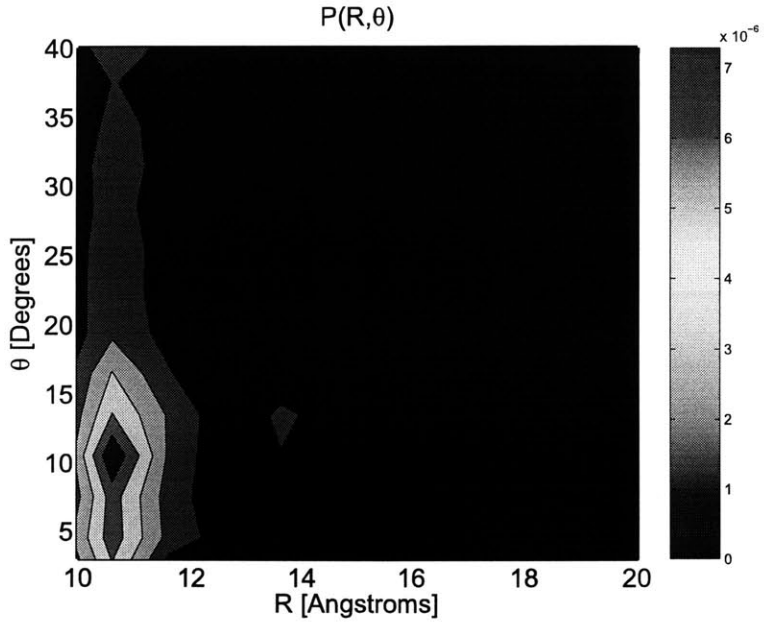

4.10 Glass Transition Temperature

The addition of tethered POSS has been linked to increases in the glass transition temperature as the added POSS slows the dynamics of the polymer chain [1-4]. Blending non-crystallizable POSS has been found to decrease the glass transition temperature [4]. Understanding the mechanisms for changes in T_g would help to engineer composites with a set of desired properties.

Each composition was cooled from 500K to 100K during a 10 ns molecular dynamics simulation in the NPT ensemble. The temperature was ramped down after each time step at a rate of 4×10^{-5} K/fs. The specific volume is plotted versus the temperature in Figure 4-14. The glass transition temperature can be estimated by determining where the curve changes slope. Two lines were fit to each composition. One line was fit using the specific volume data at the low temperatures of 100 K to 180 K and the other line was fit to the high temperature specific volume data from 330 K to 500K. The resulting glass transition temperatures can be found in Table 4-12.

From Table 4-12, we can see that there is an increase in the value of the glass transition temperature with loading above 15 wt% CpPOSS. This agrees with the overall decrease in the polymer and POSS mobility observed with increasing POSS content in these systems. The increase in glass transition temperature may be associated with either a strong interaction between polymer and POSS, or it can be explained via a confinement type effect. The less mobile POSS are spread through the polymer matrix and, assuming a perfect dispersion, are separated by distances on the order of the radius of gyration of the polymer at 15 and 25 weight percent. The increased confinement caused by their inertia could increase the T_g for the composite as a whole. It will be shown in Chapter 5 that the polymer interactions with the cyclopentyl ring groups are very similar to those between polymer chains.

Figure 4-14: Specific volume versus temperature for 0, 5, 15, and 25 weight percent CpPOSS/PE composites.

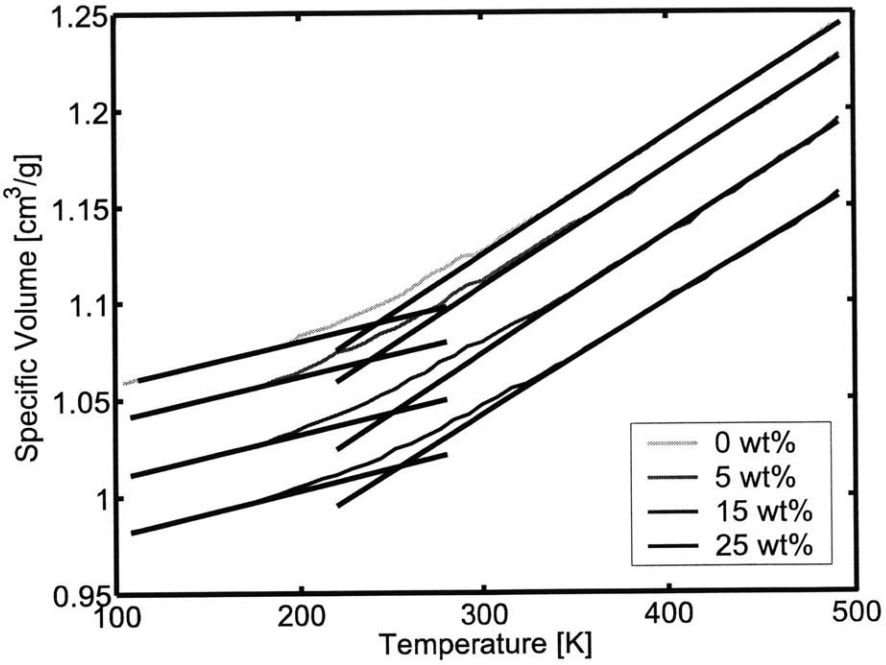

Table 4-12: Glass transition temperatures for 0, 5, 15, and 25 weight percent CpPOSS/PE composites.

Composition [weight %]	T_g [K]
0	242(6)
5	238(8)
15	250(5)
25	254(8)

4.11 Estimates of Effective Modulus for a Composite

Ultimately, one would like to determine the mechanical properties of a composite from the mechanical properties of the constituent components. In a composite with large filler particles, this requires knowledge of the properties of the matrix, the filler, and the bonding conditions at the boundary between the two. In this section, the Mori-Tanaka models will be presented which describe composite behavior based on the properties of the constituent materials. Note that as the size of the filler decreases to molecular dimensions, the thickness and properties of the interface between the filler and the matrix play an increasing role which is not accounted for in this model.

In the Mori-Tanaka method [35], the composite is treated as if each of the inclusions is placed within an infinite matrix which is subjected to the average strain field in the far field. These inclusions are assumed to be perfectly bonded to the matrix. The effective stiffness of the composite, $C_{effective}$, is given by:

$$C_{effective} = C_m \left[I + \left(v_f L_f \right) \left(I + v_f \left(S - I \right) L_f \right)^{-1} \right]^{-1} \tag{4.20}$$

where C_m is the stiffness tensor of the matrix material, v_f is the volume fraction of filler, S is the Eshelby tensor, and I is the fourth rank identity tensor. L_f is the localization tensor defined by:

$$L_f = -\left[\left(C_f - C_m \right) S + C_m \right]^{-1} \left(C_f - C_m \right) \tag{4.21}$$

where C_f is the stiffness tensor of the filler material.

When the model is applied to a matrix with non-interacting spherical inclusions distributed in a matrix, the equations reduce to the following:

$$
\begin{aligned}
K_{eff} &= K_m + \frac{v_f K_m (K_f - K_m)}{K_m + \alpha_m (1 - v_f)(K_f - K_m)} \\
\alpha_m &= \frac{3K_m}{3K_m + 4\mu_m} \\
\mu_{eff} &= \mu_m + \frac{v_f \mu_m (\mu_f - \mu_m)}{\mu_m + \beta_m (1 - v_f)(\mu_f - \mu_m)} \\
\beta_m &= \frac{6(K_m + 2\mu_m)}{5(3K_m + 4\mu_m)} \\
E_{eff} &= \frac{9K_{eff}\mu_{eff}}{3K_{eff} + \mu_{eff}}
\end{aligned}
\tag{4.22}
$$

where v_f is the volume fraction of filler, K_{eff}, K_f, and K_m are the effective bulk modulus for the composite, filler, and matrix, respectively; and μ_{eff}, μ_f, and μ_m are the effective shear modulus of the composite, filler and matrix, respectively and E_{eff} is the effective Young's modulus of the composite.

One can see in Figure 4-15 that as the ratio of filler modulus to matrix modulus increases, the effective modulus of the composite also increases. The Guth Gold model has a phenomenological term for interacting particles and deviates from the Mori-Tanaka effective properties as the volume fraction increases.

Figure 4-15: Effective composite modulus versus volume fraction for several ratios of filler modulus to matrix modulus.

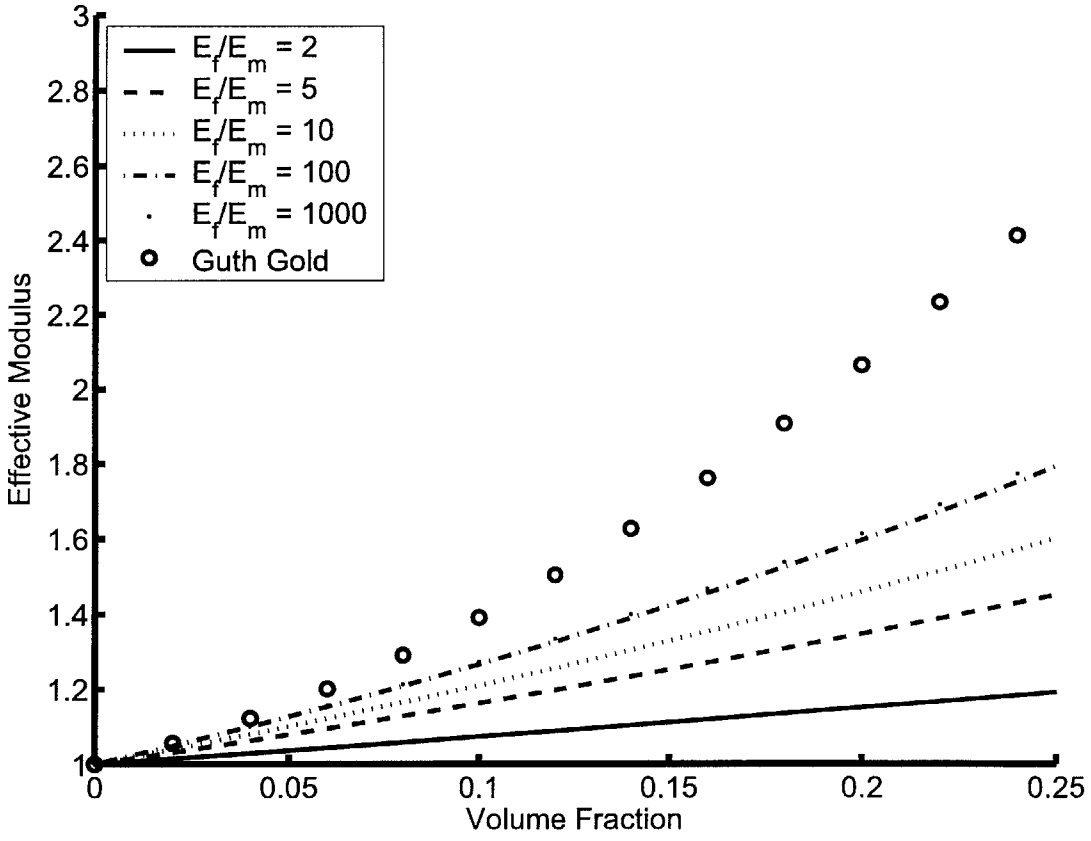

4.12 Elastic Moduli

The elastic moduli may be determined using direct methods. Assuming that we have captured a large enough representative volume element, the elastic behavior of the polymer nanocomposite is expected to be isotropic. As described in Chapter 3, this allows for only two independent elastic constants. Using this information, we can obtain the elastic moduli and the Poisson's ratio of the composite from a single uniaxial tension simulation. Simulations were run using configurations extracted from the glass transition temperature calculations at 200K. These equilibrated structures were then deformed using constant true strain deformation rates of 1×10^9 per second along the x axis while σ_{yy} and σ_{zz} are maintained at atmospheric pressure using the Berendsen barostat described in Chapter 2. Snapshots of the 15 weight percent CpPOSS/PE composite during deformation are shown in Figure 4-16. One can see from Figure 4-16 a and b that during deformation at these low temperatures there is little change in the positions of the CpPOSS cages. The stress strain data for these simulations is shown in Figure 4-17. The resulting elastic moduli are shown in Table 4-13. One notices that there is an increasing modulus with increasing CpPOSS content. As shown in Chapter 3, the CpPOSS crystal is stiffer than the polymer. However, the POSS in these composites is initially dispersed. In Section 4.7, we will show that aggregates do form to a limited degree but they occur between small groups of POSS and do not form neat crystalline domains within the polymer matrix. Using the moduli obtained from these simulations, we can attempt to estimate the "effective mechanical properties" of the POSS molecules. By this, we mean a pair of parameters, volume and moduli which describe the influence of the addition of CpPOSS in the polyethylene matrix according to continuum theories of mechanics of particle-filled composites.

The representative volume elements used in this study include between 6 and 60 POSS particles. This raises the possibility that due to the small size of the cell, there may be an anisotropic response due to the arrangement of the POSS within the cell. In order to test for this, the 25 weight percent structure was deformed along the x, y and z axis at the same rates as described above. The resulting elastic moduli were 1.81(8) GPa, 1.74(5) GPa, and 1.77(6) GPa along the x, y, and z axis respectively. Since the 25 weight percent

sample is expected to be the most anisotropic due to the structure of the POSS within the cell, the relative insensitivity of the modulus along these three directions indicates that the representative volume is large enough to capture an isotropic response.

Table 4-13 Elastic Moduli of CpPOSS/PE composite at 200K.

Composition [weight % POSS]	Elastic Moduli [GPa]	Normalize Modulus E/E_{matrix}	Poisson Ratio ν
0	1.55(8)	1	0.38
5	1.60(9)	1.03	0.39
15	1.67(7)	1.08	0.38
25	1.81(8)	1.17	0.35

Figure 4-16: a) Undeformed 15 weight percent CpPOSS/PE composite. b) 15 weight percent CpPOSS/PE composite deformed to 10 % true strain.

a)

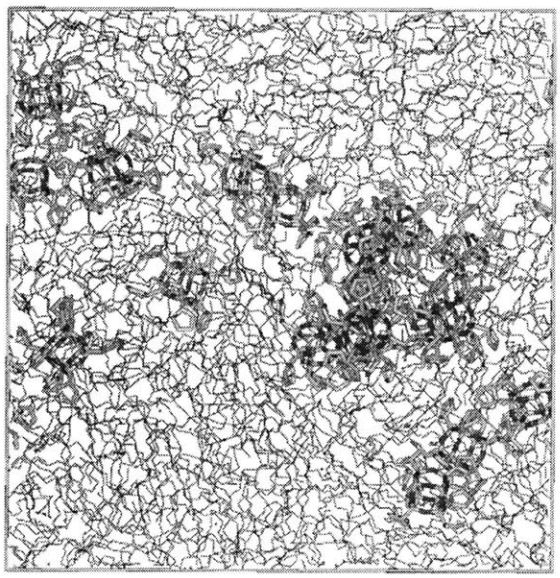

b)

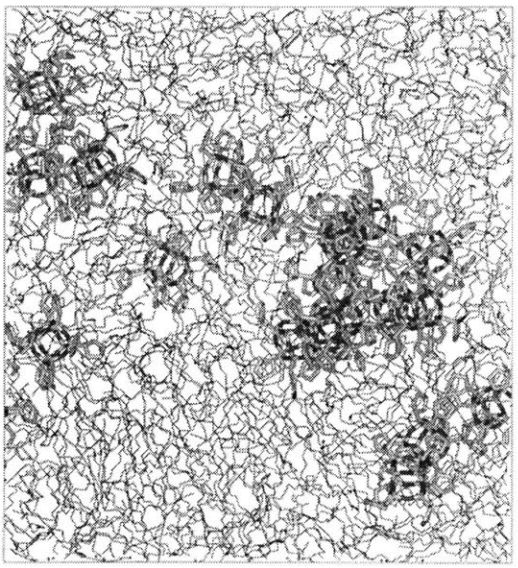

Figure 4-17: Axial stress versus strain for 0, 5, 15, 25 weight percent CpPOSS/PE composites. Each curve is shifted up by 50 MPa for clarity.

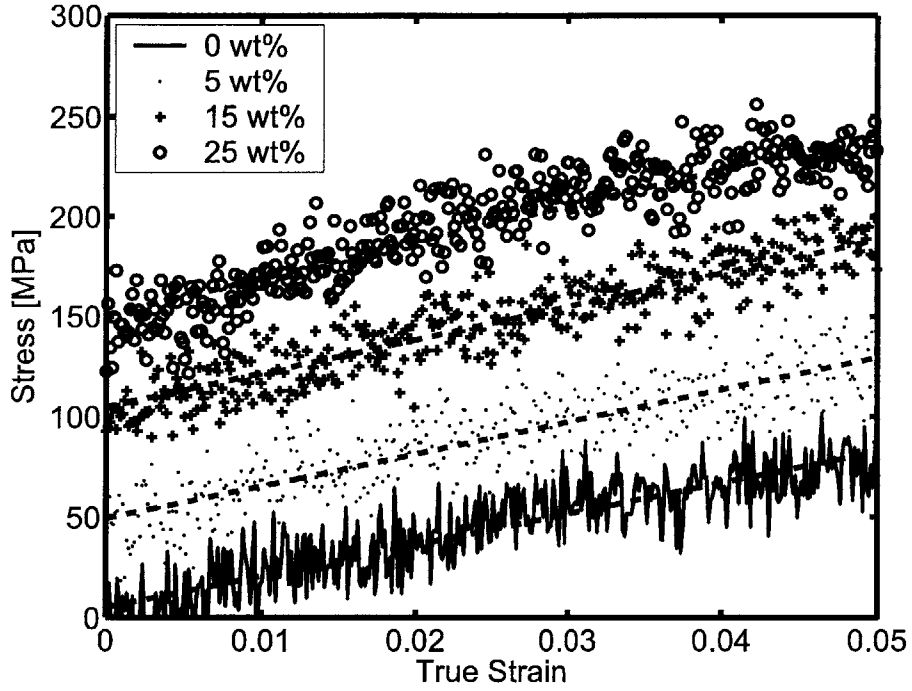

Figure 4-18: Stress components σ_{yy} and σ_{zz} versus strain for 5 weight percent CpPOSS/PE composite.

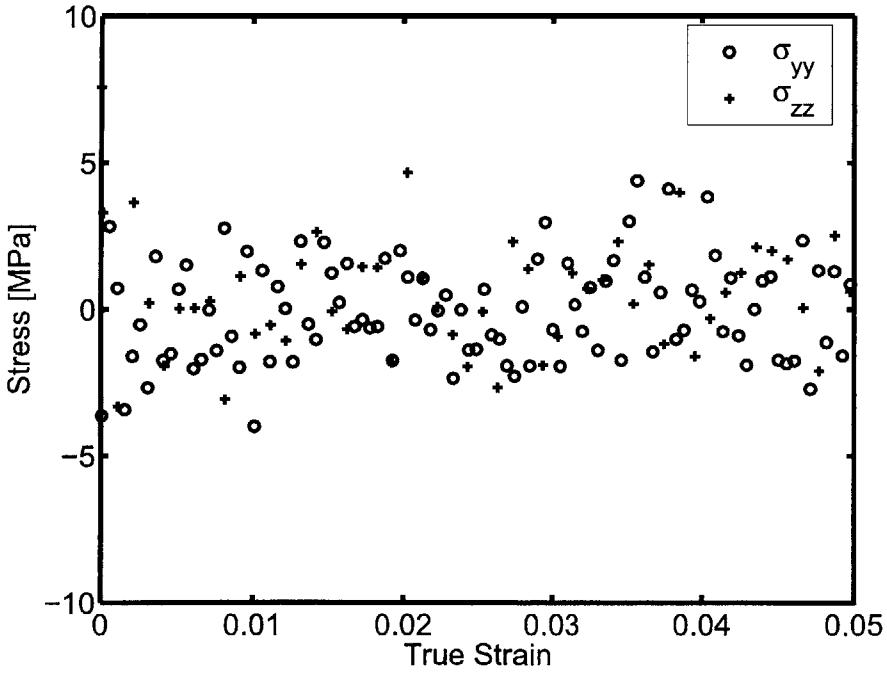

4.12.1 Guth Gold Model

Here, the effective mechanical size of the POSS particle will be estimated by fitting a micromechanical model to the calculated elastic moduli. In this case, we apply the Guth-Gold model[36] which has the following form:

$$E_{effective} = E_{matrix}\left(1+2.5v_f+14.1v_f^2\right) \tag{4.23}$$

where v_f is the volume fraction of filler, E_{matrix} is the modulus of the matrix material, and $E_{effective}$ is the effective modulus of the composite. The Guth-Gold model assumes that the filler particles are rigid spherical inclusions within the matrix material and that the inclusions are perfectly bonded to the matrix. The quadratic term accounts for interactions between particles with increasing volume fraction.

In order to apply this equation to the composite CpPOSS/PE systems, one must determine the volume fraction of the CpPOSS particles. In the case of a large filler particle with a well defined density, one can use the following conversion formula:

$$v_f = \frac{w_f}{w_f + (1-w_f)\dfrac{\rho_f}{\rho_m}} \tag{4.24}$$

where w_f is the weight fraction of the filler, ρ_f is the density of the filler, and ρ_m is the density of the matrix material. However, a single CpPOSS molecule does not have a well defined density which therefore precludes the use of this conversion. A more detailed explanation of this is given in Chapter 5 Section 5-1. Instead, we use the detailed knowledge that we have about the system, such as the number of CpPOSS molecules in the system, to directly compute the volume fraction of the filler. We assume that each particle is spherical and relate the volume fraction to the particle dimensions using the following equation:

$$v_f = \frac{\frac{4}{3}\pi R_P^3 N_P}{V} \tag{4.25}$$

where R_P is the effective radius of the CpPOSS molecule, N_P is the number of CpPOSS molecules, and V is the total volume of the system. Given that N_P and V are known, we can recast the Guth-Gold equation, which gives effective composite modulus as a function of volume fraction of filler, into an equation relating the effective modulus to the effective radius of the CpPOSS particle as follows:

$$E_{effective} = E_{matrix}\left(1+\frac{10\pi}{3}\frac{N_P}{V}\left[R_P^3\right]+25.0\pi\frac{N_P^2}{V^2}\left[R_P^6\right]\right). \quad (4.26)$$

This equation was then fit to the data in Table 4-13 using the least squares method to give the effective radius of the CpPOSS particles in our simulations. The effective radius is found to be 4.45 Å. This indicates that the effective mechanical radius of the POSS is approximately the radius of the inner silicon-oxygen cage which is 4.62 Å including the van der Waals radius. The resulting fit can be found in Figure 4-19. The CH_2 groups on the organic cyclopentyl pendant groups interact with the polyethylene CH_2 groups with the same interaction energies as the CH_2 groups in the polyethylene interact with themselves. Because of this, the flexible nature of the organic groups, and the fact that their relaxation times are similar to those of the dihedral angles within the polymer backbone, the organic groups do not contribute to the stiffening of the composite. Instead, only the rigid silicon-oxygen cage contributes. However, this indicates that the interactions between the POSS and polymer lead to a well bonded interface which is an assumption in all of the micromechanical models employed in this thesis.

Figure 4-19: Effective modulus versus CpPOSS content and Guth-Gold model fit.

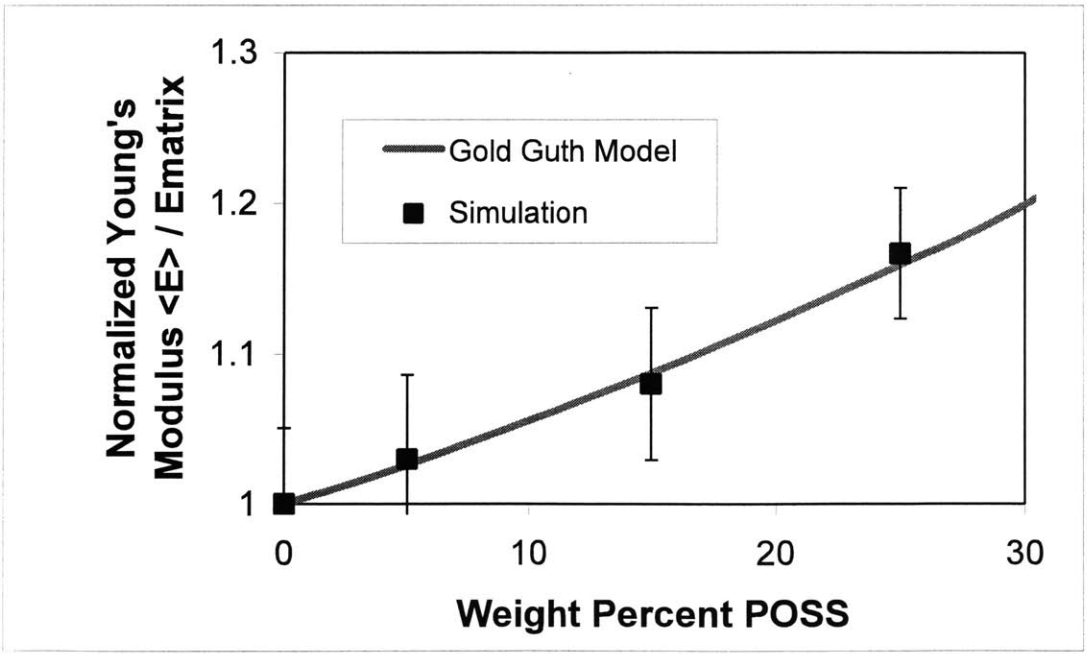

4.12.2 Mori-Tanaka Model

In Section 4.6.1, we fit the Guth-Gold model to the calculated elastic moduli as a function of weight percent. The Guth-Gold model assumes that the modulus of the filler is infinite and provides a prediction for the composite modulus as a function of matrix modulus and filler volume fraction. We know from Chapter 3 that the modulus of the CpPOSS crystal is on the order of 10 times stiffer than the polyethylene matrix. Given that the POSS particles begin to crystallize into aggregates with increasing filler volume fraction, the assumption of a rigid filler may not be valid for volume fractions greater than 15 wt %. Therefore, a model which accounts for both the volume fraction and elastic modulus of the filler particle is needed.

Here we present the Mori-Tanaka model [35] which gives an estimate of the effective modulus as a function of volume fraction and material properties as follows:

$$
\begin{aligned}
K_{eff} &= K_m + \frac{v_f K_m (K_f - K_m)}{K_m + \alpha_m (1 - v_f)(K_f - K_m)} \\
\alpha_m &= \frac{3K_m}{3K_m + 4\mu_m} \\
\mu_{eff} &= \mu_m + \frac{v_f \mu_m (\mu_f - \mu_m)}{\mu_m + \beta_m (1 - v_f)(\mu_f - \mu_m)} \\
\beta_m &= \frac{6(K_m + 2\mu_m)}{5(3K_m + 4\mu_m)}
\end{aligned}
\tag{4.27}
$$

where K_{eff}, K_f, and K_m are the effective bulk modulus for the composite, filler, and matrix, respectively; and μ_{eff}, μ_f, and μ_m are the effective shear modulus of the composite, filler and matrix, respectively. Note that the Mori-Tanaka model assumes perfect bonding between matrix and filler.

We will apply this model to the CpPOSS/PE composite system in several different ways. First, we will assume that we have a crystallite embedded within the polyethylene matrix and use the moduli calculated in Chapter 3 for the perfect crystal to predict the effective modulus as a function of weight percent filler. Second, we will use

the Mori-Tanaka model to find the set of parameters, volume fraction and moduli, which fit the calculated composite moduli.

We use the estimates of elastic moduli for the crystal which were determined in Chapter 3 for material properties of the filler. By using these properties, we are assuming that there are crystallites embedded within the polyethylene matrix. Since the density of the crystallites is well defined, one can use the common conversion formula from Equation 4.22 to estimate the volume fraction from the weight fraction. The ambiguity in assigning a volume to a single molecule decreases as the crystallite grows larger. The uncertainty in volume can be thought of as an uncertainty in where the surface of the molecule lies. As the enclosed volume increases, the uncertainty in the surface becomes less significant. This is discussed in more detail in Chapter 5. Figure 4-19 shows the effective modulus as a function of CpPOSS weight percent using the Mori-Tanaka fit combined with the weight fraction to volume fraction conversion given in Equation 4.21.

Although there is some ambiguity, knowledge of the atomic structure does give us some bounding values for the size of the particle. By using this information we can obtain bounds on the set of effective modulus/effective particle radius parameters which represent the mechanical behavior of the system and reflect the physical reality. The centers of silicon atoms within the CpPOSS cage are separated by 3.16 Å along any edge of the cube. The volume of the CpPOSS cage, calculated using the centers of the silicon atoms to define the cage, is found to be 31.56 $Å^3$. If we account for the van der Waals radius of the silicon, 4.29 Å, at the outer edges of the cube, the enclosed volume is 413.5 $Å^3$ and the effective particle radius is 4.62 Å. This defines the largest possible size of the POSS cube. The LJ potential for the silicon atoms has its minimum at the van der Waals radius so a neighboring atom may prefer to sit at this distance from the silicon. The LJ potential has a value of zero at 3.74 Å. This can be used as a hard sphere radius since an atom would have to have significant amounts of energy to approach closer than this distance. Using this hard sphere radius, the effective size of the POSS cage is found to be 4.28 Å. These two cases serve as bounds on the physical size of the cage and illustrate that there is significant ambiguity in the size of the POSS molecule. For comparison, the effective particle size of the crystalline phase of CpPOSS can be found. For the crystal, the total volume of the unit cell is well defined and can be used to unambiguously define

the effective particle size. Using the total volume of crystalline CpPOSS, 1268 $Å^3$, the effective particle size within the crystal is 6.71 Å.

Figure 4-20 illustrates the conversion from weight percent to volume fraction for the case of small crystalline POSS domains within a composite, dispersed particles which have the size of the hards sphere radius of the cage, and dispersed particles which have the size of the van der Waals radius of the cage. We can see that the additional volume enclosed between CpPOSS particles in the crystal leads to a higher volume fraction for a given weight percent of POSS.

We can also combine these estimates of particle size with estimates of particle modulus. The modulus can be approximated by finding the force required to stretch the POSS cage. This is done by applying forces to the silicon atoms in the system and measuring their displacements. The calculation of modulus requires an estimate of the normal area which leads to different moduli with different assumptions about the size of the cage. The cage has a modulus of 380 GPa assuming the HS particle and approximately 100 GPa for the VW particle. Figure 4-21 illustrates the predicated modulus for a composite made of crystalline CpPOSS aggregates, dispersed HS particles and dispersed VW particles. We can see that the simulated data falls between the HS and VW particle predictions.

Figure 4-20: Conversion from weight fraction to volume fraction assuming a) particles are small CpPOSS crystallites, b) particles are dispersed CpPOSS with effective radius equal to their center to center distance, HS, and c) particles are dispersed CpPOSS with effective radius encompassing the van der Waals radius of the cage, VW.

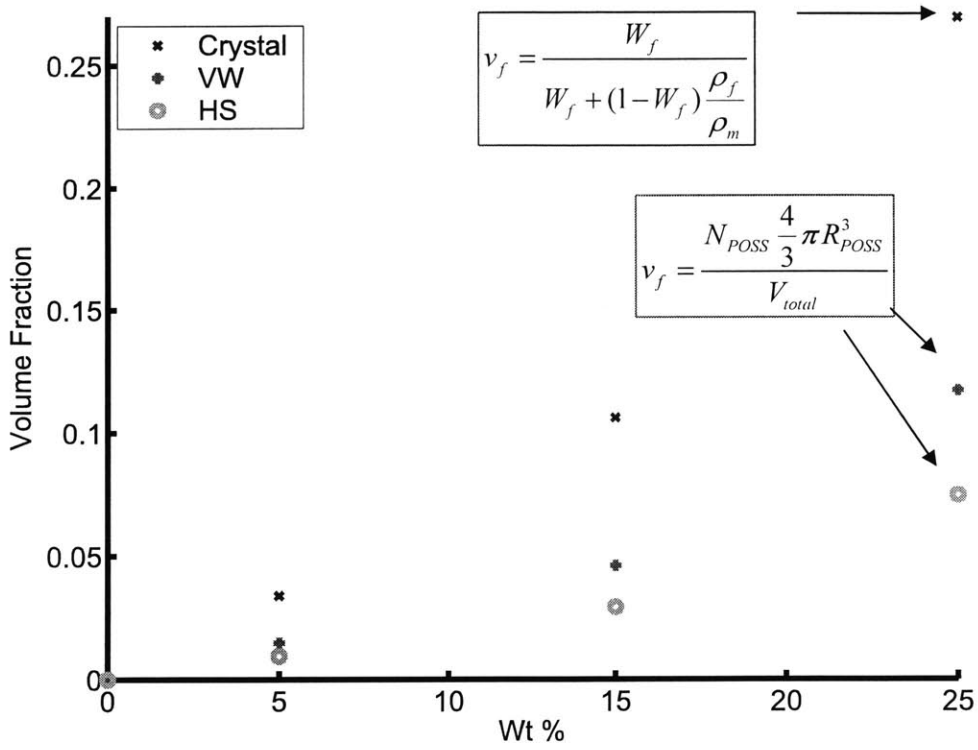

Figure 4-21: Effective modulus versus CpPOSS content assuming a) particles are small CpPOSS crystallites, b) particles are dispersed CpPOSS with effective radius equal to their center to center distance, HS, and c) particles are dispersed CpPOSS with effective radius encompassing the van der Waals radius of the cage, VW.

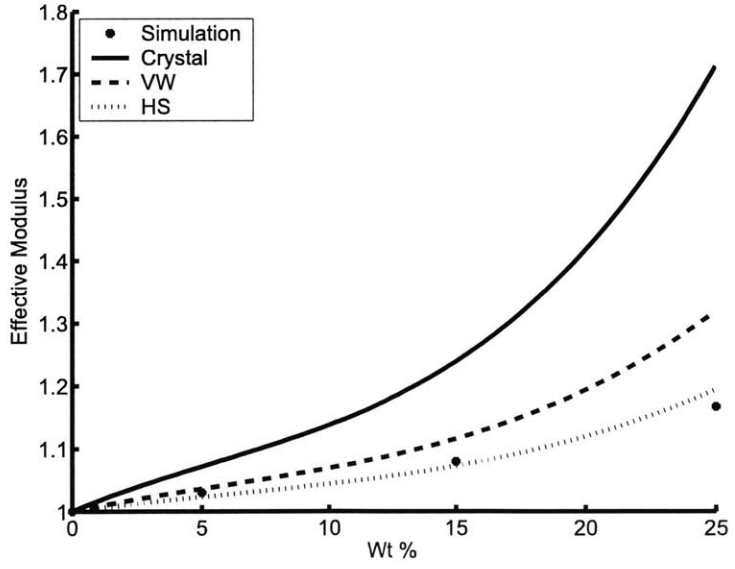

We can see in Figure 4-21, that the Mori-Tanaka formula does not fit the calculated data using the material properties for the crystallite and for the polymer. There are several possible explanations. The effective modulus of the single isolated CpPOSS molecule could be different than that of the crystalline CpPOSS due to the different interactions between the CpPOSS molecule and the PE versus interactions between CpPOSS and other CpPOSS molecules. We have shown that the CpPOSS exhibits some aggregation at higher weight fractions, but that these aggregates are not neat crystalline domains. Also, the conversion between weight percent and volume fraction is ambiguously defined and depending on this definition, the effect of the filler is either enhanced or diminished. In this case, the simulations are not consistent with the picture of a conventional composite of large POSS crystallites embedded within a PE matrix.

Since both the moduli and volume fraction have some ambiguity, we have used the simulated data to extract a set of parameters, effective radius, and effective modulus, which when taken together give a good fit to the simulated composite elastic moduli, Figure 4-22. These parameters can be found in Table 4-14. Figure 4-22 illustrates how the effective particle radius varies as a function for CpPOSS modulus. The following equation was fit to the data in Figure 4-22:

$$R_{effective} = \frac{a}{E_{CpPOSS}} + b \tag{4.28}$$

where $R_{effective}$ is the effective particle radius, E_{CpPOSS} is the effective CpPOSS modulus, and a and b are the fit parameters. The best fit results from a = 4.70(8) GPa Å and b = 4.29(1) Å. From this fit, we see that the limiting value as the modulus of the filler approaches infinity is 4.29 Å.

Table 4-14: Effective radius and modulus pairs which when used together in the Mori-Tanaka formula give a good fit to the simulated elastic moduli for the CpPOSS/PE composite.

Set	Effective Radius [Å]	Effective Modulus [GPa]
1	4.60	15
2	4.47	25
3	4.42	35
4	4.39	45

Figure 4-22: Fit of Mori-Tanaka model to the simulated elastic moduli for the CpPOSS/PE composites.

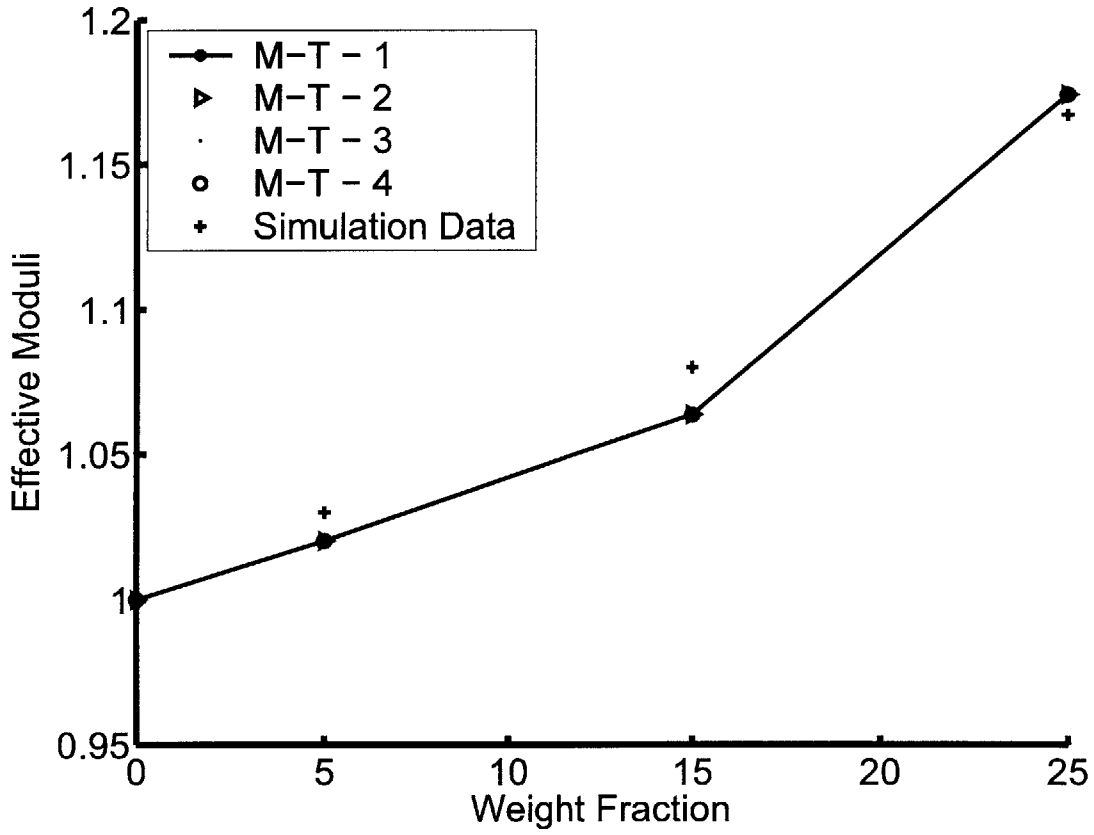

Figure 4-23: Family of Mori-Tanaka parameters, CpPOSS modulus and particle radius, which fit the simulated elastic moduli for the CpPOSS/PE composite. The dashed lines show the upper and lower bounds on the effective particle radius based on the physical size of the inner silicon oxygen cage. The cross is the smallest effective radius and effective modulus of a crystalline CpPOSS particle.

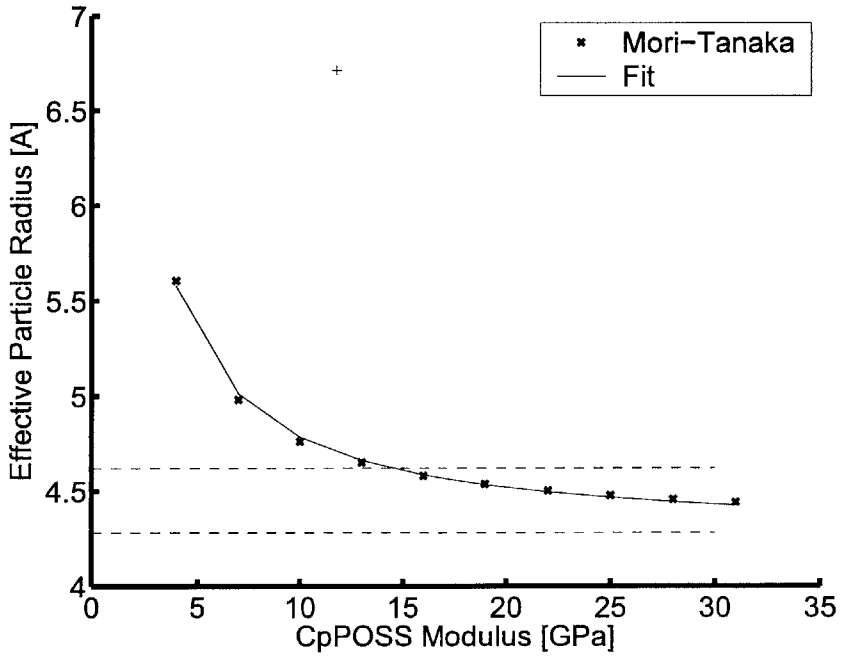

4.13 Discussion

In Section 4.2, we have shown that in this system the radius of gyration is on the order of the size of the particle. No significant changes in the radius of gyration occur with the addition of the CpPOSS. Simulations [25-32] reveal that when the filler particle is much smaller than the radius of gyration of the particle, the polymer radius of gyration increases, whereas if the particle is larger, then the radius of gyration of the polymer increases. In this case, the two length scales are similar and nothing happens to the radius of gyration.

In this chapter, we have also found aggregation of CpPOSS particles in systems with initially random dispersions. During the simulation irregular aggregates form. Though the simulations cannot be carried out for long enough times to observe directly the formation of large crystals, the relatively quick organization of neighboring CpPOSS particles suggest a strong tendency for crystallization. In Chapter 3, we found that there was a strong energetic driving force towards crystallization in the polyethylene system. These composite simulations clearly illustrate that there exists a thermodynamic driving force favoring the organization of initially well-dispersed CpPOSS particles within this polyethylene matrix.

Cluster analysis reveals the presence of both small and large clusters and demonstrates that it is highly unlikely that they could have so much internal orientation randomly. The attraction between particles and their tendency to form oriented groups is captured in a potential of mean force which can be used in coarse grained simulations to determine the properties of larger clusters of POSS over longer time frames.

The plasticizing effect of blended amorphous POSS in PMMA has been observed [4, 19]. In these systems, the plasticizer introduces additional free volume into the system, and increases the dynamics of the polymer leading to decreases in T_g and decreases in the shear modulus. The systems simulated here differ due to the relaxation time scales for the various components and the packing of the polymer around the POSS.

Notably diffusivity of the polymer chain decreases with increasing CpPOSS content. Clearly the POSS is not plasticizing this system. The reasons for this become clear when we compare the mobility of the polymer chain to that of the POSS. The POSS in this case is slower as seen in Section 4.3. Even though the particle itself is less mobile

than the polymer, there is still the chance that the pendant groups have high mobility which is transferred to the polymer thereby increasing the polymer segmental motion. This also does not happen in the current CpPOSS/PE system. We have shown in Chapter 3 that the ring rotation in the polymer has the same activation energy and same relaxation times as the dihedral angle rotation along the polymer backbone. Because of this, the ring groups cannot act to enhance the mobility of the polymer.

The decreasing mobility of the POSS and polymer with increasing CpPOSS content is also reflected in the increasing glass transition temperature seen in Section 4.5. The glass transition temperature increases above the PE T_g by approximately 12 degrees with the addition of 25 weight percent CpPOSS to the PE. This behavior along with the slowing dynamics is seen in the tethered POSS composites. The reason being that the tethered has slower dynamics and acts to slow the dynamics of the polymer. The difference in relaxation time scales in this system creates a similar scenario. Note that the T_g estimated by this simulation method is dependent on cooling rate. With increasing rate, there is an increase in the T_g value.

There is also an increase in the modulus of the composite with increasing POSS content in addition to increases in density. This data was used to extract the effective mechanical size of the CpPOSS particle. Using the Guth-Gold model, the effective rigid diameter of the CpPOSS particle was found to be approximately 4.45 Å consistent with the cage radius of the POSS. This consistency with the Guth-Gold model implies the POSS is essentially acting as a rigid filler (of size equal to the POSS cage) well bonded to the matrix through the interactions between the pendant groups and the matrix polymer.

As seen in Chapter 3, CpPOSS crystals are far from rigid and for a glassy polymer may be only 10 times stiffer than the polymer. The Mori-Tanaka equation was used with the effective modulus of the crystal from Chapter 3 to predict the increases in modulus that would occur if the POSS had taken the form of large crystallized particles within the PE matrix. The effective modulus calculated with these parameters is stiffer than the response seen in the composite system. The apparent conflict between the higher modulus for crystallized POSS filler particles versus the lower predicted modulus considering the POSS to be dispersed rigid particles lies in the weight fraction to effective volume fraction conversion. The volume fraction for a specific weight percent is

higher in the crystal phase than in the dispersed phase for this composite system. The modulus of the crystallized POSS is dramatically lower than the dispersed POSS cages, however the increased volume negates this effect and the crystallized particles in fact may give much higher stiffness in the composite. Aggregation in the simulations consisted of necklace type structures as opposed to well formed crystals.

The Mori-Tanaka equations were used to extract the effective properties of the CpPOSS filler. Though the size of the particle is theoretically determined by the atom configurations of the system which are known, there is significant ambiguity in the assignment of volume to single atoms and molecules. This ambiguity prevents us from defining with certainty the effective volume fraction of the POSS. Instead, we have determined a family of effective sizes and moduli which when used together describe the simulated behavior of the CpPOSS. Bounds on the effective size of the CpPOSS cage were calculated from the van der Waals parameters for the corner silicon atoms. These bounds are used to define a set of effective sizes and moduli which are consistent with the general dimensions of the POSS cage. In the composite systems, there exists a broad range of structures. There are dispersed POSS and groups of POSS particles interacting with one another. The calculated effective parameters are an average over these different structures and can be expected to vary as a function of mesostructure in the material.

1. Xu, H.Y., S.W. Kuo, J.S. Lee, and F.C. Chang, *Glass transition temperatures of poly(hydroxystyrene-co- vinylpyrrolidone-co-isobutylstyry1 polyhedral oligosilsesquioxanes).* Polymer, 2002. **43**(19): p. 5117-5124.
2. Xu, H.Y., S.W. Kuo, J.S. Lee, and F.C. Chang, *Preparations, Thermal Properties, and Tg Increase Mechanism of Inorganic/Organic Hybrid Polymers Based on Polyhedral Oligomeric Silsesquioxanes.* Macromolecules, 2002. **35**: p. 8788-8793.
3. Choi, J., J. Harcup, A.F. Yee, Q. Zhu, and R.M. Laine, *Organic/inorganic hybrid composites from cubic silsesquioxanes.* Journal of the American Chemical Society, 2001. **123**(46): p. 11420-11430.
4. Kopesky, E.T., T.S. Haddad, G.H. McKinley, and R.E. Cohen, *Miscibility and Properties of Acrylic Polyhedral Oligomeric Silsesquioxane-Poly(methyl methacrylate) Blends.* 2005.
5. Romo-Uribe, A., P.T. Mather, T.S. Haddad, and J.D. Lichtenhan, *Viscoelastic and morphological behavior of hybrid styryl-based polyhedral oligomeric silsesquioxane (POSS) copolymers.* Journal of Polymer Science Part B-Polymer Physics, 1998. **36**(11): p. 1857-1872.
6. Zhang, W., B.X. Fu, Y. Seo, E. Schrag, B.S. Hsiao, P.T. Mather, N.L. Yang, D. Xu, H. Ade, M. Rafailovich, and J. Sokolov, *Effect of Methyl Methacrylate/Polyhedral Oligomeric Silsesquioxane Random Copolymers in Compatibilization of Polystyrene and Poly(methyl methacrylate) Blends.* Macromolecules, 2002. **35**: p. 8029-8038.
7. Lichtenhan, J.D., N.Q. Vu, J.A. Carter, J.W. Gilman, and F.J. Feher, *Silsesquioxane Siloxane Copolymers from Polyhedral Silsesquioxanes.* Macromolecules, 1993. **26**(8): p. 2141-2142.
8. Shockey, E.G., A.G. Bolf, P.F. Jones, J.J. Schwab, K.P. Chaffee, T.S. Haddad, and J.D. Lichtenhan, *Functionalized polyhedral oligosilsesquioxane (POSS) macromers: New graftable POSS hydride, POSS alpha-olefin, POSS epoxy, and POSS chlorosilane macromers and POSS-siloxane triblocks.* Applied Organometallic Chemistry, 1999. **13**(4): p. 311-327.
9. Gilman, J.W., D.S. Schlitzer, and J.D. Lichtenhan, *Low earth orbit resistant siloxane copolymers.* Journal of Applied Polymer Science, 1996. **60**(4): p. 591-596.
10. Lichtenhan, J.D., Y.A. Otonari, and M.J. Carr, *Linear Hybrid Polymer Building-Blocks - Methacrylate-Functionalized Polyhedral Oligomeric Silsesquioxane Monomers and Polymers.* Macromolecules, 1995. **28**(24): p. 8435-8437.
11. Mather, P.T., H.G. Jeon, A. Romo-Uribe, T.S. Haddad, and J.D. Lichtenhan, *Mechanical relaxation and microstructure of poly(norbornyl-POSS) copolymers.* Macromolecules, 1999. **32**(4): p. 1194-1203.
12. Zheng, L., R.M. Kasi, R.J. Farris, and E.B. Coughlin, *Synthesis and thermal properties of hybrid copolymers of syndiotactic polystyrene and polyhedral oligomeric silsesquioxane.* Journal of Polymer Science Part a-Polymer Chemistry, 2002. **40**(7): p. 885-891.

13. Zheng, L., A.J. Waddon, R.J. Farris, and E.B. Coughlin, *X-ray characterizations of polyethylene polyhedral oligomeric silsesquioxane copolymers.* Macromolecules, 2002. **35**(6): p. 2375-2379.
14. Hsiao, B.S., H. White, M. Rafailovich, P.T. Mather, H.G. Jeon, S. Phillips, J. Lichtenhan, and J. Schwab, *Nanoscale reinforcement of polyhedral oligomeric silsesquioxane (POSS) in polyurethane elastomer.* Polymer International, 2000. **49**(5): p. 437-440.
15. Fu, B.X., B.S. Hsiao, S. Pagola, P. Stephens, H. White, M. Rafailovich, J. Sokolov, P.T. Mather, H.G. Jeon, S. Phillips, J. Lichtenhan, and J. Schwab, *Structural development during deformation of polyurethane containing polyhedral oligomeric silsesquioxanes (POSS) molecules.* Polymer, 2001. **42**(2): p. 599-611.
16. Fu, B.X., W.H. Zhang, B.S. Hsiao, M. Rafailovich, J. Sokolov, G. Johansson, B.B. Sauer, S. Phillips, and R. Balnski, *Synthesis and characterization of segmented polyurethanes containing polyhedral oligomeric silsesquioxanes nanostructured molecules.* High Performance Polymers, 2000. **12**(4): p. 565-571.
17. Hottle, J.R., H.J. Kim, J.J. Deng, C.E. Farmer-Creely, B.A. Viers, and A.R. Esker, *Blends of amphiphilic PDMS and trisilanolisobutyl-POSS at the air/water interface.* Macromolecules, 2004. **37**(13): p. 4900-4908.
18. Li, G.Z., L.C. Wang, H. Toghiani, T.L. Daulton, K. Koyama, and C.U. Pittman, *Viscoelastic and mechanical properties of epoxy/multifunctional polyhedral oligomeric silsesquioxane nanocomposites and epoxy/ladderlike polyphenylsilsesquioxane blends.* Macromolecules, 2001. **34**(25): p. 8686-8693.
19. Kopesky, E.T., T.S. Haddad, R.E. Cohen, and G.H. McKinley, *Thermomechanical properties of poly(methyl methacrylate)s containing tethered and untethered polyhedral oligomeric silsesquioxanes.* Macromolecules, 2004. **37**(24): p. 8992-9004.
20. Sun, H., *Ab-Initio Calculations and Force-Field Development for Computer-Simulation of Polysilanes.* Macromolecules, 1995. **28**(3): p. 701-712.
21. Sun, H. and D. Rigby, *Polysiloxanes: Ab initio force field and structural, conformational and thermophysical properties.* Spectrochimica Acta Part a-Molecular and Biomolecular Spectroscopy, 1997. **53**(8): p. 1301-1323.
22. Sun, H., *COMPASS: An ab initio force-field optimized for condensed-phase applications - Overview with details on alkane and benzene compounds.* Journal of Physical Chemistry B, 1998. **102**(38): p. 7338-7364.
23. Verlet, L., *Computer "Experiments" on Classical Fluids. I. Thermodynamical Properties of Lennard-Jones Molecules.* Physical Review, 1967. **159**(1): p. 98-103.
24. Berendsen, H.J., J.P.M. Postma, W.F.v. Gunsteren, A.D. Nola, and J.R. Haak, *Molecular Dynamics with Coupling to an External Bath.* Journal of Chemical Physics, 1984. **81**: p. 3684-3690.

25. Vacatello, M., *Monte Carlo simulations of polymer melts filled with solid nanoparticles.* Macromolecules, 2001. **34**(6): p. 1946-1952.
26. Vacatello, M., *Monte Carlo simulations of the interface between polymer melts and solids. Effects of chain stiffness.* Macromolecular Theory and Simulations, 2001. **10**(3): p. 187-195.
27. Vacatello, M., *Chain dimensions in filled polymers: An intriguing problem.* Macromolecules, 2002. **35**(21): p. 8191-8193.
28. Vacatello, M., *Molecular arrangements in polymer-based nanocomposites.* Macromolecular Theory and Simulations, 2002. **11**(7): p. 757-765.
29. Vacatello, M., *Ordered arrangements of semiflexible polymers at the interface with solids.* Macromolecular Theory and Simulations, 2002. **11**(1): p. 53-57.
30. Vacatello, M., *Phantom chain simulations of polymer-nanofiller systems.* Macromolecules, 2003. **36**(9): p. 3411-3416.
31. Vacatello, M., *Predicting the molecular arrangements in polymer-based nanocomposites.* Macromolecular Theory and Simulations, 2003. **12**(1): p. 86-91.
32. Vacatello, M., *Monte Carlo simulations of polymers in nanoslits.* Macromolecular Theory and Simulations, 2004. **13**(1): p. 30-35.
33. Pearson, D.S., G.V. Strate, E. Vonmeerwall, and F.C. Schilling, *Viscosity and Self-Diffusion Coefficient of Linear Polyethylene.* Macromolecules, 1987. **20**(5): p. 1133-1141.
34. McConnel, J.R., *Rotational Brownian motion and dielectric theory*. 1980, New York: Academic Press. 300.
35. Mori, T. and K. Tanaka, *Average Stress in Matrix and Average Elastic Energy of Materials with Misfitting Inclusion.* Acta Metallurgica, 1973(21): p. 571-574.
36. Guth, E. and O. Gold, Journal of Applied Physics, 1945: p. 16.

Chapter 5
Interfaces

By using nanometer sized particles as fillers in polymers, one hopes to achieve more significant and/or otherwise unachievable enhancements in properties while using less of the filler. Due to the small size of the particle, there will be a large surface area between the particle and the polymer. Because of this larger surface area, interactions between particle and matrix at this interface may alter the properties of the composite in ways that are not seen in traditional fillers.

In this system, the interface theoretically would consist of a thin layer of polymer surrounding the CpPOSS particle in which the properties of the polymer are different than the bulk matrix material. In this chapter, we will try to quantify the size of this region and find the degree to which the CpPOSS particle influences its neighboring material. Significantly, the measured thickness of the interface depends on the particular structural feature or the property used to define the interface. In the following sections, the interface is characterized using both static structural, thermodynamic, and dynamical measures.

5.1 Density Fluctuations Near the Particle

The influence of the filler on the surrounding matrix depends on the surface between the two. In the case of CpPOSS, the surface is irregularly shaped. Because the irregular shape may create pockets of unoccupied space increasing the free volume in the system. In order to assess this, the accessible surface as a function of probe particle size is shown in Figure 5-1. The van der Waals surface is created by assigning all of space that is within 1 van der Waals radius from each atom to the molecule. The geometry of the ring groups is evident and one can even see features of the internal cage. However, interacting polymer is limited in its ability to sample the surface of the CpPOSS molecule by the size of the monomer units.

In Figure 5-1b thru Figure 5-1d, the surface accessible to a probe atom of radius 3, 4, and 5 Å is shown. These surfaces are generated by taking a probe atom of a given size and rolling it over the molecule to find how close an atom of a given size can

approach the molecule. One can see from Figure 5-1c that for small probe particles of radius 3 Å, the probe particle can inhabit regions between the ring groups. As the probe particle becomes larger, the volume captured by the CpPOSS particle increases and the surface becomes smoother. The cavity between the ring groups disappears.

We found in Chapters 3 and 4 that there is some ambiguity in assigning a volume to a single molecule. Here we see clearly that the volume of the molecule depends on what it interacts with and an arbitrary partitioning of space between the two. This ambiguity is then propagated to the effective properties such as effective modulus that are calculated using these volumes.

In Figure 5-2, we display the radial distribution function, $g_{P\text{-}a}$, calculated between the center of mass of the CpPOSS and all other atoms in a system consisting of a single CpPOSS molecule embedded within a polyethylene matrix.

The aggregate structure was quantified by calculating the radial distribution function between the centers of mass of POSS particles and all silicon atoms within the system belonging to other POSS particles:

$$g_{P,A}(R) = \frac{V}{N_A N_P} \left\langle \sum_{i=1}^{N_P} \sum_{j=1}^{N_{Si}} \delta(R - |\vec{r}_i^{\,P} - \vec{r}_j^{\,A}|) \right\rangle \tag{5.1}$$

where $\vec{r}_i^{\,P}$ is the center of mass of POSS particle i, and $\vec{r}_j^{\,A}$ is the position of atom j of type A, V is the volume of the simulation cell, N_A is the number of atoms of type A, and N_P is the number of POSS particles in the system. Figure 5-2 shows that the silicon atoms in the cage of the CpPOSS are located at a distance of 2.5 Å from the center of the CpPOSS molecule. The cyclopentyl ring group extends from 4.5 to 7 Å from the center. But most interestingly, the polymer can occupy the region between the cyclopentyl ring groups. The polymer is found at distances as small as 5 Å from the center of the CpPOSS molecule.

Figure 5-2 also illustrates that the polymer surrounding the POSS has regions of more and less dense material as a function of distance from the center of the POSS. This can be seen in the peaks and troughs in the radial distribution function. These peaks are similar to those seen in liquids where there may be shells of neighboring particles. The order in this radial distribution function persists for several monolayers.

We can see from the earlier surface plots that as the size of the monomer increases, the penetration of the polymer into the cavities between R-groups decreases. One can surmise that these increases in free volume near the surface of the molecule may influence both the dynamics of the ring groups and of the polymer near the surface of the POSS.

Figure 5-3 illustrates that as the temperature increases, less polymer can be found within the cavities between the cyclopentyl ring groups. Ordering in the layers of polymer surrounding the polymer also decreases to approximately two monolayers as evidenced by the two liquid like peaks in the radial distribution function.

Figure 5-1: a) Van der Waals surface for the CpPOSS particle. Solvent accessible surface for particle with radius b) 3.0 Å, c) 3.0 Å, d) 4.0 Å, e) 5.0 Å.

a) VDW

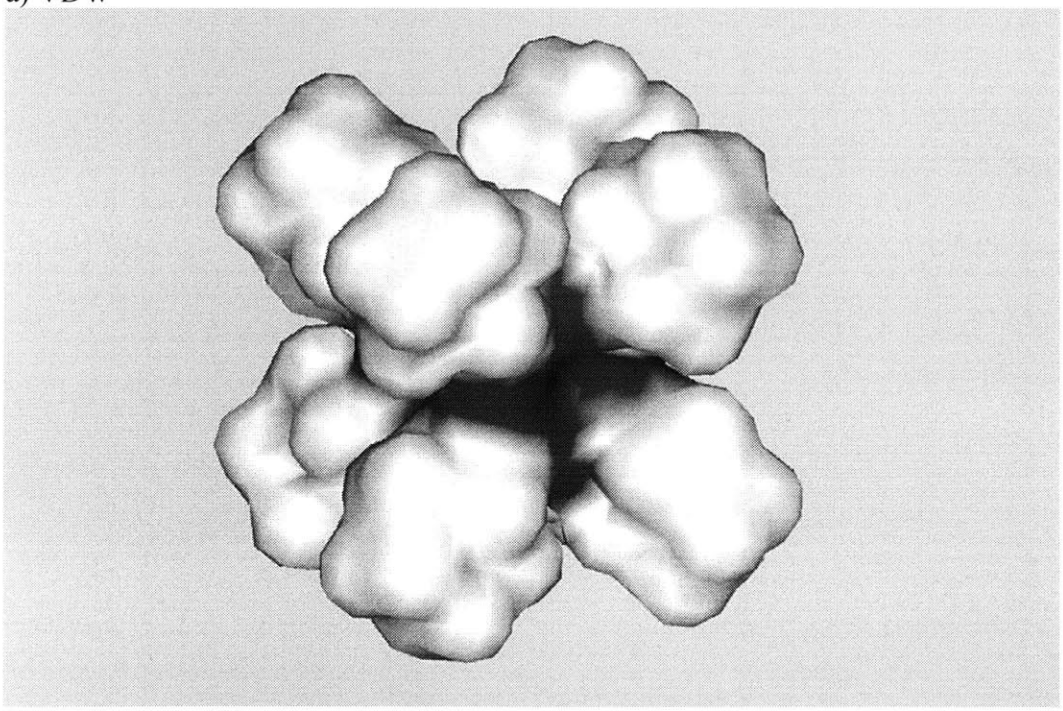

b) R = 3.0

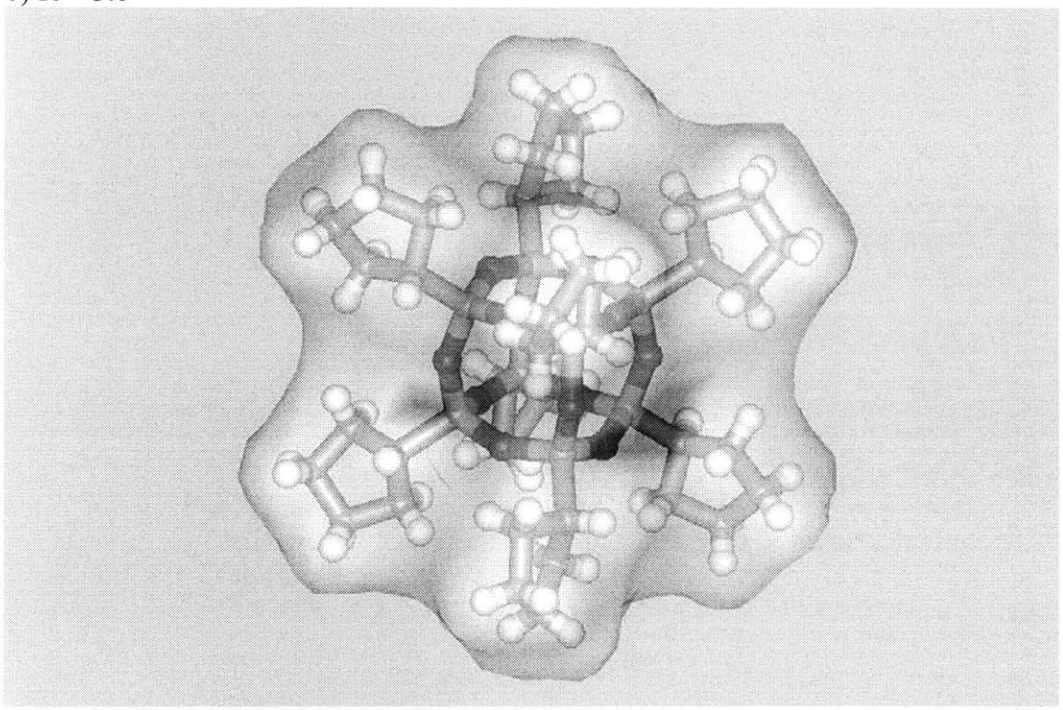

c) R = 3.0

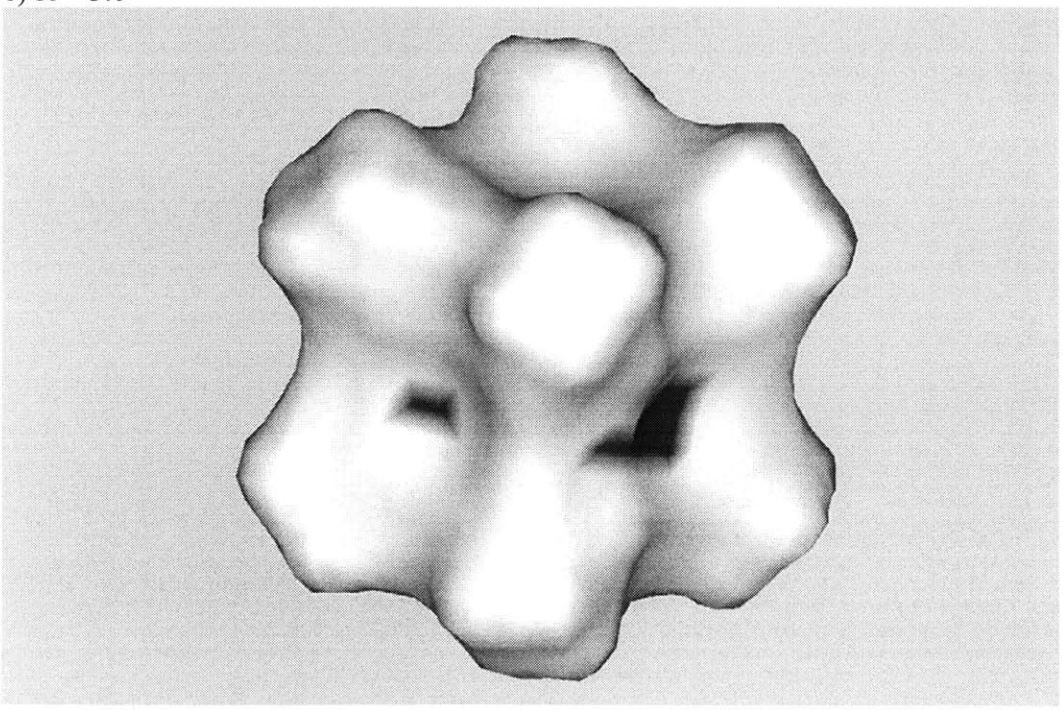

d) R = 4.0

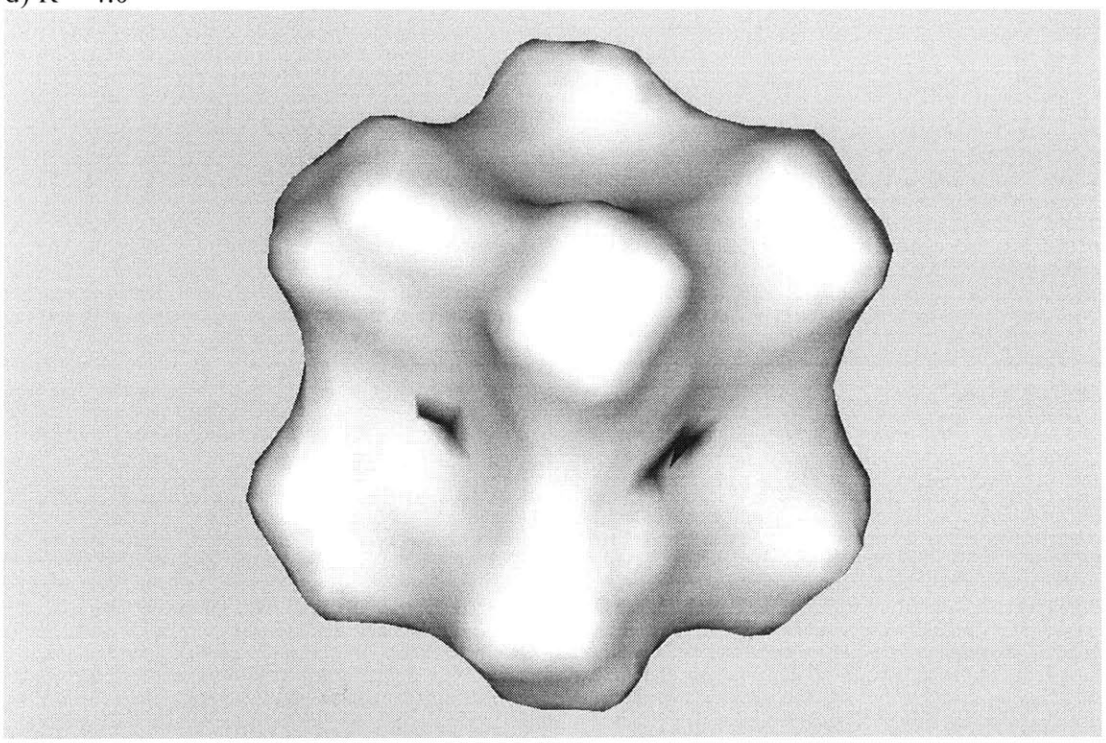

e) R = 5.0

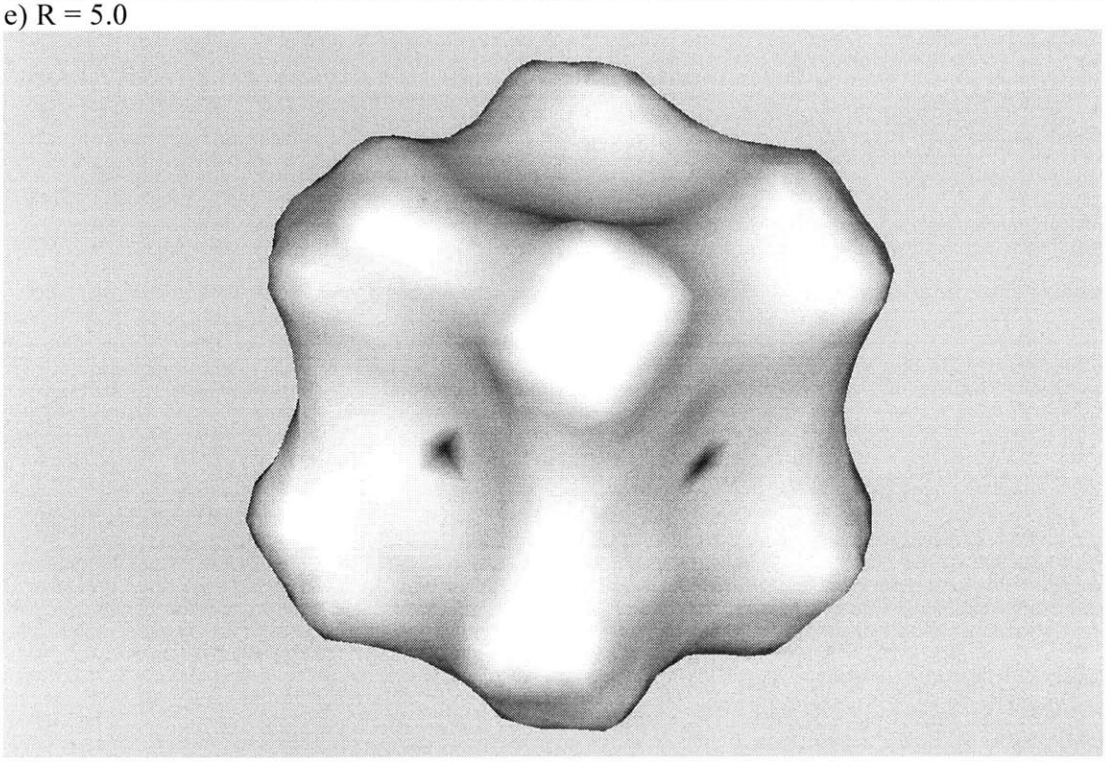

Figure 5-2: Radial distribution function between POSS centers of mass and all atoms in the system at 300K.

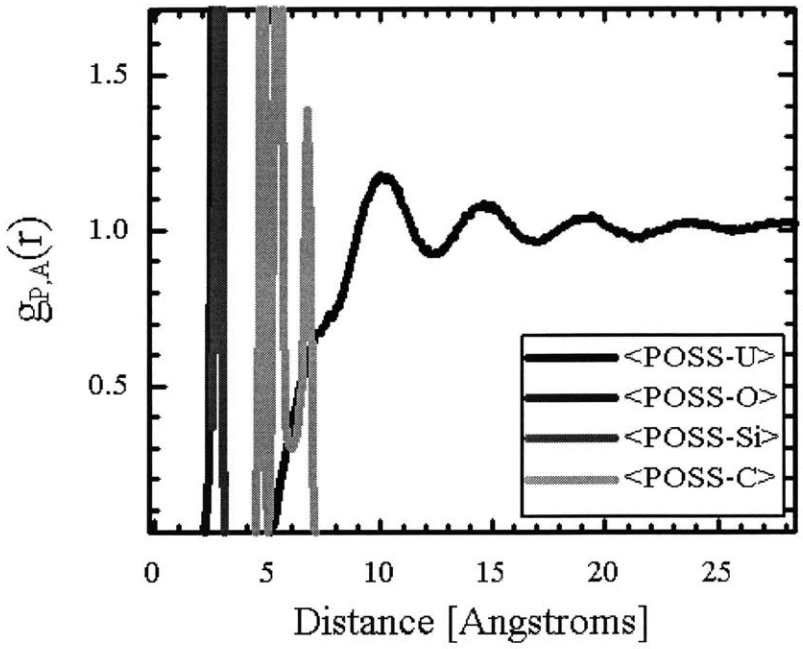

Figure 5-3: Comparison of radial distribution function between CpPOSS center of mass and the polymer backbone in the system at 300K and 500K.

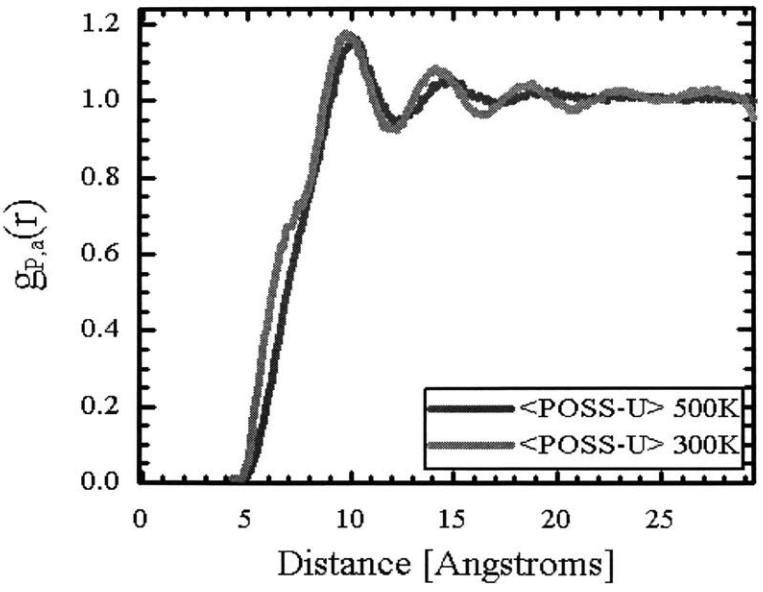

5.2 Structural Measures of Interface Thickness

The alignment and organization of polymeric material near the surface of the CpPOSS particle may have strong effects on the rheology of the melt and on the stiffness of the solid composite. The structure of the polymer was determined by monitoring the orientation of the polymer backbone relative to the radial direction of the CpPOSS particle. The orientation of a segment of the backbone is measured by the vector, $\vec{v}_i$, connecting the two carbon atoms bonded to carbon atom i as follows:

$$\vec{v}_i = \vec{r}_{i-1} - \vec{r}_{i+1} . \tag{5.2}$$

A vector, $\vec{\rho}_{i,j}$, can then be formed from the center of $\vec{v}_i$ to the center of mass of the CpPOSS particle, $\vec{r}_j^{\,P}$ as follows:

$$\vec{\rho}_{i,j} = \left[\frac{\vec{r}_{i-1} + \vec{r}_{i+1}}{2} \right] - \vec{r}_j^{\,P} . \tag{5.3}$$

The variation in structure was monitored using the following radial orientation order parameter, which measures the second Legendre coefficient for $\vec{v}_i$ as a function of radial distance from the center of a POSS molecule:

$$\gamma_{RO}(R) = \left\langle \frac{1}{N_{CH_2} N_P} \sum_{i=1}^{N_{CH_2}} \sum_{j=1}^{N_P} \frac{3\cos^2\left(\theta_{i,j}^{\rho v}\right) - 1}{2} \delta\left(\left|\rho_{i,j}\right| - R\right) \right\rangle \tag{5.4}$$

where N_{CH_2} is the number of polymer CH_2 groups within the system, and $\theta_{i,j}^{\rho v}$ is the angle between the local chain direction, $\vec{v}_i$, and the radial vector, $\vec{\rho}_{i,j}$. This function, which is an average over all i and j, takes a value of -0.5 when all vectors $\vec{v}_i$ are circumferential to the particle, 1.0 when all $\vec{v}_i$ are radially oriented, and 0.0 when the vector pairs $\vec{v}_i$ and $\vec{\rho}_{i,j}$ are randomly oriented with respect to one another.

Figures 5-4 and 5-5 show the results of applying equation (5.4) to systems with 5, 15, and 25 wt % CpPOSS/PE composites at 500K and 300K, respectively. At distances very far from the CpPOSS particle, γ_{RO} is approximately zero, indicating randomly oriented chains, as one would expect for an amorphous material. In all cases, as the distance R is

decreased, the value of $\gamma_{RO}(R)$ also decreases, indicating that the presence of the particle induces circumferential alignment of the polymer chains. The outermost extent of the interface was determined by fitting a stretched exponential to the γ_{RO} data and obtaining the distance, R, at which $\gamma_{RO}(R)$ is equal to 10% of the maximum deviation of γ_{RO} from its far field value. At 500K structural deviations from bulk matrix orientation can be observed up to 13.3±0.2 Å from the center of mass of the CpPOSS particle. At 300K the structural differences extend 11.7±0.7 Å from the center of mass of the CpPOSS particle.

Figure 5-4. Local structure calculation at 500K for 5, 15, and 25 weight percent Cyclopentyl POSS/PE composite.

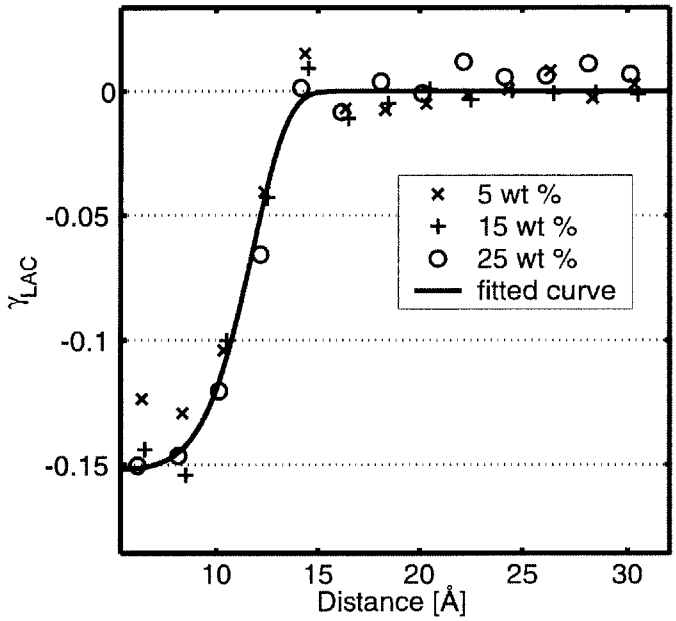

Figure 5-5. Local structure calculation at 300K for 5, 15, and 25 weight percent Cyclopentyl POSS/PE composite.

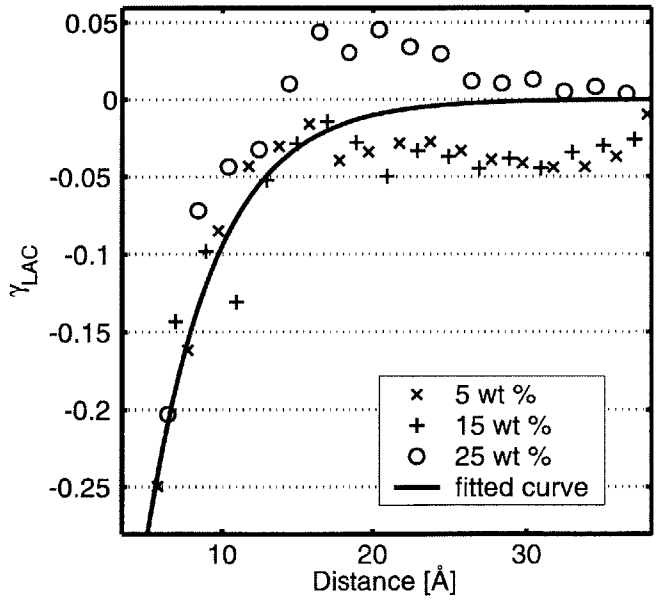

5.3 Dynamical Measures of Interfacial Thickness

The structural differences observed in the interface suggest that there might also be differences in the dynamics of the polymer in this region. It has previously been shown that attractive interactions between particle and polymer act to decrease the dynamics of polymer within some region surrounding the particle[1]. If this were true, it would explain the decrease in the overall mobility of the polymer within the composite described earlier.

The atomic mobility was monitored as a function of distance away from the center of the CpPOSS particle. The mean squared displacement, $MSD(R,\Delta t)$, of polymer carbon atoms which were originally a distance R from the center of the CpPOSS particle after a time Δt has elapsed is given by:

$$MSD(R,\Delta t) = \left\langle \frac{1}{N(R,t)} \sum_{j=1}^{N_P} \sum_{i=1}^{N_C} |\vec{r}_i(t+\Delta t) - \vec{r}_i(t)|^2 \, \delta\left(R - |\vec{r}_i(t) - \vec{r}_j^{\,P}(t)|\right) \right\rangle$$
$$N(R,t) = \sum_{j=1}^{N_P} \sum_{i=1}^{N_C} \delta\left(R - |\vec{r}_i(t) - \vec{r}_j^{\,P}(t)|\right) \qquad (5.5)$$

where N(R,t) is the number of polymer carbon atoms at a distance R from the center of the CpPOSS particle at time t, $\vec{r}_i(t)$ is the position of atom i at time t, $\vec{r}_j^{\,P}(t)$ is the position of the center of mass of CpPOSS particle j, and N_C is the number of polymer carbon atoms in the system. Figures 5-6 and 5-7 show $MSD(R,\Delta t)$ calculated at 500K and 300K, respectively, for a system with 5 weight percent POSS. The lack of variation in the mean squared displacement of atoms as a function of distance from the center of the CpPOSS particle indicates that the overall motion of the polymer backbone is not affected by the presence of the CpPOSS particle. The same behavior is observed in the 15 and 25 wt % CpPOSS composites. It is important to note that when Δt is large this calculation averages the mobility experienced by a polymer atom as it diffuses and explores regions more or less remote from the CpPOSS particle. As a consequence, we estimate that this function has very little resolving power at 500K since the polymer backbone is displaced by an average 8.2 Å over 40 ps (12 Å over 120 ps). However, at

300K the polymer backbone moves an average of only about 2.8 Å over 40 ps (3.7 Å over 120 ps) so the resolution should be adequate.

The lack of a change in mobility in the interfacial region indicates a neutral interaction between the CpPOSS particles and the polymer. This also suggests that the change in the overall mobility of the polymer is due to a dampening of mobility throughout the matrix due to the presence of the particles and not simply to localized changes in polymer mobility near the surface of the particle.

Figure 5-6. Local Mean Squared Displacement 500K for 5wt% CpPOSS/PE composite.

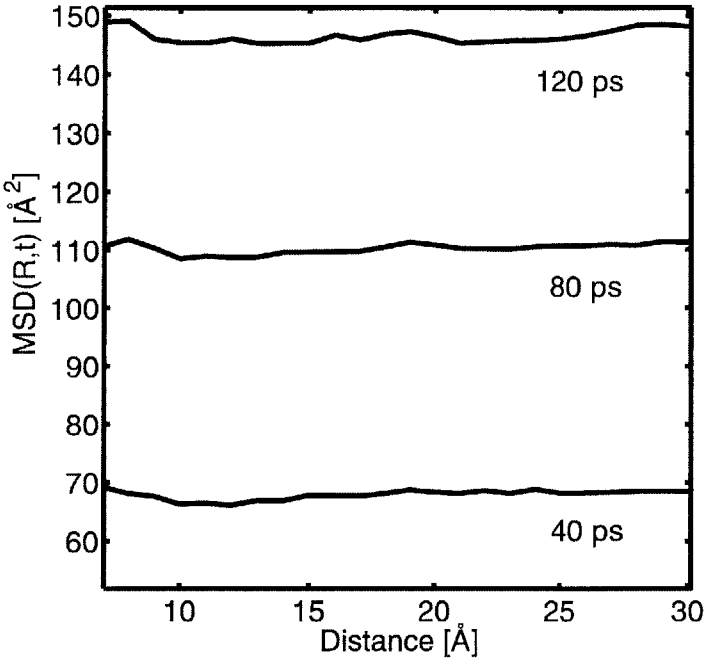

Figure 5-7. Local Mean Squared Displacement 300K for 5 wt% CpPOSS/PE composite.

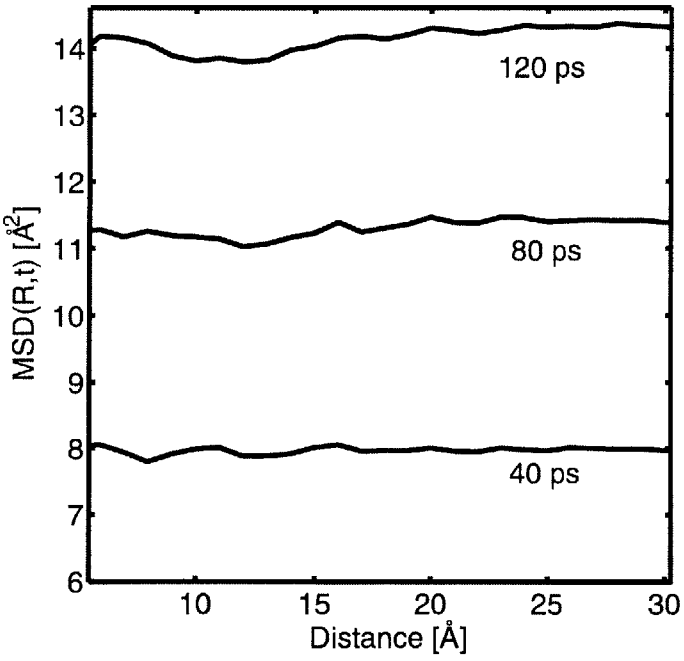

5.4 Radial and Circumferential Dynamics within the Interface

The structural alignment of the backbone does imply however that there should be some anisotropy in the polymer dynamics near the surface of the particle. To monitor this, the mean squared displacements described above were further resolved into components of motion in the radial, $MSD_r(R,\Delta t)$, and circumferential, $MSD_c(R,\Delta t)$, directions, as follows:

$$\vec{\Phi}_{ij} = \left[\vec{r}_i(t+\Delta t) - \vec{r}_i(t)\right]\delta\left(R - \left|\vec{r}_i(t) - \vec{r}_j^{\,P}(t)\right|\right)$$

$$MSD_r(R,\Delta t) = \frac{1}{N(R,t)}\sum_{j=1}^{N_P}\sum_{i=1}^{N_C}\left(\vec{\Phi}_{ij}\bullet\left[\vec{r}_i(t) - \vec{r}_j^{\,P}(t)\right]\right)^2 \qquad (5.6)$$

$$MSD_c(R,\Delta t) = \frac{1}{2N(R,t)}\sum_{j=1}^{N_P}\sum_{i=1}^{N_C}\left(\vec{\Phi}_{ij} - \vec{\Phi}_{ij}\bullet\left[\vec{r}_i(t) - \vec{r}_j^{\,P}(t)\right]\right)^2$$

Notice that the function representing the mobility in the radial direction measures the mean squared displacement in a single dimension while the circumferential mobility measures two-dimensional displacement in a plane. In order to compare the radial and circumferential mobilities, the circumferential mobility is multiplied by a factor of ½ in equation (5.6). This assumes that motion in the plane is isotropic and can be broken down into independent motion along two perpendicular axes within that plane. Far from the CpPOSS particle, MSD_r should be comparable to MSD_c.

Figures 5-8 and 5-9 show the component mean squared displacements for both radial and circumferential motion at 500K and 300K respectively. These figures reveal decreased mobility in the direction normal to the surface of the CpPOSS. To compensate, an increase in mobility in the circumferential direction is observed. Similar results were obtained for the 15 and 25 wt % systems. The observed changes in the motion of the polymer near the surface of the particle seem to be due to the structural alignment of the backbone with the particle surface.

Figure 5-8. Normal Local Mean Squared Displacement 500K.

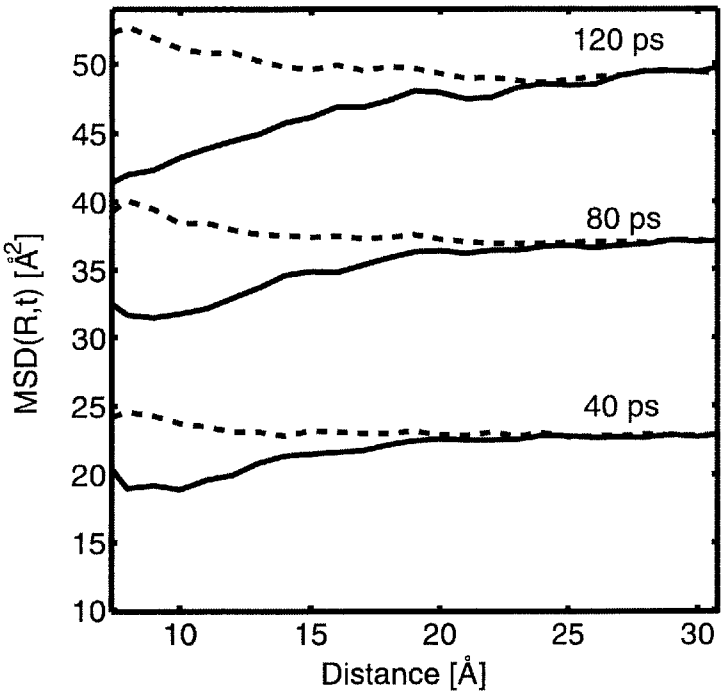

Figure 5-9. Tangential Local Mean Squared Displacement 500K.

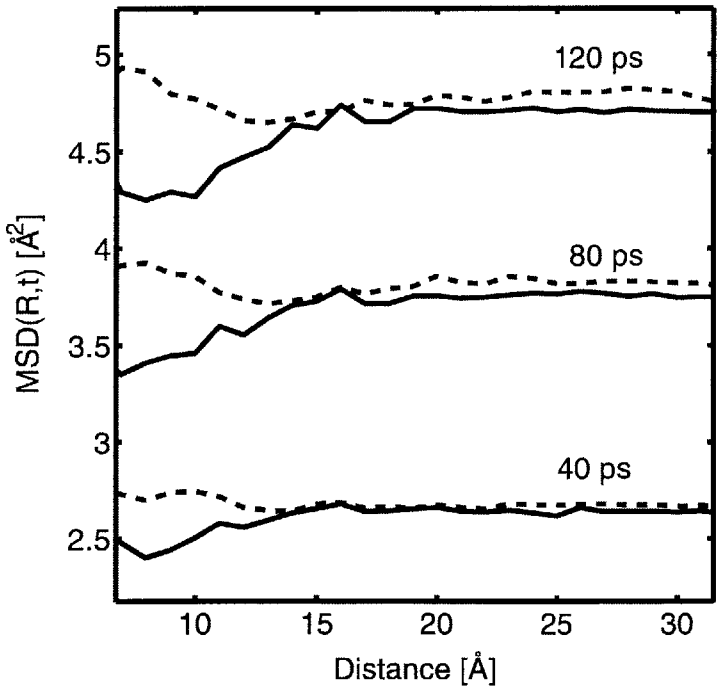

5.5 Radius of Gyration Near the CpPOSS

In Section 4-2, there is no significant change in the radius of gyration of the polymer chains with increasing CpPOSS content. In systems of freely jointed chains interacting with walls, changes in the radius of gyration of the polymer near the surface have been observed[2].

The radius of gyration of the polymer was calculated as a function of distance of the chain center of mass from the center of mass of the CpPOSS particle as follows:

$$R_g(r) = \frac{\sum_{j=1}^{N_{POSS}} \sum_{i=1}^{N_{chains}} R_g \delta\left(r - \left|\mathbf{r}_{poly,i}^{COM} - \mathbf{r}_{POSS,j}^{COM}\right|\right)}{\sum_{j=1}^{N_{POSS}} \sum_{i=1}^{N_{chains}} \delta\left(r - \left|\mathbf{r}_{poly,i}^{COM} - \mathbf{r}_{POSS,j}^{COM}\right|\right)}. \tag{5.7}$$

where $R_{g,i}$ is the radius of gyration of polymer chain i calculated using Equation 4.3. The results are shown in Figure 5-10. We can see only slight increases of less than 6 percent in the value of the radius of gyration as distance between polymer center of mass and POSS center of mass decreases. The increase does agree with the structural differences reported in Section 5.2. The elongation of the chain near the surface of the particle leads to the slight increase in the radius of gyration. One can also see that a polymer with center of mass near the surface of the CpPOSS particle has half of its configurational space blocked by the presence of the particle. The radius of gyration would have to increase near the surface.

Figure 5-10: Normalized radius of gyration for polymer chains as a function of distance from the center of the CpPOSS molecule.

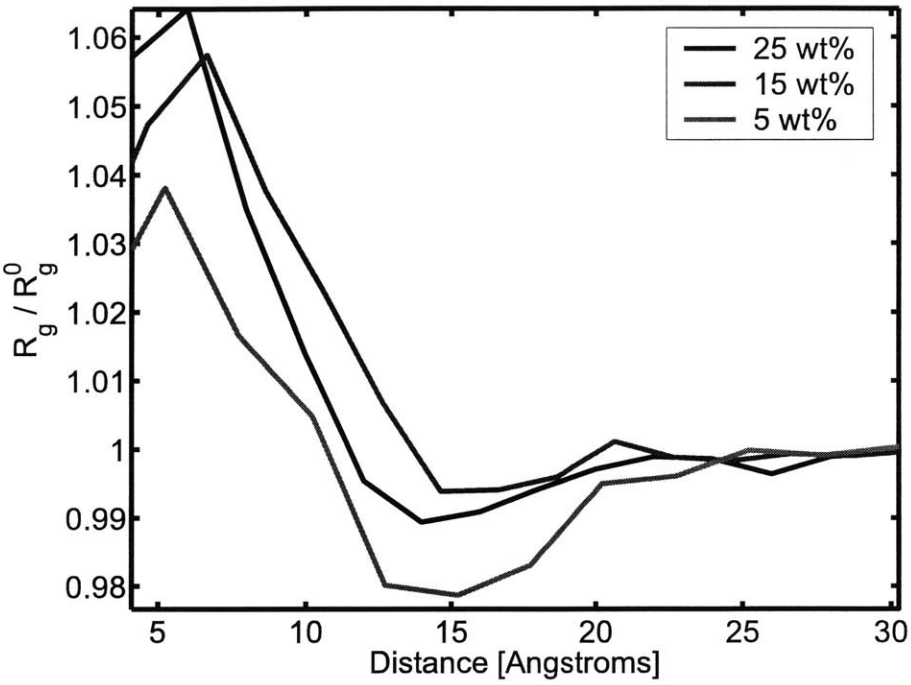

5.6 Fraction of Polymer found within the Interface

One of the advantages of using nanoparticles over traditional micron sized particle fillers is that the nanocomposite has a tremendous amount of interface between filler and polymer. Even when the interface is extremely thin, i.e. on the order of 1 or 2 Angstroms, the volume fraction of polymer within the interface can be extremely large. The data in Section 5.2 suggests that the polymer within 13.2 Å at 500K and 11.7 Å at 300K of the center of the CpPOSS particle has modified properties. The volume fraction of polymer in the interface was determined by determining the weight fraction of polymer that was within this distance from any CpPOSS particle. The results, shown in Table 5-1, reveal that significant fractions of polymer can be found within the interface between the CpPOSS and polymer even though the interface may be only a monolayer thick. The fraction of polymer located within the interface runs as high as 24% at 300K, and 43% at 500K for the 25 wt% composite. Because of this, the slight changes in the structural or dynamic measures reported in Sections 5-2 through 5-6 can have significant effects on the properties of the composite.

This data also shows that the volume fraction of polymer in the interface drops significantly with even small amounts of aggregation. Assuming that all particles are dispersed in the polymer matrix and their separation distances are larger than the twice distance to the outer edge of the interface, then the volume fraction of polymer in the interface scales linearly with weight fraction of CpPOSS. In Figure 5-11, we have plotted the extrapolated values of polymer weight fraction in the interface as well as the actual values. We can see that at the higher loadings, the weight fraction of polymer in the interface decreases. This drop off is an indication of aggregation. As shown in Figure 5-12, when CpPOSS particles come in close contact with one another, they may either share interface, or there may be no polymer between them. If they crystallize, which has been shown in Chapter 4 to happen in this system, then no polymer is located between the CpPOSS particles causing the volume fraction of polymer in the interface to decrease.

In experimental system, even small amounts of aggregation will drive the interfacial volume down significantly. In micron scaled fillers, this interfacial volume will be insignificant.

Table 5-1: Weight percent of polymer found within 13.2 Å at 500K and 11.7 Å at 300K.

Composition [weight % POSS]	300K	500K
5	6.8(2)	10.8(6)
15	16.7(3)	27(2)
25	24.4(3)	43(2)

Figure 5-11: Simulated and extrapolated weight Percent of polymer found within the interface.

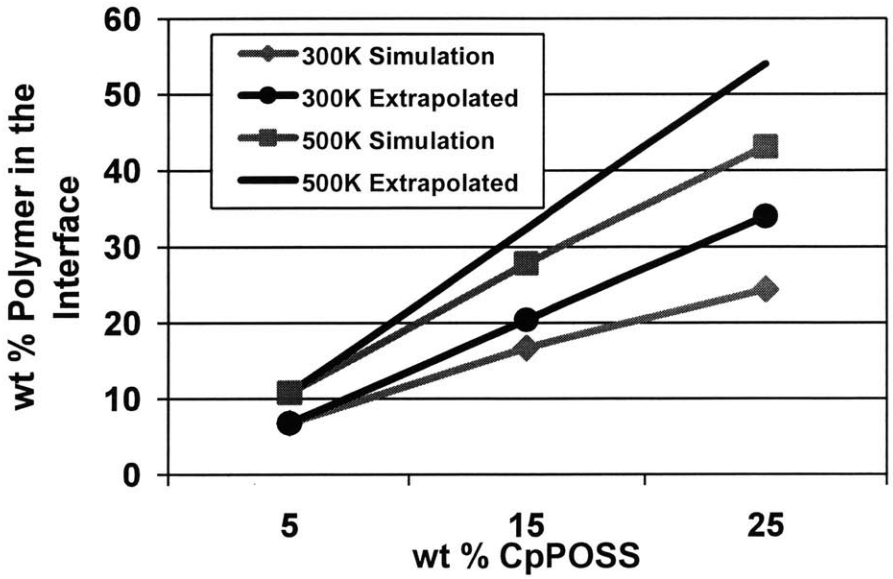

Figure 5-12: Illustration of shared interface.

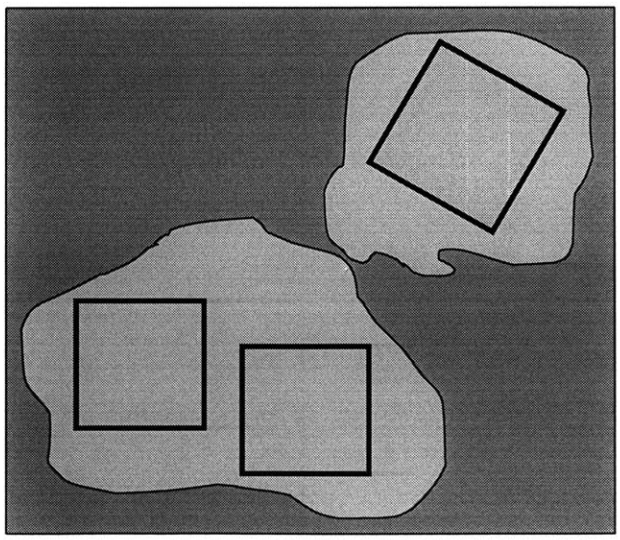

5.7 Discussion

Due to the large surface to volume ratio for the nanoscopic CpPOSS particles, there is a significant volume fraction of interfacial matrix polymer within a well dispersed system. However, this volume fraction becomes less important as the particles aggregate. In the absence of aggregation, and in systems in which the particles do not interact, one would expect the volume fraction of interfacial matrix polymer to increase in direct proportion to the wt% of POSS. Extrapolation of the data from the 5 wt% composite to 25 wt% in this way would imply a volume fraction of interfacial matrix polymer of 54%. Instead, we determined only 43% of the polymer was in the interface. We were able to show both that the POSS particles interact and that they aggregate. Nevertheless, this reduction in interfacial matrix polymer volume fraction is, in our view, modest; we speculate that, had we the liberty to simulate for longer times, this reduction would have been more significant due to additional aggregation of the POSS particles.

These simulations reveal that the polymer within the interface adopts a configuration to accommodate the CpPOSS particle by aligning the polymer backbone tangent to the surface of the CpPOSS particle. While the extent of the interface decreases with decreasing temperature, the degree of alignment within the interface increases. The interactions between the CpPOSS particle and the polymer are governed primarily by the interactions of the cyclopentyl ring groups and the polymer. These interactions are not significantly different from polymer/polymer interactions and therefore the influence of the particle on polymer dynamics, as measured by a scalar diffusivity as a function of distance from the particle, appears to be negligible. However, the anisotropy of these dynamics are significantly altered. In the vicinity of the particle, the mean squared displacement increases in the direction parallel to the surface of the CpPOSS particle, while it decreases in the direction perpendicular to that surface. The anisotropy in dynamics can be attributed to structural alignment near the particle: the polymer can move more easily in the direction of its backbone (i.e. tangential to the particle) through a reptation type motion than it can perpendicular to the backbone (i.e. radial to the particle). One might expect the anisotropy in diffusivity observed for the interfacial polymer matrix material to be reflected also in the anisotropic diffusion of small guest

molecule. Since the mobility of the polymer is enhanced in the tangential direction, the diffusion of small molecules could also be enhanced in this direction. Therefore, percolation of this aligned layer throughout the entire composite could provide a path for significantly increased diffusion of small molecular species. The aligned layer would also present anisotropic mechanical behavior with more compliant shear modulus near the surface of the particle and enhanced modulus.

The interfacial properties observed within these composite systems are influenced most directly by the geometry of the inclusion and the fact that its movement is slower than that of the polymer. As noted earlier, the CpPOSS particle diffuses at a rate 1.5 times slower than the polymer. We observed a decrease in the diffusion rate of both the polymer and of the CpPOSS, as well as a decrease in the rotational relaxation time of CpPOSS, with increasing CpPOSS content. Since there is no decrease in the mobility of the polymer within the interface as compared to the bulk polymer, the decreased dynamics must be attributable to the confinement effect on the polymer from multiple CpPOSS particles. The particles are attracted to one another and these aggregates not only serve to confine the motion of the polymer but also to hinder the movement of the POSS particles themselves. This is seen in the decreasing POSS particle mobility with increasing concentration.

1. Starr, F.W., T.B. Schroder, and S.C. Glotzer, *Effects of a nanoscopic filler on the structure and dynamics of a simulated polymer melt and the relationship to ultrathin films.* Physical Review E, 2001. **6402**(2).
2. Bitsanis, I. and G. Hadziioannou, *Molecular dynamics simulations of the structure and dynamics of confined polymer melts.* Journal of Chemical Physics, 1989. **92**(6): p. 3827.
3. Xu, H.Y., S.W. Kuo, C.F. Huang, and F.C. Chang, *Poly(acetoxystyrene-co-isobutylstyryl POSS) nanocomposites: Characterization and molecular interaction.* Journal of Polymer Research-Taiwan, 2002. **9**(4): p. 239-244.
4. Xu, H.Y., S.W. Kuo, J.S. Lee, and F.C. Chang, *Preparations, thermal properties, and T-g increase mechanism of inorganic/organic hybrid polymers based on polyhedral oligomeric silsesquioxanes.* Macromolecules, 2002. **35**(23): p. 8788-8793.
5. Choi, J., J. Harcup, A.F. Yee, Q. Zhu, and R.M. Laine, *Organic/inorganic hybrid composites from cubic silsesquioxanes.* Journal of the American Chemical Society, 2001. **123**(46): p. 11420-11430.

Chapter 6
Conclusions and Future Direction

Interest in polymer nanocomposites has been driven by the desire to create materials with novel sets of properties. The ability to control the nanostructure of the material to achieve a tougher and stiffer composite, or a stiffer composite without sacrificing the processibility of the polymer, or achieving a functional composite would greatly impact polymer science. The behavior of these nanocomposites can be the result of phenomena on several different length scales. The polymer/filler interface, the dispersion state of the filler, the length scale of the filler in comparison to the length scale of the polymer can all influence the material properties. In this thesis, we attempt to understand the interplay between these variables in a cyclopentyl polyhedral oligomeric silsesquioxane polyethylene nanocomposite.

We have used atomistic simulations to investigate the properties of Cyclopentyl POSS (CpPOSS)/ polyethylene (PE) blended composites. We have shown that the force field developed by Sun et al. for polysilanes [13], polysiloxanes [14], and alkanes [15] adequately describes the intermolecular and intramolecular interactions in the CpPOSS molecule. This was demonstrated through simulations of vibrational spectra as well as crystal structure which were found to be in excellent agreement with reported data. Using this force field, we were able to determine properties for the constituent phases and for the composite as well as map out property variations in the interface between CpPOSS and polymer.

The addition of CpPOSS to the C_{50} chains is shown to decrease the mobility of the polymer. The CpPOSS acts as a stiffening agent, decreasing the mobility of C_{50} polymer and CpPOSS, and increasing the glass transition temperature of the composite. The glass transition temperature increases above the pure PE T_g by approximately 12 degrees with the addition of 25 weight percent CpPOSS to the PE.

Interestingly, a number of POSS/polymer blends have been experimentally observed to exhibit a decrease in the glass transition temperature[4, 5] with the addition of POSS. In these systems, the POSS acts as a plasticizer, introducing additional free volume into the system and increasing the dynamics of the polymer leading to the

observed decreases in T_g and decreases in shear modulus. The systems simulated here differ due to the relaxation time scales for the various components and the packing of the polymer around the POSS. Notably diffusivity of the C_{50} polymer chain decreases with increasing CpPOSS content. Clearly the POSS is not plasticizing the nanocomposite system studied in this thesis. Increases in T_g along with the slowing dynamics is seen experimentally in the tethered POSS/polynorbornene composites[6]. The reason being that the tethered POSS has slower dynamics and acts to slow the dynamics of the polymer.

We have also found aggregation of CpPOSS particles in the PE/CpPOSS systems with initially random dispersions. Over the simulation time period (17 ns), irregular aggregates form. Though the simulations cannot be carried out for long enough times to observe directly the formation of large crystals, the relatively quick organization of neighboring CpPOSS particles suggest a strong tendency for crystallization. The observation of aggregation is supported by calculations showing that there is a strong energetic driving force towards crystallization of the CpPOSS in the CpPOSS/polyethylene composite system. These composite simulations clearly illustrate that there exists a thermodynamic driving force favoring the organization of initially well-dispersed CpPOSS particles within this polyethylene matrix.

Cluster analysis reveals the presence of both small and large clusters. Clusters were quantified in terms of proximity of particles as well as relative orientational ordering of particles. The attraction between particles and their tendency to form oriented groups is captured in a potential of mean force which can be used in coarse grained simulations to determine the properties of larger clusters of POSS over longer time frames.

Calculations of the moduli of the CpPOSS crystal reveal that the high stiffness of the central silicon-oxygen cage within the CpPOSS molecule does not translate into high stiffness for the CpPOSS crystal. The interactions between the flexible organic cyclopentyl R-groups add compliance to the crystal and the measured modulus is on the order of 15 GPa. Compared to a glassy or semicrystalline polymer modulus of 1 – 2 GPa, these particles are only 1 order of magnitude stiffer.

Blending the CpPOSS into the polymer lead to increases in the effective modulus of the composite. Micromechanical models such as the Mori-Tanaka model are often used to describe effective composite properties in terms of the constituent properties and the volume fraction of filler. When the filler dimension approaches the nanometer length scale, the volume of the molecule cannot be precisely determined. There is ambiguity in how the size of a molecule is defined. Therefore in both simulation and experiment, the known weight fraction of filler added to a composite cannot be uniquely converted into a volume fraction. Assumptions must be made about the geometry of the filler molecule in order to convert from weight fraction to volume fraction.

Using the effective composite behavior, two questions were posed. Given information about the filler, i.e. the stiffness of the silicon oxygen cage and several approximations for the size of the molecule, how does the predicted composite behavior compare to the simulated behavior? The answer outlined in Chapter 4, suggests that the stiffening is due to the rigidity of the silicon-oxygen cage and the organic pendant groups do not add to the rigidity of the composite. The second question, given the simulated composite moduli, what are the effective properties, both size and moduli, of the filler molecule? Due to the uncertainty in the definition of volume at this length scale, we show that the best one can do is to obtain a range of effective sizes which each have a unique corresponding effective modulus. These pairs of properties then describe the behavior of the filler.

The effective modulus for a PE/CpPOSS composite that contains crystalline inclusions is higher than that for a PE/CpPOSS composite with the same weight percent of CpPOSS and perfectly dispersed POSS cages. The crystallized POSS filler particles display a lower modulus than the dispersed POSS particles, but the volume fraction for a specific weight percent is higher in the crystal phase than in the dispersed phase for this composite system. This leads to higher effective moduli when the domains are aggregated crystalline domains versus perfectly dispersed POSS cages. Although aggregation was seen in the simulations, we observe the formation of necklace type structures as opposed to well formed crystals.

Due to the large surface to volume ratio for the nanoscopic CpPOSS particles, there is a significant volume fraction of interfacial matrix polymer within a well

dispersed system. These simulations reveal that the polymer within the interface adopts a configuration to accommodate the CpPOSS particle by aligning the polymer backbone tangent to the surface of the CpPOSS particle. While the interface size decreases with decreasing temperature, the degree of alignment within the interface increases. The interactions between the CpPOSS particle and the polymer are governed primarily by the interactions of the cyclopentyl ring groups and the polymer. These interactions are not significantly different from the polymer to polymer intermolecular interactions and therefore the influence of the particle on polymer dynamics, as measured by a scalar diffusivity as a function of distance from the particle, appears to be negligible. However, the anisotropy of these dynamics are significantly altered. In the vicinity of the particle, the mean squared displacement increases in the direction parallel to the surface of the CpPOSS particle, whereas it decreases in the direction perpendicular to that surface. The anisotropy in dynamics can be attributed to structural alignment near the particle: the polymer can move more easily in the direction of its backbone (i.e. tangential to the particle) through a reptation type motion than it can perpendicular to the backbone (i.e. radial to the particle). One might expect the anisotropy in diffusivity observed for the interfacial polymer matrix material to be reflected also in the anisotropic diffusion of a small guest molecule. Since the mobility of the polymer is enhanced in the tangential direction, the diffusion of small molecules could also be enhanced in this direction. Therefore, percolation of this aligned layer throughout the entire composite could provide a path for significantly increased diffusion of small molecular species. The aligned layer would also present anisotropic mechanical behavior with more compliant shear modulus near the surface of the particle and enhanced modulus.

The interfacial properties observed within these composite systems are influenced most directly by the geometry of the inclusion and the fact that its movement is slower than that of the polymer. The CpPOSS particle diffuses at a rate 1.5 times slower than the polymer. We observed a decrease in the diffusion rate of both the polymer and of the CpPOSS, as well as a decrease in the rotational relaxation time of CpPOSS, with increasing CpPOSS content. Since there is no decrease in the mobility of the polymer within the interface as compared to the bulk polymer, the decreased dynamics must be attributable to the confinement effect on the polymer from multiple

CpPOSS particles. The particles are attracted to one another and these aggregates not only serve to confine the motion of the polymer but also to hinder the movement of the POSS particles themselves. This is seen in the decreasing POSS particle mobility with increasing concentration.

These simulations reveal that as the dimensions of the filler approach the nanoscopic length scale, it is important to consider not only the size and geometry of the filler but also the energetic interactions between filler and matrix. As shown in this thesis, the geometry and energetics can drive aggregation and crystallization of the filler within the matrix and lead to changes in the structure and properties of material in the interface. It is also important to realize that as the dimensions of a filler approach the molecular dimensions, continuum level concepts such as volume fraction of filler become ambiguous. The assumptions that are used to define these quantities can significantly alter the results.

Given the wide range of POSS chemistry available, it would be quite informative to repeat these types of simulations for different POSS and polymer chemistry. Most importantly, one could map out the energetic driving forces for crystallization and aggregation as a function of both polymer and POSS chemistry. This would allow scientists to rationally select composites based on the most probable resulting morphologies. In addition, large scale deformation of these nanocomposites introduces several interesting problems. The anisotropy of the polymer near the surface of the particle may affect the way they accommodate large deformation. The bonding between POSS and polymer in the system studied (CpPOSS/PE) is quite good since the organic pendant groups have the same chemistry as the polymer. Debonding of particles is difficult and may require the same amount of energy as forming voids in the polymer itself. However, with different pendant groups or different polymers, the bonding between polymer and POSS may not be so strong.

Due to the fast dynamics of the polymer in these simulations, we have seen a response in a blended POSS polymer composite that differs from the experimental literature. However, moving to a polymer with a different chemistry and larger molecular weight will decrease polymer mobility making the POSS more of a plasticizer in the system. By studying a variety of chemistries and molecular weights, one may be able to

determine which chemistries are most likely to produce desired mechanical behavior for POSS polymer nanocomposites.

Also, by using the coarse grained potentials developed in this work and by calculating similar potentials for other POSS polymer chemistry, one can study the formation of mesostructure in these composites. We have shown clearly that the mesostructure of the POSS can have significant effects on the mechanical properties of the composite. Understanding the relation between chemistry and mesostructure will help to guide the development of new POSS polymer composites.

1. Sun, H., *Ab-Initio Calculations and Force-Field Development for Computer-Simulation of Polysilanes.* Macromolecules, 1995. **28**(3): p. 701-712.
2. Sun, H. and D. Rigby, *Polysiloxanes: Ab initio force field and structural, conformational and thermophysical properties.* Spectrochimica Acta Part a-Molecular and Biomolecular Spectroscopy, 1997. **53**(8): p. 1301-1323.
3. Sun, H., *COMPASS: An ab initio force-field optimized for condensed-phase applications - Overview with details on alkane and benzene compounds.* Journal of Physical Chemistry B, 1998. **102**(38): p. 7338-7364.
4. Kopesky, E.T., T.S. Haddad, R.E. Cohen, and G.H. McKinley, *Thermomechanical properties of poly(methyl methacrylate)s containing tethered and untethered polyhedral oligomeric silsesquioxanes.* Macromolecules, 2004. **37**(24): p. 8992-9004.
5. Kopesky, E.T., T.S. Haddad, G.H. McKinley, and R.E. Cohen, *Miscibility and Properties of Acrylic Polyhedral Oligomeric Silsesquioxane-Poly(methyl methacrylate) Blends.* 2005.
6. Mather, P.T., H.G. Jeon, A. Romo-Uribe, T.S. Haddad, and J.D. Lichtenhan, *Mechanical relaxation and microstructure of poly(norbornyl-POSS) copolymers.* Macromolecules, 1999. **32**(4): p. 1194-1203.